EFFICIENCY IMPROVEMENT ANALYSIS FOR COMMERCIAL VEHICLES BY (I) POWERTRAIN HYBRIDIZATION AND (II) CYLINDER DEACTIVATION FOR NATURAL GAS ENGINES

by

Shubham Agnihotri

A Thesis

Submitted to the Faculty of Purdue University

In Partial Fulfillment of the Requirements for the degree of

Master of Science in Mechanical Engineering

School of Mechanical Engineering

West Lafayette, Indiana

August 2021

THE PURDUE UNIVERSITY GRADUATE SCHOOL
STATEMENT OF COMMITTEE APPROVAL

Dr. Gregory M. Shaver
School of Mechanical Engineering

Dr. Oleg Wasynczuk
School of Electrical and Computer Engineering

Dr. John Evans
School of Agriculture Engineering

Approved by:
Dr. Nicole Key

Dedicated to my brothers who inspire me to be better than yesterday.

ACKNOWLEDGMENTS

I am grateful to the opportunity provided by my P.I Dr.Greg Shaver to work on two industry projects in the two years of my Masters. He has been very helpful and inspiring at the same time. It is motivating to understand the impact of Shaver group's research on industry and regulators.

I would like to acknowledge Dr. Wasynczuk who was a wonderful teacher for the Hybrid Electric Vehicle course. I enjoyed my time working as a TA for the course.

I would like to thank Dr. Lisa Farrel and Akash Desai from Cummins Inc. for their invaluable industry support for the natural gas engine project.

Special thanks to Herrick labs for providing the infrastructure to the projects. Thanks to Eric Holloway and Ryan Thayer for their invaluable support to the projects.

It been a pleasure working with Tyler Swedes on the hybrid truck, collaborating with Vrushali Deshmukh on the engine simulation work and a fun journey with Doni Thomas, Chisom Emegaonkar, Adil Shaikh building the test cell for natural gas engine compatibility. I would also like to thank my colleagues who became good friends, Miles Droege, Shveta Dhamankar and Shubham Ashtha.

Thanks to Sayali who has been a special person in my life and witnessed the journey firsthand. She inspires me to keep pushing. I would like to acknowledge all my friends since childhood who I call my brothers. The brotherhood has truly helped me become the person who I am today. Last but not the least my family, my parents and my sister without whom I wouldn't be here.

TABLE OF CONTENTS

LIST OF TABLES

LIST OF FIGURES

LIST OF SYMBOLS

$\eta_{thermal}$	Thermal efficiency
η_{closed}	Closed efficiency
η_{open}	Open efficiency
$\eta_{mechanical}$	Mechanical efficiency
P_{brake}	Brake Power
$\dot{m}$	Mass flow rate
Q_{lhv}	Calorific Lower Heating Value
V_d	Displacement Volume
Cd_1	Discharge Coefficient
D	Throttle Diameter
δP	Delta Pressure
a	Acceleration
A_f	Truck Frontal Area
C_d	Vehicle Drag Coefficient
E	Energy
F	Force
g	Gravitational Acceleration
h	Elevation
θ	Road Grade Angle
KE	Kinetic Energy
m	Total Vehicle Mass
μ	Rolling Resistance Coefficient
P	Power
PE	Potential Energy
ρ	Fluid Density
t, τ	Time
V	Voltage
v	Speed

W	Work
x	Distance Travelled

ABBREVIATIONS

1D	One Dimensional
AC	Alternating Current
AFR	Air Fuel Ratio
BEV	Battery Electric Vehicle
NIMEP	Net Indicated Mean Effective Pressure
BMEP	Brake Mean Effective Pressure
BMS	Battery Management System
BSFC	Brake Specific Fuel Consumption
BTE	Brake Thermal Efficiency
CAC	Charge Air Cooler
CAFE	Corporate Average Fuel Economy
CCE	Closed Cycle Efficiency
CDA	Cylinder Deactivation
C.I	Compression Ignition
COVID-19	Coronavirus Disease of 2019
ECM	Engine Control Module
EGR	Exhaust Gas Re-circulation
EVO	Exhaust Valve Opening
GDP	Gross Domestic Product
GHG	Greenhouse Gases
GIMEP	Gross Indicated Mean Effective Pressure
GPS	Global Positioning System
GT	Gamma Technologies
HEV	Hybrid Electric Vehicle
HP	Horsepower
I-70	Interstate 70
I-74	Interstate 74
I-75	Interstate 75

iEGR	Internal Exhaust gas Re-circulation
IHS	Information Handling Services
IMP	Intake Manifold Pressure
IVC	Intake Valve Closure
ME	Mechanical Efficiency
MPG	Miles Per Gallon
NHTSA	National Highway Traffic Safety Administration
NOx	Nitrogen Oxides
OCE	Open Cycle Efficiency
ORNL	Oak Ridge National Lab
PEL	Power Energy Logger
PMEP	Pumping Mean Effective Pressure
rpm	Rotations Per Minute
S.I	Spark Ignition
SOC	State Of Charge
TWC	Three-Way Catalyst
VVA	Variable Valve Actuation
VFD	Variable Frequency Drive

ABSTRACT

The commercial vehicle sector is an important enabler of the economy and is heavily dependent on fossil fuels. In the fight against climate change, reduction of emissions by improving fuel economy is a key step for the commercial vehicle sector. Improving fuel economy deals with reducing energy losses from fuel to the wheels. This study aims to analyze efficiency improvements for two systems that are important in reducing CO2 emissions - hybrid powertrains and natural gas engines. At first, a prototype series hybrid powertrain was analyzed based on on-highway data collected from its powertrain components. Work done per mile by the electrical components of the powertrain showed inefficient battery operation. The net energy delivery of the battery was close to zero at the end of the runs. This indicated battery was majorly used as an energy storage device. Roughly 15% of losses were observed in the power electronics to supply power from battery and generator to the motor. Ability of the hybrid system to capture regenerative energy and utilize it to propel the vehicle is a primary cause for fuel savings. The ability of this system to capture the regenerative energy was studied by modeling the system. The vehicle model demonstrated that the system was capturing most of the theoretically available regenerative energy. The thesis also demonstrates the possibility of reduction of vehicular level losses for the prototype truck. Drag and rolling resistance coefficients were estimated based on two coast down tests conducted. The ratio of captured regenerative to the drive energy energy for estimated drag and rolling resistant coefficients showed that the current system utilizes 4%-9% of its drive energy from the captured regenerative energy. Whereas a low mileage Peterbilt 579 truck could increase the energy capture ratio to 8%-18% for the same drive profile and route. Decrease in the truck's aerodynamic drag and rolling resistance can potentially improve the fuel benefits.

The second study aimed to reduce the engine level pumping losses for a natural gas spark ignition engine by cylinder deactivation (CDA). Spark ignited stoichiometric engines with an intake throttle valve encounter pumping/throttling losses at low speed, low loads due to the restriction of intake air by the throttle body. A simulation study for CDA on a six cylinder natural gas engine model was performed in GT- Power. The simulations were ran for steady

state operating points with a torque range 25-560 ftlbs and 1600 rpm. Two , three and four cylinders were deactivated in the simulation study. CDA showed significant fuel benefits with increase in brake thermal efficiency and reduction in brake specific fuel consumption depending on the number of deactivated cylinders. The fuel benefits tend to decrease with increase in torque. Engine cycle efficiencies were analyzed to investigate the efficiency improvements. The open cycle efficiency is the main contributor to the overall increase in the brake thermal efficiency. The work done by the engine to overcome the gas exchange during the intake and exhaust stroke is referred to the pumping losses. The reduction in pumping losses cause an improvement in the open cycle efficiency. By deactivating cylinders, the engine meets its low torque requirements by increase in the intake manifold pressure. Increased intake manifold pressure also resulted in reduction of the pumping loop indicating reduced pumping losses. A major limitation of the CDA strategy was ability to meet EGR fraction requirements. The increase in intake manifold pressure also caused a reduction in the delta pressure across the EGR valve. At higher torques with high EGR requirements CDA strategy was unable to meet the required EGR fraction targets. This limited the benefits of CDA to a specific torque range based on the number of deactivated cylinders. Some variable valve actuation strategies were suggested to overcome this challenge and extend the benefits of CDA for a greater torque range.

1. INTRODUCTION

1.1 Motivation

Climate change caused due to increase of greenhouse gases in the atmosphere, is a primary threat to our planet and human civilization. According to Gates [1] , to avoid serious impacts of climate change, the current greenhouse gas emissions of 51 billion tonne per year need to be brought down to zero. This number of 51 billion tonne of annual GHG emissions reduced by about 5% in the year 2020 due to a standstill in human activity caused by the COVID-19 pandemic. A drastic reduction in GHG emissions at the expense of dire consequences to world economy and human livelihood is not ideal. To tackle climate change, efforts on improving the current energy pathways are critical.

World energy demands keep on rising. The high dependence on fossil fuels to meet energy demands is due to high energy density, reliability and cost. If left unchecked, there is a threat that non-renewable sources would be exhausted. Figure 1.1 indicates that the rate of finding new oil reserves is a constant at 1600 billion barrels for the past decade [2]. On the contrary, world petroleum consumption has kept on rising and doesn't show any significant signs to slow down. It can be estimated that the oil reserves can be exhausted in the next 60 years if the current trends continue. Hence, there is an urgency to work on better energy utilization and improve efficiencies of existing technologies dependant on fossil fuels.

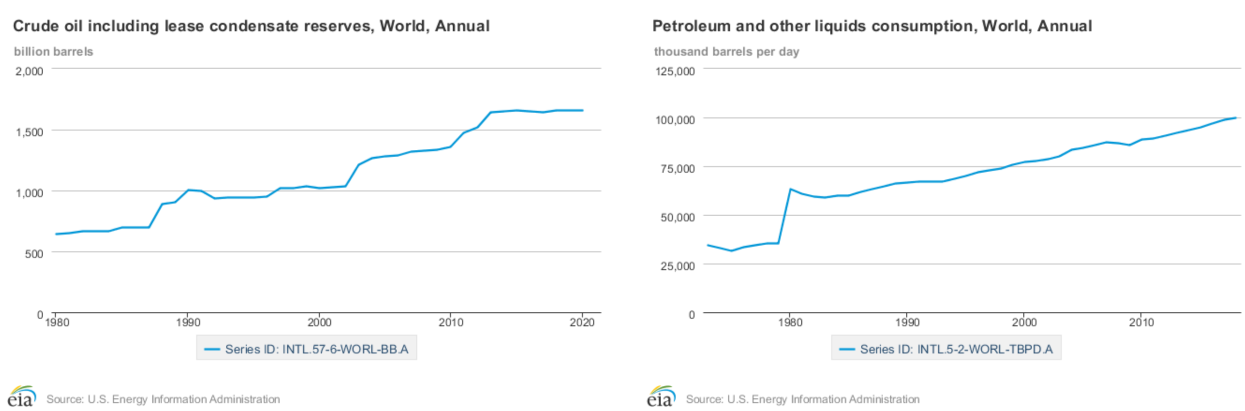

(a) World Oil Reserves

(b) World Oil Consumption

Figure 1.1. World Oil Reserves and Consumption

1.1.1 Commercial Vehicle Space

Commercial vehicles play an important role in enabling the world economy, and is significantly dependent on fossil fuels like diesel and natural gas. The trucking industry in the US employs 7.1 million people and responsible for 80% of total cargo movement [3]. There is strong correlation between GDP and commercial vehicles sold for any country. While the transportation sector accounts for 28% of the total GHG emissions, medium and heavy-duty trucks account for the second highest emissions after light duty vehicles [4].

The commercial vehicle market by fuel type is shown in Figure 1.2. The medium and heavy-duty market is dominated by diesel. The share of diesel powered medium and duty trucks is expected to decrease to 66% in 2040 compared to 80% in the US today, per findings of the IHS Markit study [5]. Although, the BEV has made a significant entry in the light-duty passenger segment, the adoption of battery technology is difficult in the medium-heavy duty segment accounting to the lower energy density of batteries. Natural gas fueled trucks, having the advantage of low NOx emissions would be the second most sold fuel type of commercial vehicles. Hybrid powetrains and hydrogen fuel cell powered vehicles are expected to increase their market share as well.

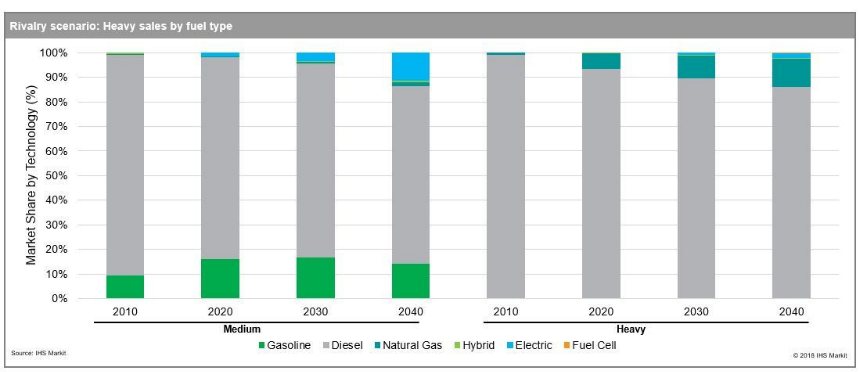

Figure 1.2. Commercial vehicle market by fuel type

With huge implications on the overall GHG emissions as well as dependence on fossil fuels, regulators are keen to save every drop of fuel by implementing aggressive regulations in the commercial vehicle space.

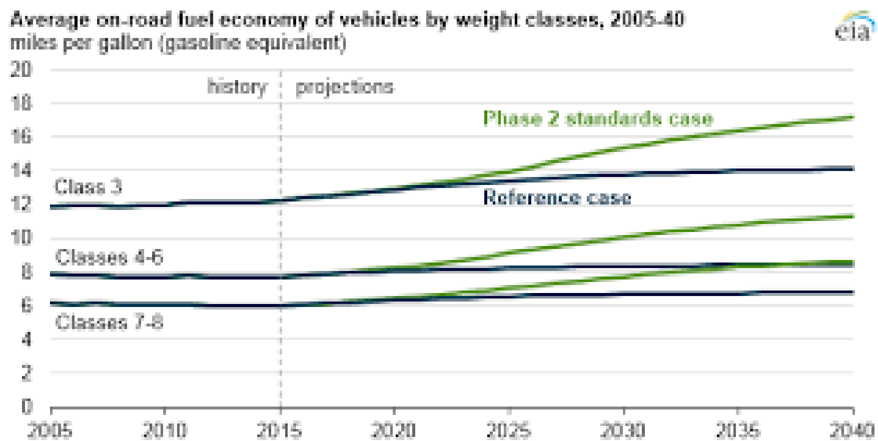

Figure 1.3. CAFE standards for fuel economy

1.1.2 Homologation Requirements

Government bodies across the globe implement rules and regulations to keep the fuel usage and emissions in check. NHTSA's Corporate Average Fuel Economy (CAFÉ) standards are implemented with an aim to reduce the energy consumption by increasing fuel economy of vehicles [6]. The CAFÉ program requires all the manufacturers of passenger cars and truck to meet the CAFÉ standards of fuel economy. The CAFE standards are to be implemented in 2 phases, as shown in Figure 1.3. For class 7-8, heavy-duty vehicles the current MPG standards lie around 6 miles per gallon and is expected to be around 8 miles per gallon in Phase 2.

Adherence to the homologation requirements serves as an external pressure not only on engine manufacturers but also vehicle manufacturers. These external pressures have generated a need to keep exploring methods of efficiency improvement on engine level, powertrain level and vehicle level.

1.1.3 Technology Development

Based on the homologation requirements and to conform with the regulations, OEM's are investing in all technology developments. For the commercial vehicle segment, reduction in NOx and CO2 emissions are the primary drivers for new technology development and adop-

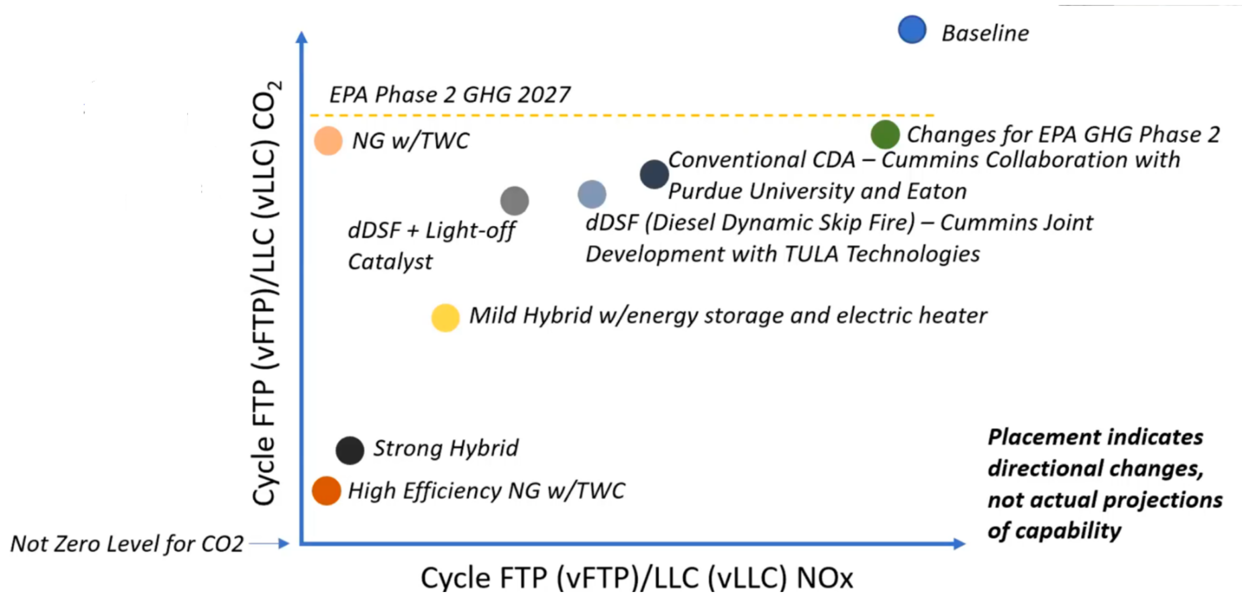

Figure 1.4. Technology transition to meet emission regulations [7]

tion. Figure 1.4 shows a placement of different engine powertrain development technologies undertaken by Cummins Inc. based on the CO2 and NOx emission reduction capability with respect to each other [7]. Yellow line signifies the Phase 2 of the GHG emission norms set by EPA, to be implemented in 2027. Many technologies can conform to these norms. Conventional CDA on diesel engines using valvetrain flexibility has demonstrated to have significant fuel benefits by previous colleagues at Purdue [8],[9],[10].

High efficiency natural gas engines along with strong hybrid powertrains are projected to provide the best results for ultra low NOx and CO2 emmissions. These two technologies that lie at the bottom of the Technology transition Figure 1.4 are the basis of this thesis work.

1.2 Objective

The following study investigates efficiency improvement for the commercial vehicle industry by exploring two different systems. One on the powertrain and vehicle system level and the other on the engine level. Both systems are pathways to reduced CO2 emissions along with improved fuel economy.

(A) Series hybrid powertrain of a class 8 truck.

A prototype class 8 truck with a series hybrid powertrain was developed by a startup based in Florence, Kentucky. The objectives of the study were to collect and analyze data from the on-highway tests, understand behaviour of the powertrain components, give insights on the powertrain efficiencies , model the system for analyzing system level losses and recommend any additions or betterment for future development.

(B) Natural Gas engine for medium duty applications.

A simulation based analysis of the B6.7N Cummins natural gas engine was demonstrated. The overall objective was to demonstrate the capabilities of different valvetrain flexibility strategies in simulation as a precursor to experimental work in an Engine test cell. This study specifically discusses the Cylinder Deactivation strategy implemented on the engine 1D simulation model to analyze its effects on efficiency improvements.

Both the studies had the common goal of analyzing efficiency improvements , although one focused on a vehicular level and other on the engine level.

1.2.1 Other Contributions

Apart from the above mentioned work, the author also worked on building the engine test cell for natural gas capabilities, and its baseline testing at Herrick Laboratories at Purdue University.

1.3 Background

1.3.1 Hybrid Powertrain

An engine aided with a battery electric power to drive the wheels of a vehicle is called a hybrid powertrain [11]. Depending on how the power is split between the engine and battery, hybrid powertrains are broadly classified as parallel, series and series-parallel split hybrid powertrain. The series and hyrid architectures are shown in Figure 1.5 and 1.6. In parallel hybrids, the final drive can be driven independently by an engine and an electric motor. In series hybrid systems, the final drive is by the electric motor. The electrical energy supplied to the motor is by a battery source or by a generator run by an engine.

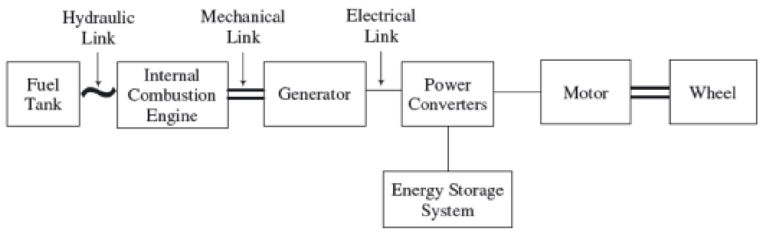

Figure 1.5. Series Hybrid Architecture

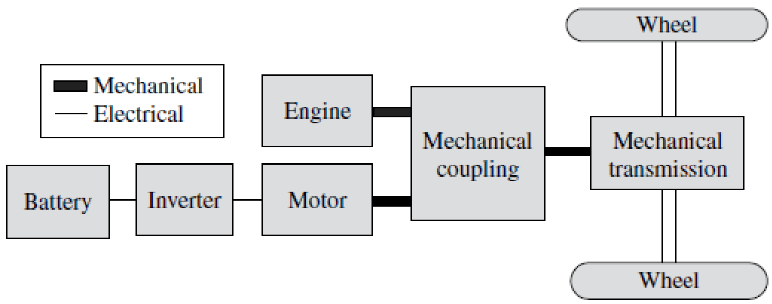

Figure 1.6. Parallel Hybrid Architecture

In both cases, the hybrid powertrain helps the engine to operate efficiently. The engine operation is inefficient in certain applications like idling and stop-and-go. The major advantages of HEV's is enabling an optimized engine operation. The battery power can be utilized during idling or stops. Optimized engine operation means not only fuel savings but also reduced emissions. Use of hybrid powertrain also enables down-sizing of the engine to meet the same power demands.

Another major advantage of incorporating a hybrid powertrain is the ability to capture kinetic energy during braking also called as regenerative energy. An energy storage device like a battery stores this regenerative energy during baking and can be used again to propel the vehicle.

1.3.2 S.I Engine Limitations

A typical spark ignited natural gas engine torque curve is shown in Figure 1.7. The torque curve demonstrates operating points of the engine. Based on the engine operation / torque curve, the performance limitations of a spark ignited engine can be broadly classified into three zones :

(i) Part load throttling losses at low loads

(ii) Knock at high rpm and

(iii) Fuel Enrichment at high load high rpm regions.

The spark ignited engines have stoichiometric operation, defined as operation with a constant air to fuel ratio. A fixed air-to-fuel ratio means as load demand increases, both the fuel flow and air flow are raised to meet increased load demands.

Unlike C.I engines , where the air-fuel-ratio is varied to meet varied torque demands, S.I engines have stoichiometric operation by deploying a throttle valve at the intake manifold to control varying loads. The throttle valve restricts the air flow when the engine is operating at low loads. Restricting intake air flow results is engine doing more work in pumping gases. The losses incurred at low loads are called part load throttling losses. The study focuses on tackling these losses through implementation of valvetrain strategy of cylinder deactivation.

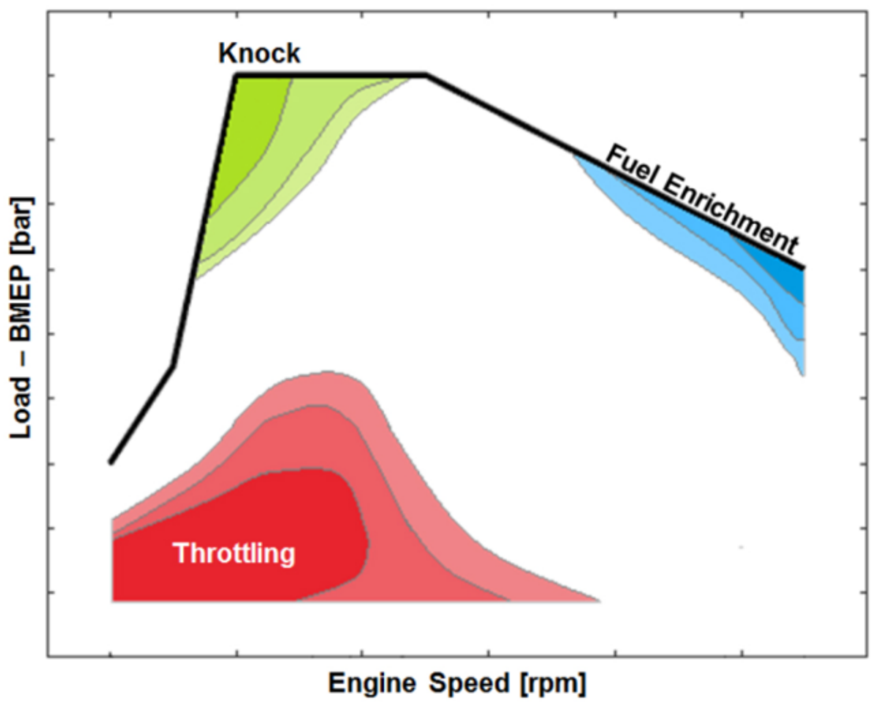

Figure 1.7. P-V diagram for a four-stroke S.I engine

2. SYSTEM DESCRIPTION

This chapter will describe the 2 systems in consideration for efficiency evaluation. First a detailed overview of the system architecture of the Series Hybrid Powertrain of class 8 truck is given and then details of the B6.7N Natural Gas engine is discussed. This engine would be experimentally run in the Purdue Herrick Lab test cell facility. Although the thesis discusses simulation of the engine it is necessary to understand the experimental setup and working of the system. The chapter also discusses the VVA system at Purdue university which would be used for experimental testing of valvetrain flexibility strategies like CDA discussed in the thesis.

2.1 Series Hybrid Powertrain for a Class 8 Prototype Truck

A class 8 sleeper cab truck was modified by converting the I.C engine powertrain to a series hybrid powertrain. This prototype truck was used for on-highway testing. The series hybrid powertrain has a 6.7-liter diesel engine, a three-phase synchronous AC generator, a three-phase 200 HP induction motor, a lithium-ion battery pack constructed from two 85-kWh Tesla Model 3 battery packs connected in series and a 10 speed transmission gearbox. The details of the powertrain components are given in the Table 2.1.

The engine drives the generator via a mechanical coupling. The generator generates the electrical energy which is complimented by the electrical energy supplied by the battery. The power electronics box houses the variable frequency drive (VFD). A control algorithm implemented by the Power electronics decides the percentage of generator and battery energy supplied to drive the motor as well as energy stored in the battery during regeneration.

Table 2.1. Prototype Truck Series Hybrid Powertrain Components

Component	Details
Engine	Cummins ISB 6.7L C.I Engine
Generator	Marathon 3 Phase Synchronous AC Generator
Motor	Marathon 200 HP Induction Motor
Battery	Tesla Model 3
Transmission	Eaton Ultra Shift 10 Speed RTO- 16910

The system was equipped with data acquisition system for all electric components of the powertrain as seen in Figure 2.1. A PEL103 Power and Energy data logger measured the electric current and voltage on the 3 phase electric machines to derive power.These data loggers connected to the electric machines were on board in the truck and captured real time data during the on-highway tests. A TESLA Battery management system (BMS) measured the battery state of charge, current and voltage. Apart from the electric component data loggers, the truck was also equipped with a GPS based speed and position sensor to log truck velocity and position in 3 dimensions.

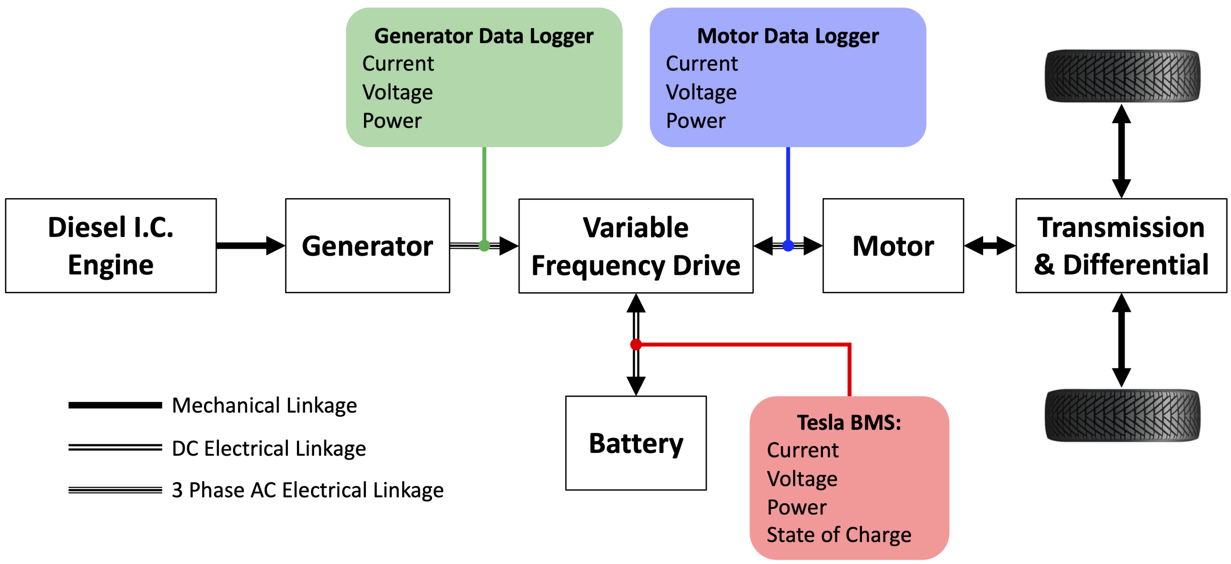

Figure 2.1. Series hybrid system diagram

Being a series hybrid, the focus of analysis is in the electrical energy flow. A simplified system diagram is used as shown in Figure 2.2 to highlight the electric energy pathways. The variable frequency drive and power controller are together coupled to represent the power electronics block.

The propulsive power flow to the motor and discharge power from the battery corresponds to positive power for notation. Similarly, the regenerative power flow motor and charge to the battery corresponds to negative power flow.

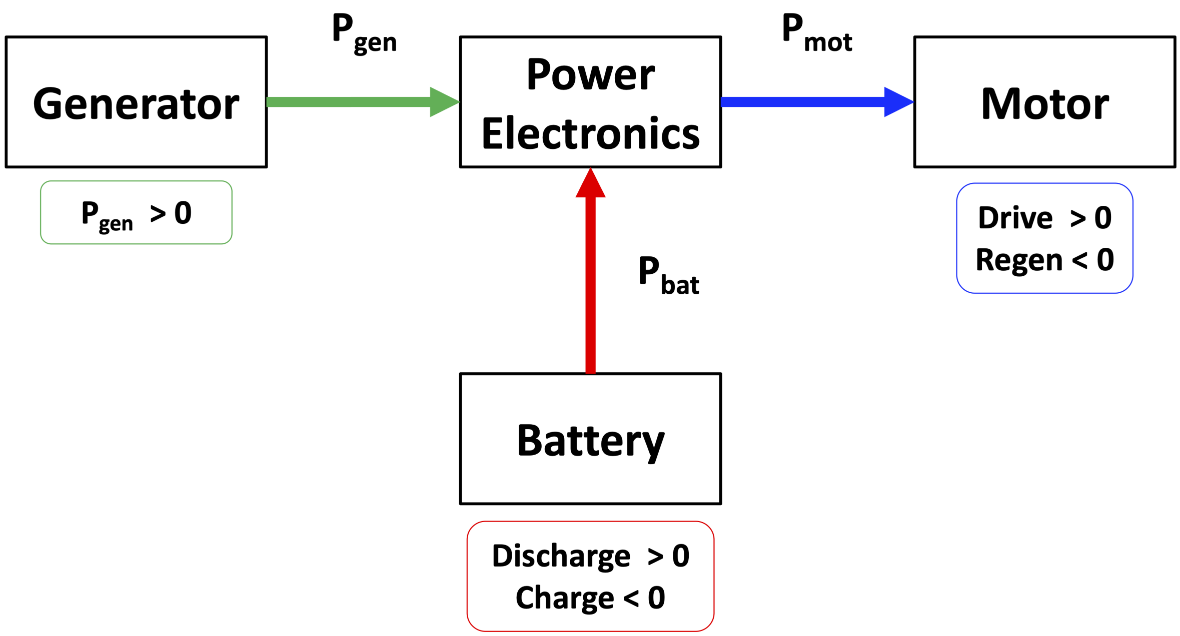

Figure 2.2. Simplified system block diagram showing selected reference directions

Table 2.2. Engine Specification

Model	B6.7N
Displacement	6.7 litre
Maximum Horsepower	240HP / 179KW
Peak Torque	560lb-ft / 759Nm

2.2 Natural Gas Engine

The engine in evaluation is a Cummins Westport Inc. make, six cylinder, stoichiometric spark-ignited, natural gas combustion engine. The B6.7N is equipped with a cooled EGR, charge air cooler (CAC), wastegate turbocharger and a TWC for aftertreatment.The engine specifications are shown in Table 2.2.

Figure 2.3 shows the schematic details of the engine. The engine schematic is representative of the GT Power model used for simulation. The engine has a split exhaust manifold to drive exhaust gas through the EGR loop and through the wastegate to the TWC. The boost-pressure controller actuates the wastegate valve to drive the turbine of the turbocharger. The turbine is connected to the compressor which compresses the air that boosts the inlet air pressure to meet elevated torque demands. The compressed intake air is passed through a charge-air-cooler (CAC) system to decreases its temperature before entering the intake manifold. Demanded torque is controlled by the torque controller by actuating the intake throttle valve. A stoichiometric AFR controller actuates the fuel injector to maintain a air-to-fuel ratio of 12.7. The exhaust re-circulation loop has an EGR fraction controller to control the EGR valve to meet the EGR fraction demands.

2.3 Variable Valve Actuation System

The VVA system is a full flexible camless valve actuater which allows full control of valve events of the engine. It has electro-hydraulic linear actuators for each intake and exhaust valve pair. The VVA system is shown in Figure 2.4. It is important to note that the VVA system is used for experimental testing of VVA strategies like CDA. For the purpose of this work, the VVA strategies were implemented in simulation environment. Knowing

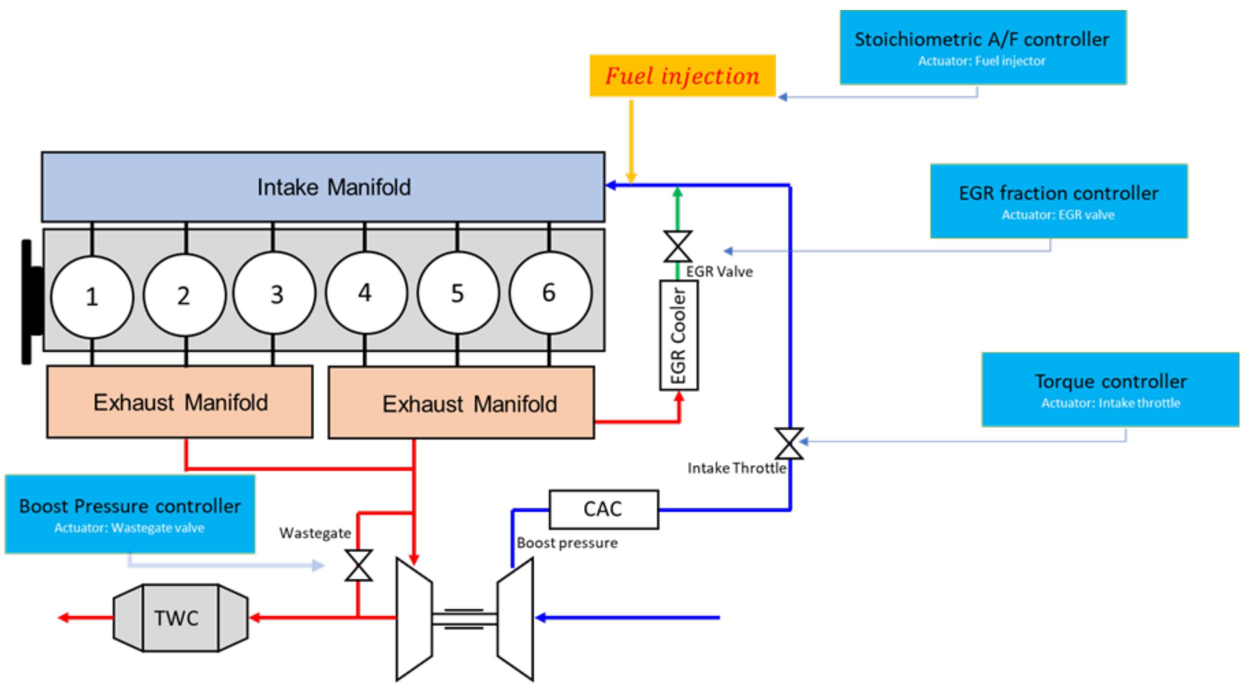

Figure 2.3. Engine schematic

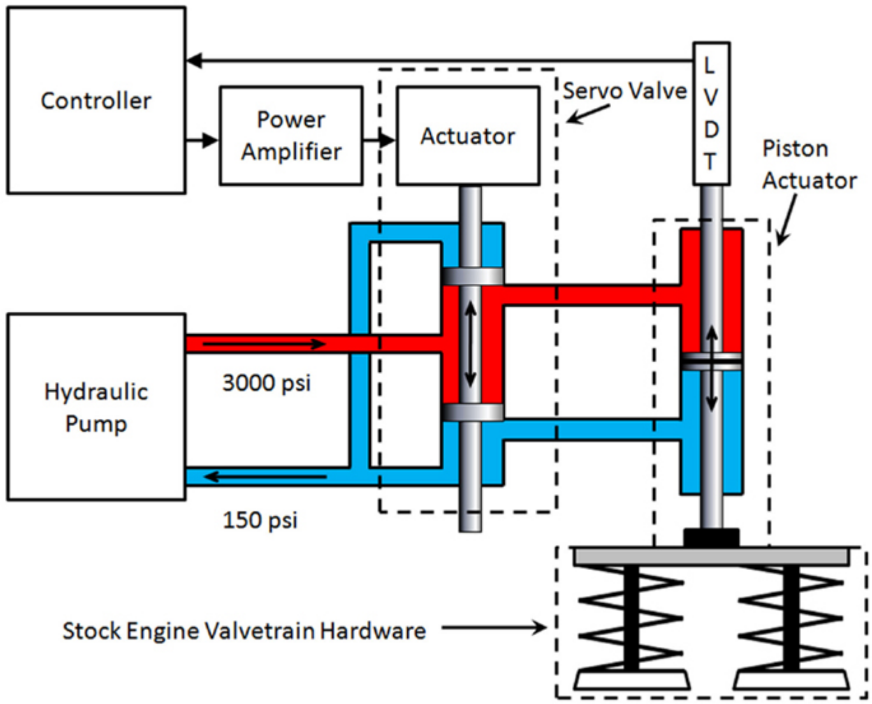

Figure 2.4. VVA system

the physical VVA system is essential to understand the real world implementation of the simulation analysis.

3. METHODOLOGY

This chapter covers the on-highway testing conducted between October 2019 and January 2020 over two routes for a range of payload weights. This chapter also covers the GT-Power model Setup for the simulation of cylinder deactivation of the natural gas engine.

3.1 On-highway Testing of Class 8 Truck

The prototype truck was equipped with data acquisition systems to collect real time data during on-highway tests. In total, 21 highway tests were conducted, in addition to 2 coast-down tests.

3.1.1 Data Collection Routes

The prototype truck has an application as a freight carrier and hence routes were selected along Interstate Highways in Indiana and Kentucky representing freight paths. The hybrid system with a capability to capture regenerative energy during downhill or braking performs differently on a flat road vs hilly conditions. The selected routes provided these different conditions.

Lexington Test Route

The first set of testing was conducted on I-75 in Kentucky from Florence to Lexington as shown in Figure 3.1. This route covered a distance of 100kms and could be covered multiple times in a single test day. This test route has small ups and downs due to some hilly terrains which can be seen in the grade plot in Figure 3.2. This allowed the hybrid system to capture regenerative energy in downhill segments.

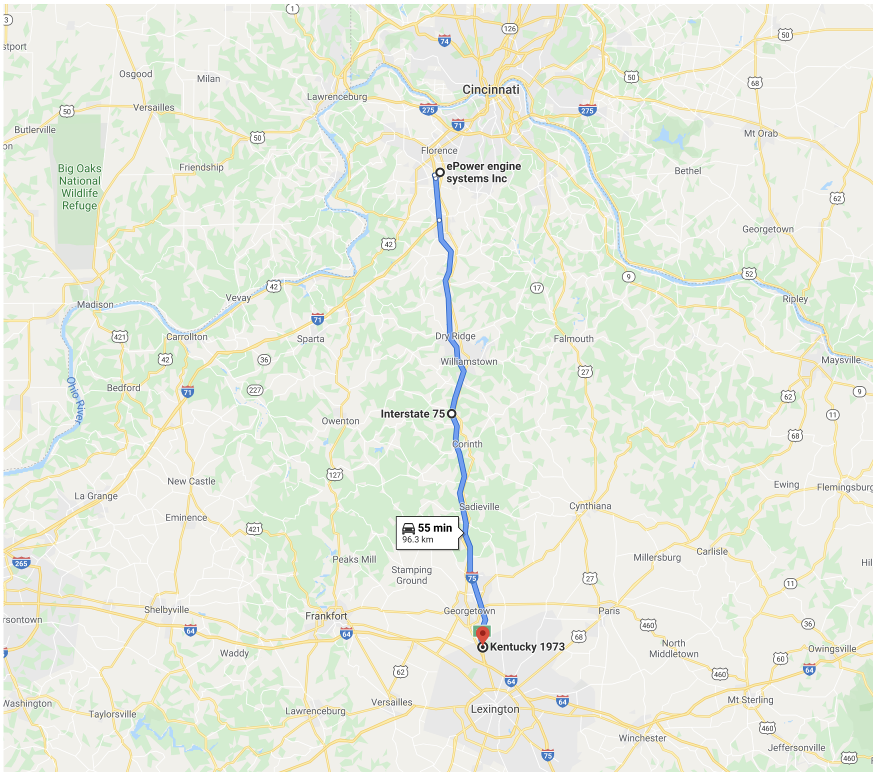

Figure 3.1. Lexington Route

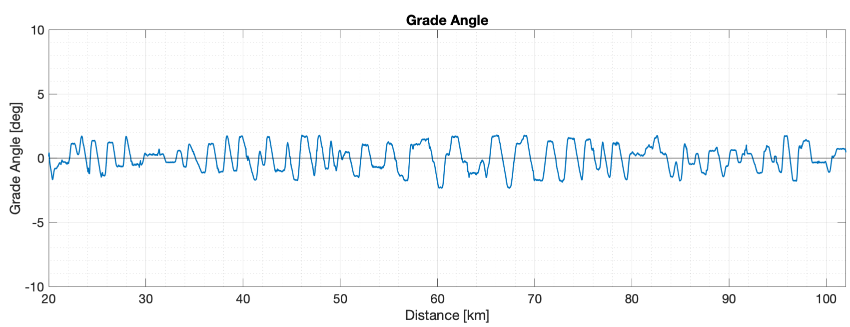

Figure 3.2. Lexington test route grade angle (degrees)

Indianapolis Test Route

The Indianapolis test route shown in Figure 3.3 was on I-74 and I-70 in Indiana and covered a distance of roughly 140kms. This route is flatter as seen from the grade plot 3.4 and did not provide many opportunities for the hybrid powertrain to capture the regenerative energy.

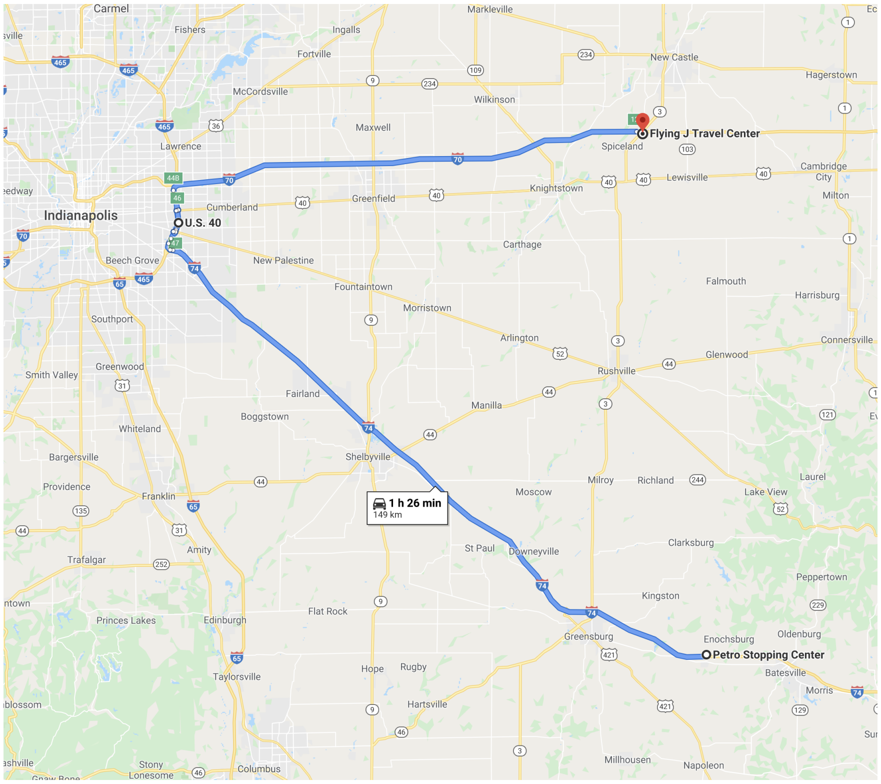

Figure 3.3. Indianapolis test route grade angle (degrees)

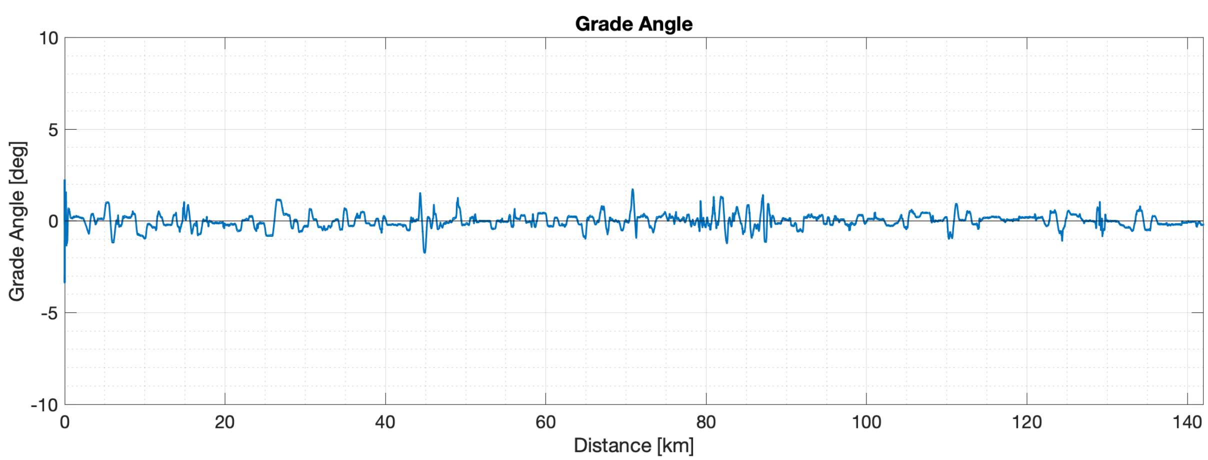

Figure 3.4. Indianapolis test route grade angle (degrees)

Data Sets

A total of 21 on highway test were performed that are summarized in the Table 3.1. However, some tests had battery timestamp recordings incorrect and a test with GPS data missing which made 10 of the 21 tests usable for analysis.

Table 3.1. List of On-Highway Test Runs

Date	Route	Weight [lb]	Data Anomalies
27 September 2019	Lexington	52,720	
10 October 2019	Lexington	52,720	
14 October 2019	Lexington	52,720	
15 October 2019	Lexington	55,800	
16 October 2019	Lexington	55,800	BMS timestamp jumps
17 October 2019	Lexington	55,800	BMS timestamp jumps
18 October 2019	Lexington	55,800	BMS timestamp jumps
19 October 2019	Lexington	55,800	BMS timestamp jumps
20 October 2019	Lexington	55,800	BMS timestamp jumps
22 October 2019	Lexington	55,800	
23 October 2019	Lexington	55,800	
24 October 2019	Lexington	60,120	
28 October 2019	Lexington	60,120	BMS timestamp jumps
29 October 2019	Lexington	60,120	BMS timestamps rounded to nearest minute
1 November 2019	Lexington	60,120	BMS timestamp jumps
2 November 2019	Lexington	60,120	BMS timestamp jumps
4 November 2019	Lexington	60,120	GPS data missing after 2.5 hours
9 January 2020	Indianapolis	58,200	
13 January 2020	Indianapolis	55,800	
14 January 2020	Indianapolis	55,800	BMS timestamp jumps & missing generator data after 1 hour
20 January 2020	Indianapolis	55,800	BMS timestamp jumps & generator data doesn't appear to match

3.1.2 Coast Down Tests

In addition to the on-highway tests, 2 coast down tests were performed for estimating the truck's drag coefficient, C_d, and rolling resistance coefficient, μ. These were important parameters that were used for the modeling of the truck to analyze system efficiency losses, explained in the chapter Systems Modeling. In each test, the vehicle was accelerated to an initial velocity (40 and 50mph in this case) and allowed to coast to stop on a near-level roadway. Ideally the test should be on a flat road and similar to the on-highway conditions. The road on the US-42 West Kentucky was chosen with a 2km straight section, as shown in Figure 3.5.

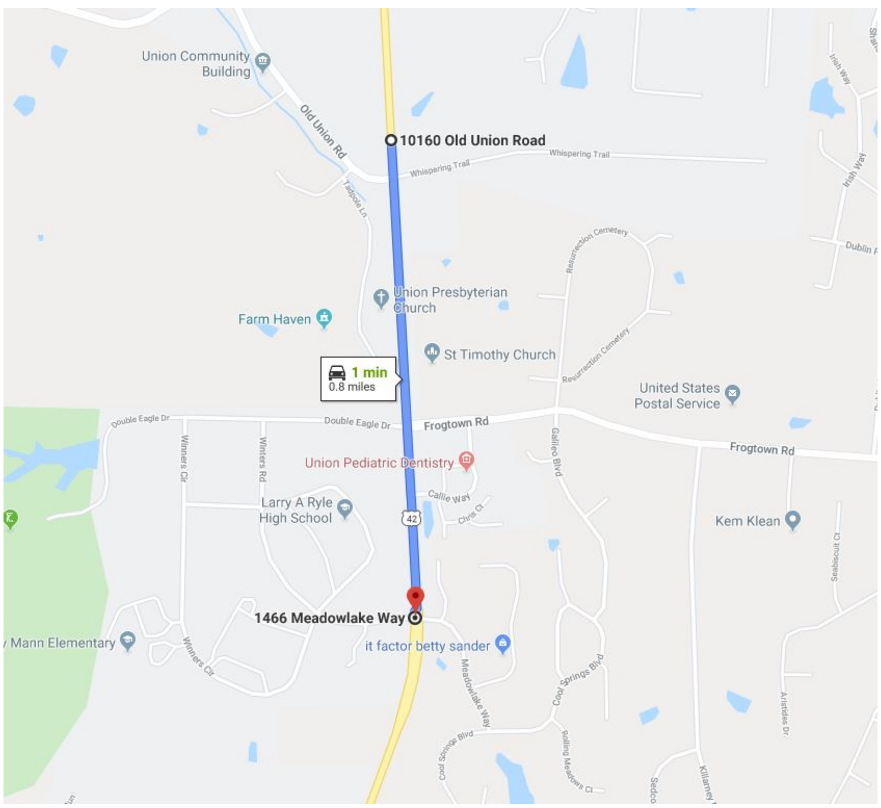

Figure 3.5. Coast-down test route map for US-42 W

3.2 GT Power Simulation

GT-Power is a system level simulation software by Gamma Technologies used by engine manufacturer's for engine performance simulation. It is a multi-physics 1-D simulation tool. 1D simulation tools have significant advantages in reducing the computational time in comparison to 3D simulations, demand less computing power and a good first step for engine design and performance testing. The author's research team was provided with a GT-Power model developed by the sponsors with an objective to run simulations of valve-train flexibility strategies and analyze its effects on efficiency improvements.

3.2.1 Model Setup

The GT-Power model schematic shown in Figure 3.6 is representative of the engine discussed in section 2.2. The model contains submodels of the mixer, intake manifold, intake-exhaust valves connecting the short block/engine block, exhaust manifold, charge air cooler, EGR loop and a turbocharger. The model doesn't include the after-treatment system. It also incorporates four controllers - Turbo-wastegate controller, EGR valve controller, A-F ratio controller and a throttle controller which are stock GT-Power templates.

Simulation inputs were targets for the controllers. AFR was fixed with a value 12.7. To concentrate the efforts , engine speed was kept constant at 1600 rpm for all simulation runs. Desired torque was varied from 25ftlbs to 560lbs. The EGR fraction targets corresponding to full load condition was known to be 22%. EGR targets were interpolated based on the torque values and verified that the EGR controller attained steady state for 6-cylinder firing, Baseline simulations. The engine is naturally aspirated in the torque region of 25-125ftlbs and needs boosting at loads above 125ftlbs in the 6-Cylinder firing, baseline operation. The boost pressure targets were varied manually for each case to ensure stable operation of the Turbo-wastegate controller.

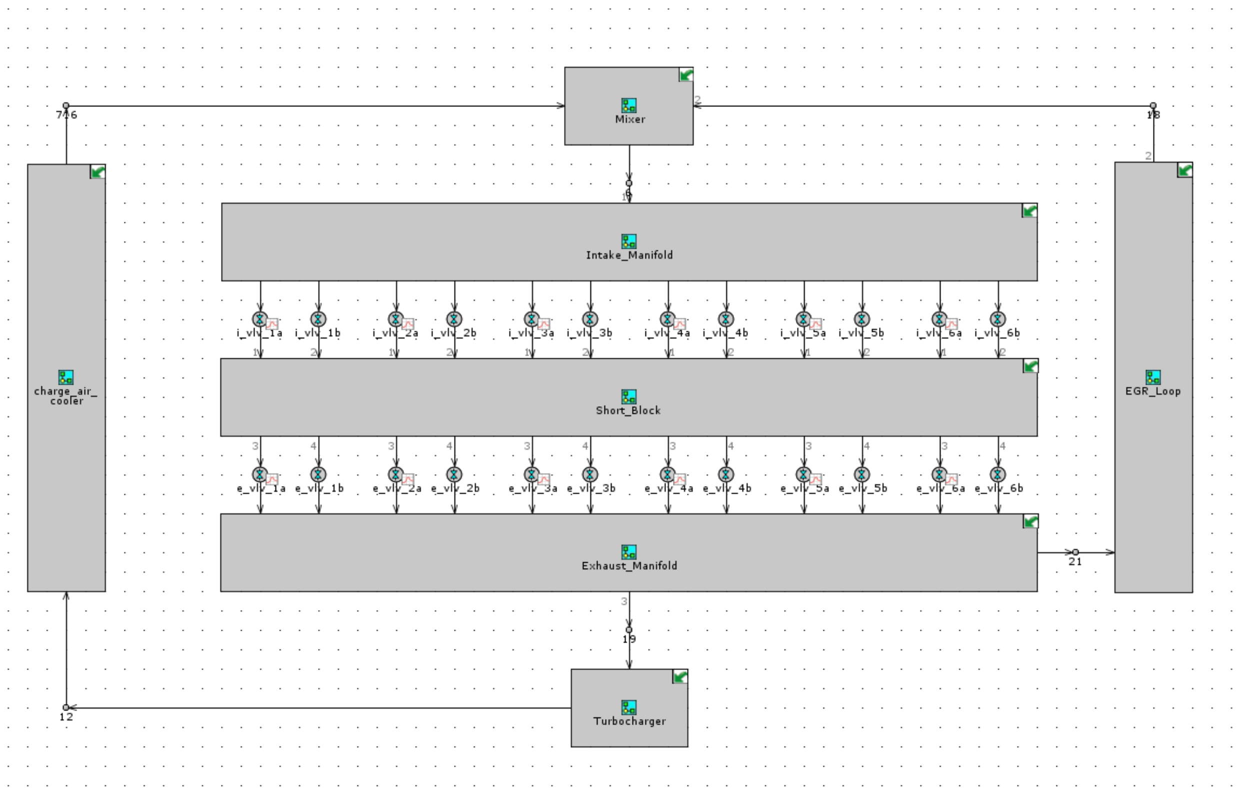

Figure 3.6. Simulation model in GT-Power

3.2.2 Data Set

The model was ran for steady state data points at a constant 1600 rpm engine speed and a torque range of 25ftlbs to 560ftlbs. The simulation points ran are summarized in table 3.2.

Table 3.2. GT-Power Steady State Simulation Test Points

Sr. No.	Torque[ftlbs]	Speed[rpm]	EGR fraction [percent]
1	25	1600	6.10
2	50	1600	6.88
3	75	1600	7.66
4	100	1600	8.44
5	125	1600	9.22
6	150	1600	9.99
7	200	1600	11.54
8	250	1600	13.11
9	300	1600	14.65
10	350	1600	16.22
11	400	1600	17.76
12	450	1600	19.33
13	500	1600	20.87
14	560	1600	22.75

3.2.3 Limitations

The simulation model has its limitations and its primary role is to provide a foundation for design of experiments for engine testing in the test cell.

The primary limitation of the model is that for all the simulation cases, there is a constant Heat release rate that is imposed. The constant heat release rate shown in Figure 3.7 is imposed in the initial model setup. This implies that the combustion and heat exchange analysis may not be truly representative of the engine operation. This affects the analysis of the closed cycle efficiency.

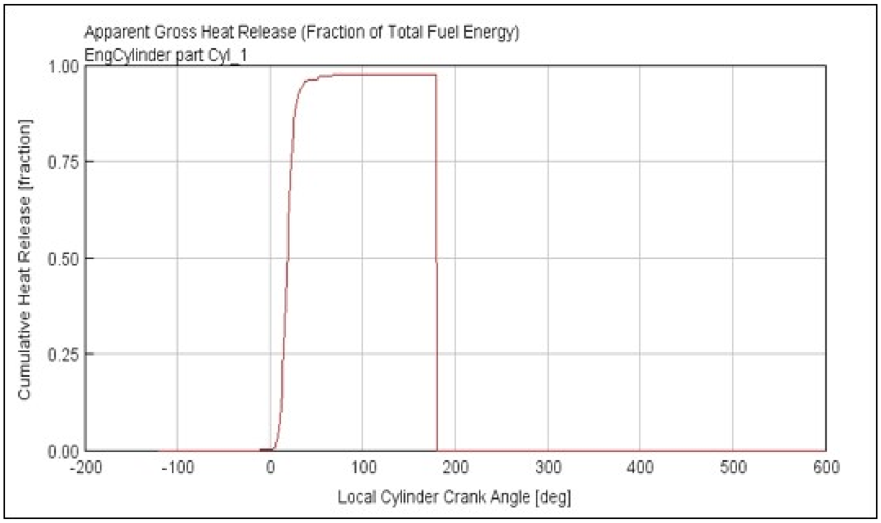

Figure 3.7. Imposed heat release rate

3.2.4 CDA Setup

Intake and exhaust valves are modeled for all the cylinders. Independent valve models gives the capability to run valvetrain flexibility strategies in the simulation environment. Valve profiles are the inputs to the GT-Power setup file. For cylinder deactivation, valve lifts of the deactivated cylinders are input as zero . Flat valve profile with zero lift results in no firing in the deactivated cylinders as can be seen from the in-cylinder results from the GT-Post (post processing) file.

3.2.5 Cycle Efficiency

Engine efficiency can be determined by analyzing the cycle efficiencies of the four stroke spark ignition engine. The overall efficiency also called the brake thermal efficiency (BTE) of the engine is defined as the total output per input fuel energy. [12]

$$\eta_{thermal} = \frac{P_{brake}}{\dot{m} * Q_{lhv}} \tag{3.1}$$

P_{brake} is the output brake power, is the mass flow rate and Q_{lhv} is the lower heating value of the fuel. The above equation 3.1 is helpful during engine testing when the output power is being measured on a dynamometer and accurate measurements of fuel flow rates can be made. The composition of a natural gas as fuel may vary slightly depending where the refueling is done which may affect the lower heating value of the fuel.

Hence, another method to determine the BTE of the engine is based on thermodynamic processes of the four stroke spark ignited engine. The BTE can be expressed as :

$$\eta_{thermal} = \eta_{closed} * \eta_{open} * \eta_{mechanical} \tag{3.2}$$

where η_{open}, η_{closed} and $\eta_{mechanical}$ is the Open Cycle Efficiency (OCE), Closed cycle efficiency (CCE) and Mechanical Efficiency (ME), respectively. The Pressure-Volume plot in 3.8 demonstrates a four stroke s.i engine cycle. The area represented as +W indicating work done by the system signifies the closed cycle. Closed cycle is the time period when both valves are closed i.e from IVC to EVO in Figure 3.8 and open cycle is the time period where both intake and valves are open. The area represented as -W is the open cycle, where engine has to overcome work to transfer working fluid.

Based on the PV plot, gross indicated mean effective pressure, pumping mean effective pressure and net indicated mean effective pressure are defined as-

$$GIMEP = \frac{Area_{ClosedLoop}}{V_d} \tag{3.3}$$

$$PMEP = \frac{Area_{OpenLoop}}{V_d} \tag{3.4}$$

$$NIMEP = GIMEP - PMEP \tag{3.5}$$

where Vd is the volumetric displacement of the engine.

The closed cycle efficiency represents the efficiency during the combustion process and is calculated as :

$$\eta_{closed} = \frac{GIMEP * V_d}{\dot{m} * Q_{lhv}} \tag{3.6}$$

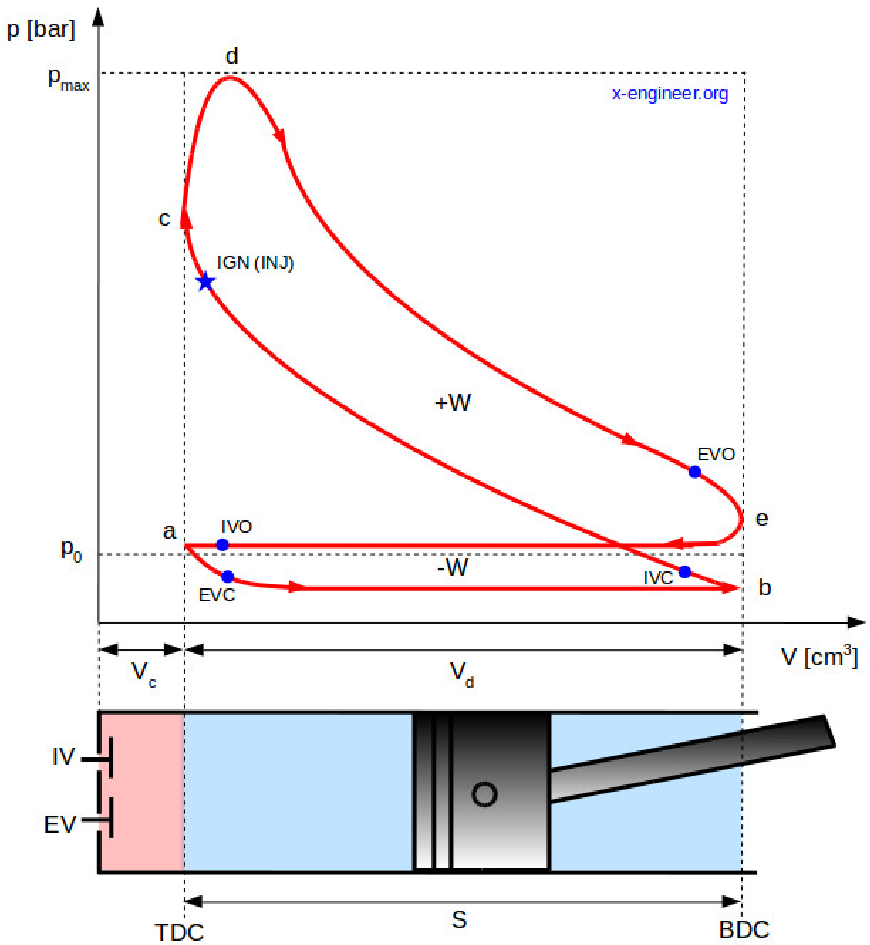

Figure 3.8. P - V diagram for a four stroke S.I engine

The Open cycle efficiency is related to the pumping of gases. The open cycle efficiency is defined as the ability of the engine to transfer the charge into and out of the cylinder.

$$\eta_{open} = 1 + \frac{PMEP}{GMEP} \tag{3.7}$$

The mechanical efficiency takes into account the mechanical losses associated with the working of the engine like friction. It is given as :

$$\eta_{mechanical} = \frac{BMEP}{NIMEP} \tag{3.8}$$

where BMEP is the Brake Mean Effective Pressure.

The above equations 3.2 to 3.8 are used to analyze the natural gas s.i engine efficiencies.

4. CLASS 8 HYBRID ON-HIGHWAY TEST RESULTS

This chapter details the results and analysis of the on-highway tests for class 8 hybrid prototype truck. The results of this chapter lay a foundation for the modeling of the system for the next chapter.

4.1 Component Energy Flows

In the series hybrid powertrain, the generator driven by the engine provides most of the required propulsive energy, aided by the battery to the drive motor. A snippet of the power-flows through a 4km section of the Lexington and Indianapolis route are shown in Figures 4.1 and 4.2, respectively. The behaviour of the system can be understood based on the power flows and can broadly be classified into three power modes.

(i) Drive mode : When motor power is positive and generator and and battery are providing positive power to the motor. This can be easily seen during highway cruise conditions or constant peak motor power.

(ii) Regen Mode : When motor power is negative, battery power is negative indicating battery charging. Here, generator power is always positive and thus during battery charging, both generator and motor provide the charging power.

(iii) Drive + charge mode : When motor power is positive indicating drive and battery power is negative indicating charging. Here, the generator provides power simulatneously to the motor and battery. This phenomenon can be seen at roughly 24km distance in Figure 4.1.

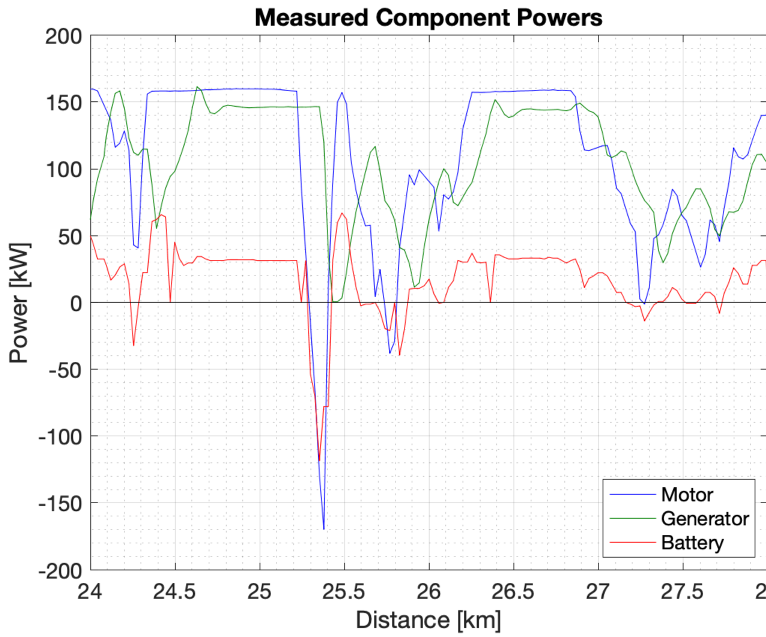

(a) Motor, generator, and battery power

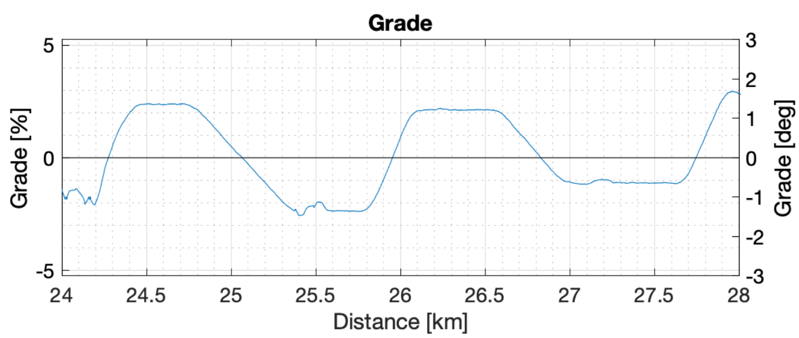

(b) Grade

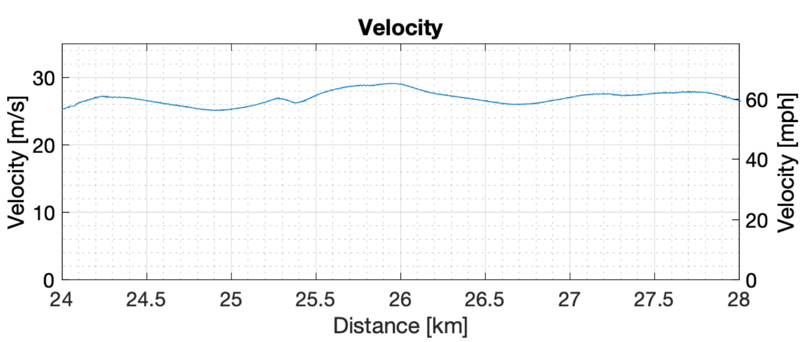

(c) Velocity

Figure 4.1. Power flows and drive cycle conditions for 4 km of Lexington route on 10 October

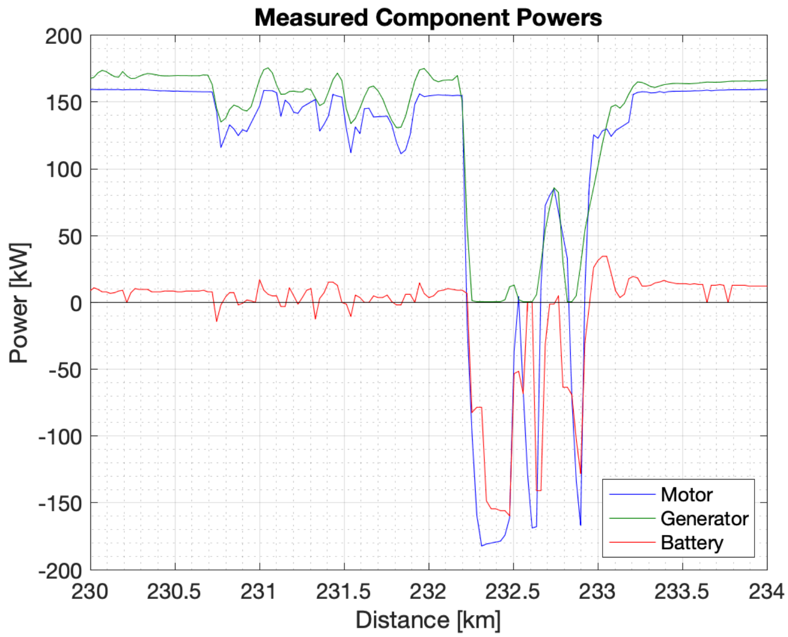

(a) Motor, generator, and battery power

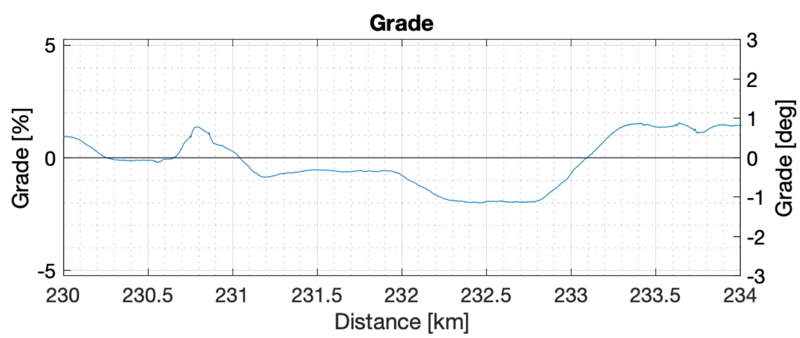

(b) Grade

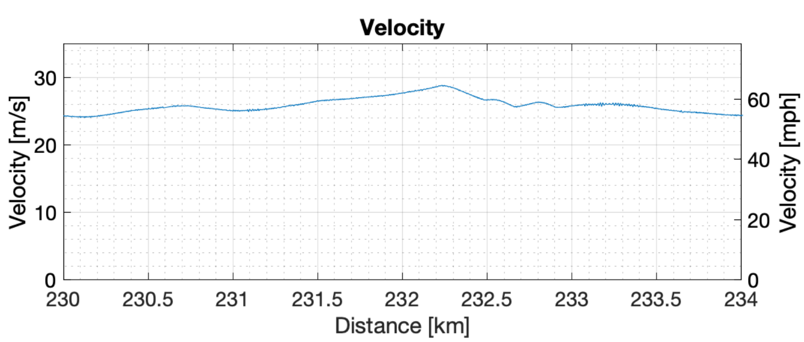

(c) Velocity

Figure 4.2. Power flows and drive cycle conditions for 4 km of Lexington route on 9 January

The power plots give an idea of the instantaneous performance of the system. For further analysis, the energy contributions of the drive components are determined by integrating the power data according to Equation 4.1.

$$E(t) = \int_0^t P(\tau) d\tau \tag{4.1}$$

where $E(t)$ is the net energy from start of the run to time $\boldsymbol{t}$, $P(\tau)$ is the measured power into or out of the component of interest, $d\tau$ is the time step (1 second for most data loggers) .

4.1.1 Generator

The generator provides most of the electrical energy to propel the system and its direct coupling with the engine helps in tracking the power demand from the engine ECM. Figure 4.3 shows the power range of 0 to 160kW for the generator which is similar to the Engine Load curve from Figure 4.4. The highlight of this arrangement is the engine operating speed which remains around the 1800 rpm value, enabling efficient operation of the engine.

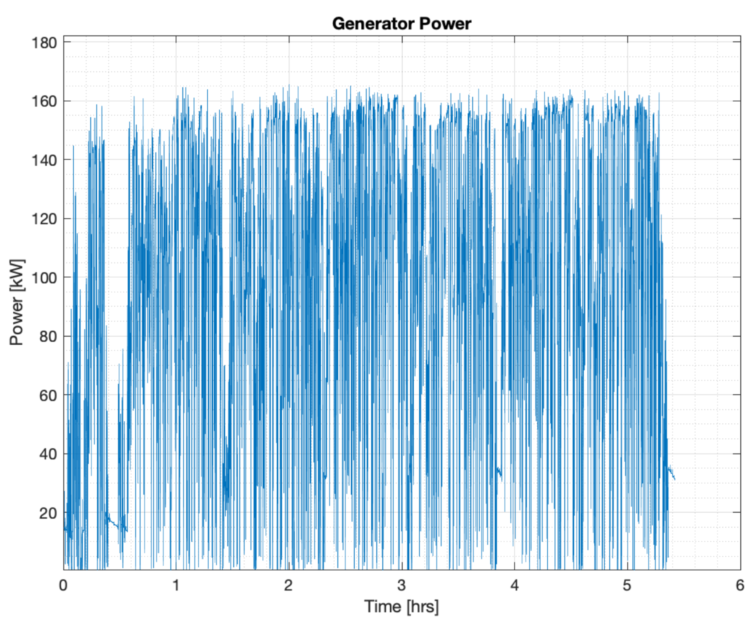

Figure 4.3. Generator power output from Lexington test on 10 October

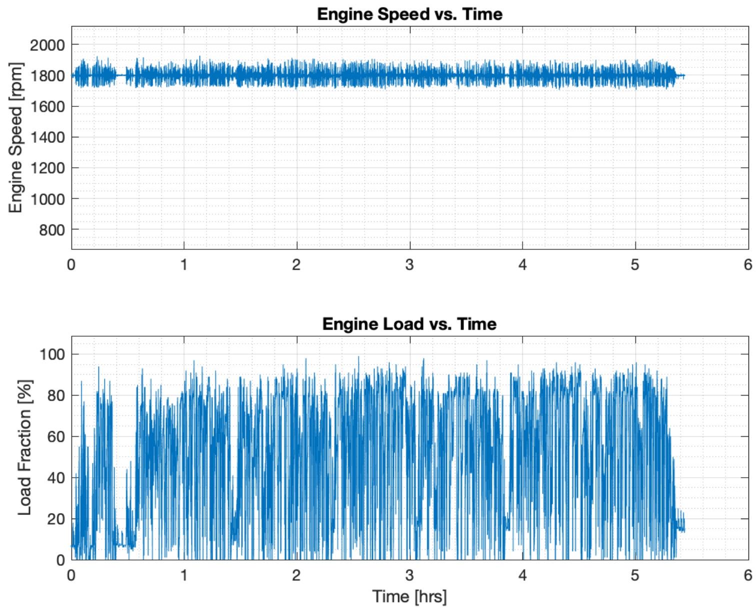

Figure 4.4. Diesel engine rpm and load

The energy supplied by the generator was very consistent with the load conditions throughout testing. The generator's energy accumulation curves for the four primary testing configurations are shown in Figure 4.5, and although on average the energy delivered by the generator increased with load, differences in trip conditions like trailer weight from run to run caused variations of similar magnitude.

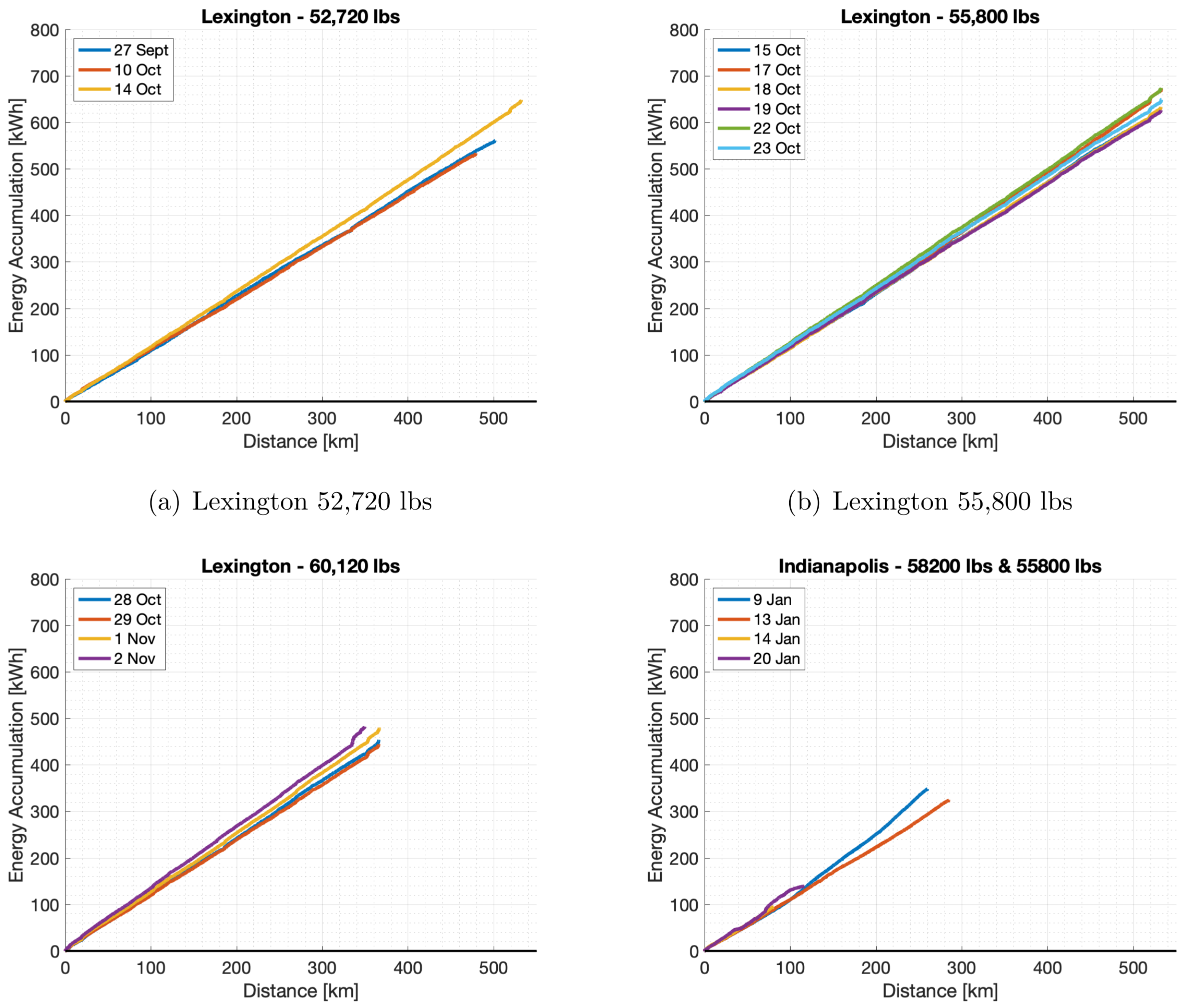

(a) Lexington 52,720 lbs

(b) Lexington 55,800 lbs

(c) Lexington 60,120 lbs

(d) Indianapolis 58,200 & 55800 lbs

Figure 4.5. Generator energy accumulation functions

4.1.2 Motor

The electric motor is the final component of the electric powertrain which provides mechanical power to the wheels. The motor power varied between -200kW to 160kW, as shown in Figure 4.6, indicating huge negative power spikes during deceleration/braking events. The positive 160kW is the maximum rated power of the motor and it reached this limit frequently. Although, the generator saturation power is around 160kW , the motor spent more time at max power compared to the generator indicating battery operation to overcome the deficit.

The negative power spikes during regeneration events were consistent with battery charge events.

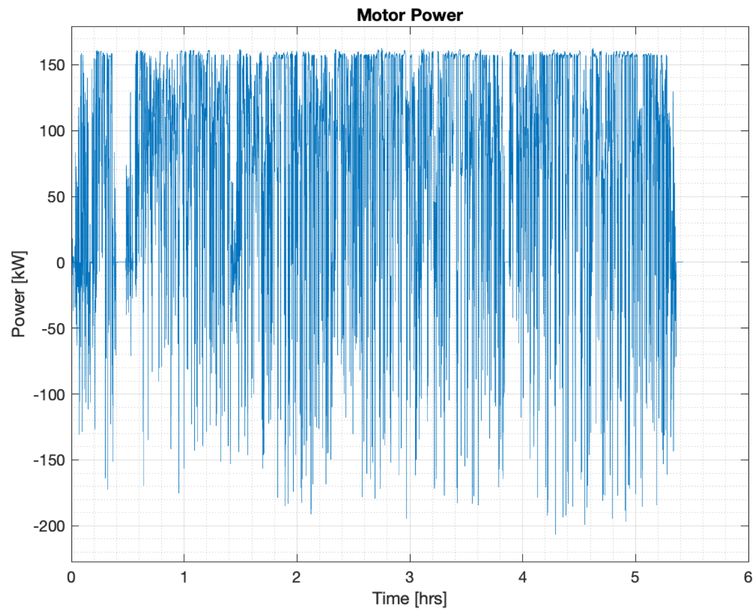

Figure 4.6. Motor power from Lexington from 10 October test run

The main control algorithm deciding the percentage of battery and generator power to be supplied to the motor during propulsion is implemented by the motor controller situated in the power electronics box. To estimate the losses in power electronics , a first law analysis is done. The P_{mot} and $P_{\text{bat}} + P_{\text{gen}}$ are plotted in Figure 4.7 for a 5-km stretch of the Lexington route. The $P_{\text{bat}} + P_{\text{gen}}$ exceeds the P_{mot} during the drive mode by 5% - 15% which is close to the analyzed efficiency of the power electronics. A detailed power electronics efficiency analysis was done by colleague Tyler and is omitted from this thesis.

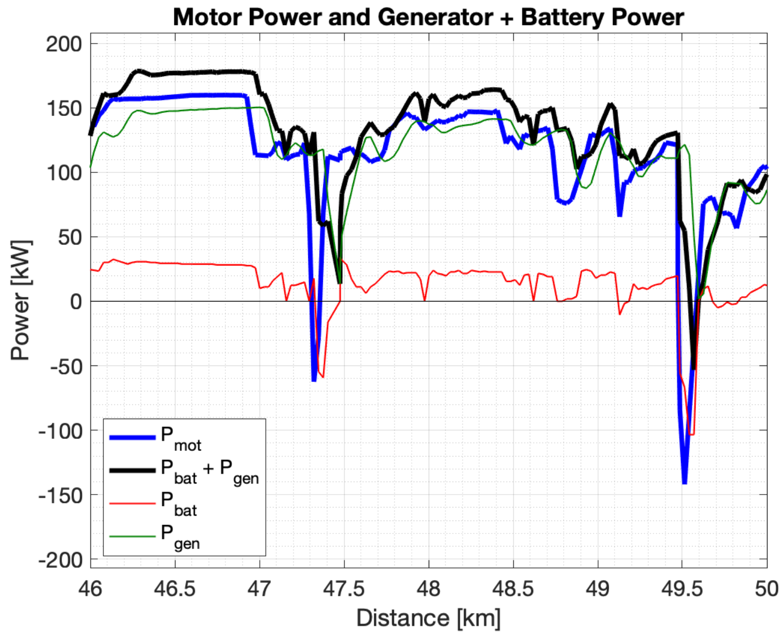

Figure 4.7. $P_{\text{bat}} + P_{\text{gen}}$ from Lexington from 10 October test run

Similar to the generator energy output, the motor energy output is consistent for different conditions as shown in Figure 4.8. The drive and regeneration energy is plotted as a positive solid and negative dotted line respectively. Notably, the regeneration energy in the Indianapolis runs is low compared to the Lexington runs due to flatter road grades and less potential to capture regenerative energy.

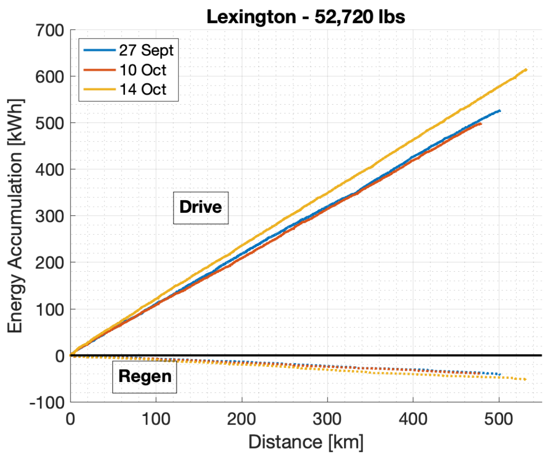

(a) Lexington 52,720 lbs

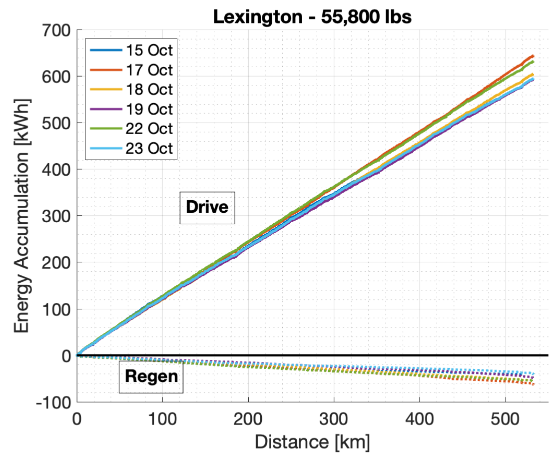

(b) Lexington 55,800 lbs

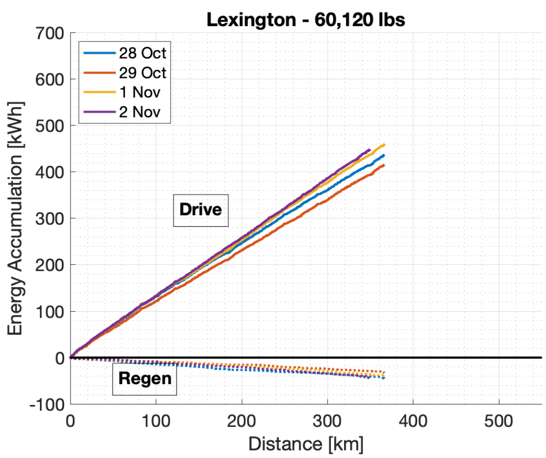

(c) Lexington 60,120 lbs

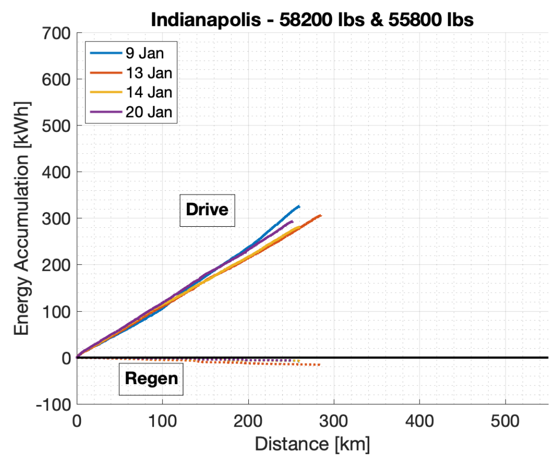

(d) Indianapolis 58,200 & 55800 lbs

Figure 4.8. Motor energy accumulation functions

Th performance of the hybrid powertrain can be analyzed based on its potential to capture the regenerative energy available from the road and be able to utilize to propel the vehicle. The motor energy results show the fraction of regenerative energy to the drive energy was very low. This encouraged a need to model the vehicle system to investigate potentials to increase its regenerative capture and are discussed in detail in Chapter 5.

4.1.3 Battery

The battery acted primarily as the storage device, storing energy from the motor during regeneration and drive energy from the generator during idle conditions. This stored energy was then later supplied to the motor as drive energy aiding the generator electrical energy. The data recorded from the BMS is plotted in Figure 4.9. It shows that the battery state of charge (SOC) is close to 100% throughout the run. The battery current sees huge spikes in both charge and discharge events. The battery voltage remained reasonably constant at 480V.

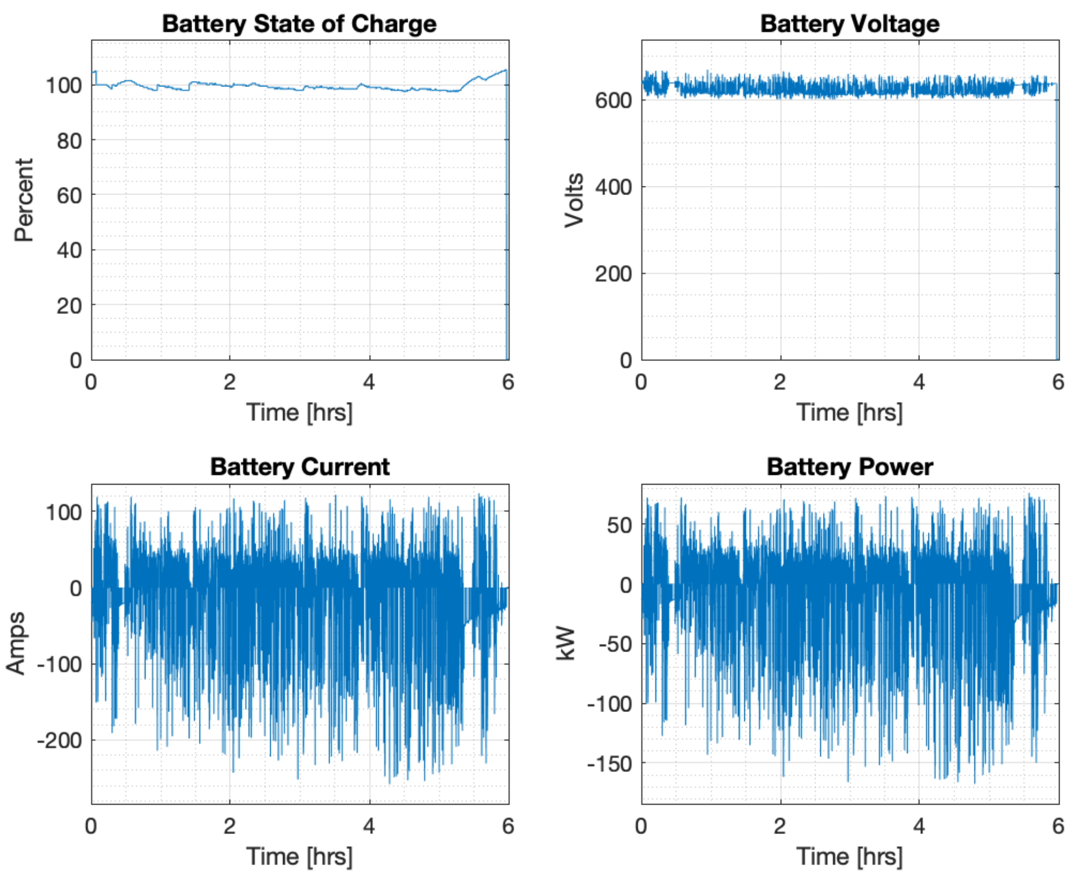

Figure 4.9. Battery power, current, voltage, and state of charge from 10 October test run

From this data, useful information about the battery degradation was inferred.

(i) The voltage of 640 V is lower than the battery packs nominal voltage of 750

(ii) The battery SOC remained at 100% although random measurements of actual cell voltages showed a drop in voltage.

This indicated that some of the battery modules connected in series were not working. This analysis helped identify the faulty battery modules and replace it for the next prototype truck.

Similar to the generator and motor energy accumulation, battery energy accumulation plots were plotted along with an additional net energy of the battery as shown in Figure 4.10. The positive energy indicates battery discharge and negative indicates battery charge.

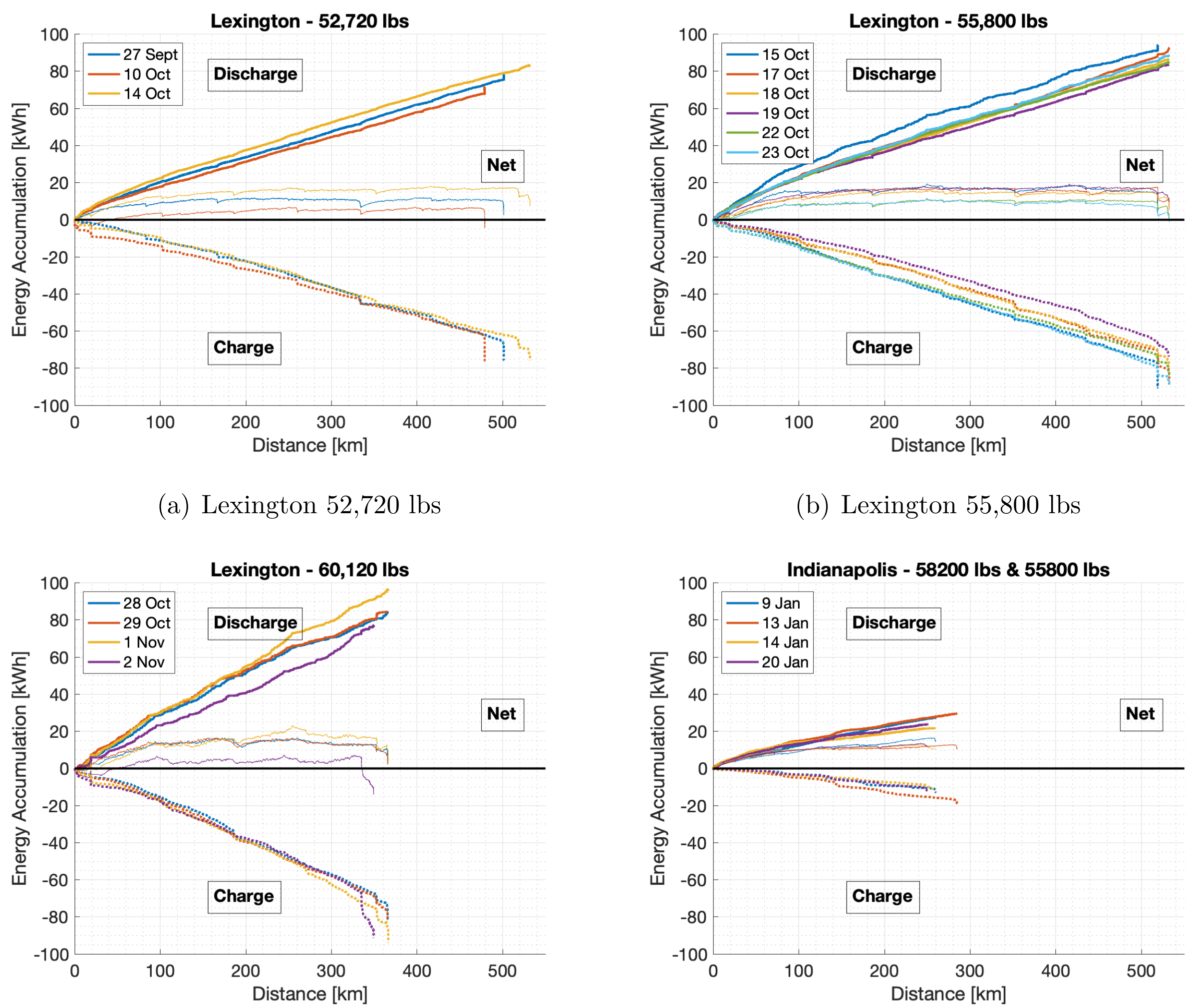

(a) Lexington 52,720 lbs

(b) Lexington 55,800 lbs

(c) Lexington 60,120 lbs

(d) Indianapolis 58,200 & 55800 lbs

Figure 4.10. Battery energy accumulation functions

As shown in above figure, the net energy output was positive between to 20kW indicating net work done by the battery. However, the battery contribution is the main contributor to energy savings in a hybrid architecture and the data indicated that battery energy could be utilized more to potentially increase fuel savings.

4.2 Component Contribution to Work Performed

Plotting all components' energy accumulation curves for a single test run highlights the relative contributions of each component to the total work required to move the vehicle through its drive cycle. These curves are shown in Figure 4.11 for the October 10th test run on the Lexington route with a 52,720 lb payload and are representative of the trends noted throughout the data sets.

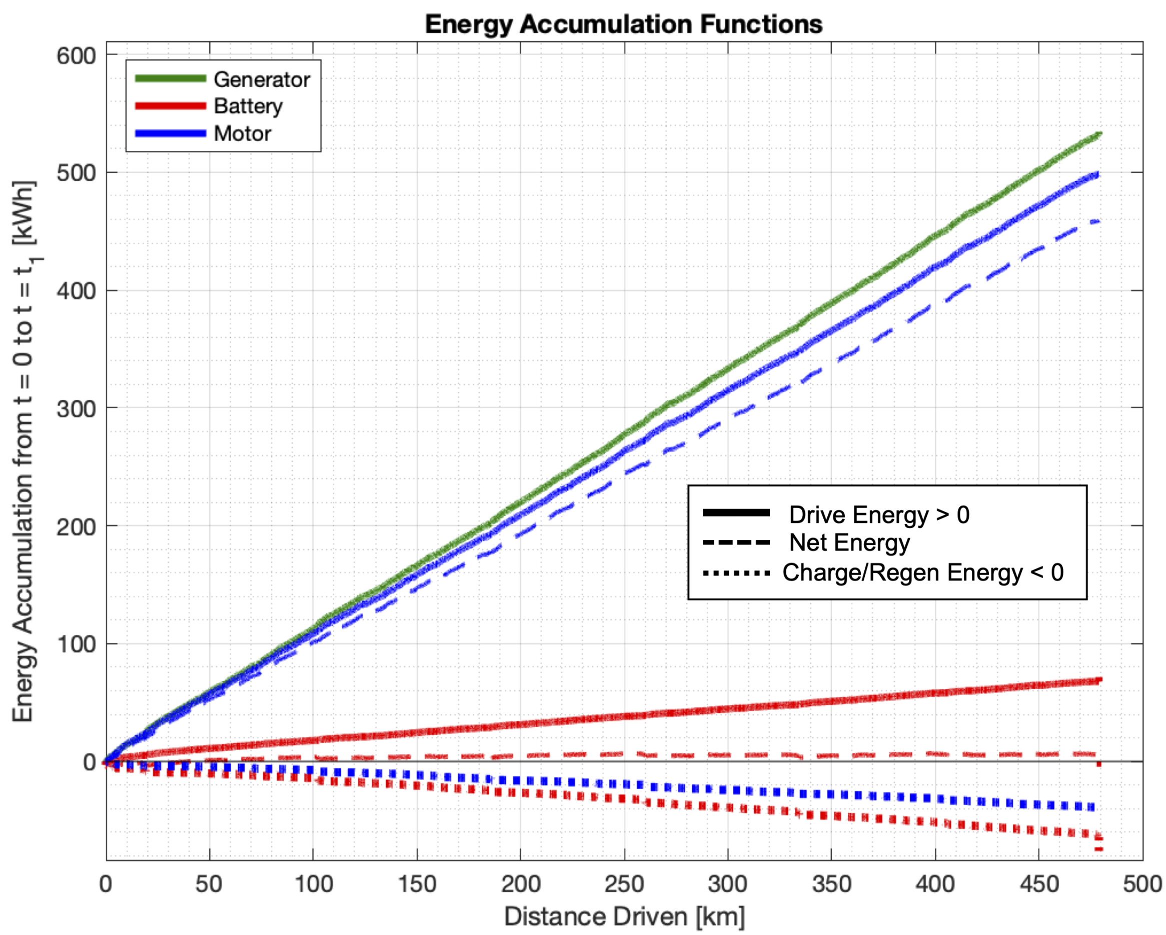

Figure 4.11. Component energy accumulation curves for 10 October test run

As shown in Figure 4.11, the battery charge energy ($E_{\text{bat,charge}} < 0$, red dotted curve) exceeds the motor regeneration energy ($E_{\text{mot,regen}} < 0$, blue dotted curve). This indicates that the generator supplied the remaining charge energy to the battery, but this only occurs at low speed, not during highway cruise. Once the truck slows to turn around, and the motor stops producing regeneration energy, the generator supplies energy to both the battery and the motor during the brief period of low speed operation, accounting for the difference between motor regeneration energy and battery charge energy.

As shown in Figure 2.2, when energy flows from the generator through the battery to the motor, losses are incurred in the battery and both times power is transmitted through the power electronics, a much less efficient path than transfer straight from the generator through the power electronics to the motor. It is also arguably unnecessary to charge the battery from the generator, since the battery's total capacity of 170 kWh is more than double the total discharge energy from the battery in a single test run. As a result, reducing energy flow from the generator to the battery, either through architecture or control changes, may offer a slight increase in overall fuel efficiency.

Additionally, the battery capacity is significantly larger than necessary. It's capacity far exceeds its total discharge energy, and its SOC does not vary significantly throughout a test run. However, because the Tesla battery is optimized for total energy storage, the C-rate must be kept low, and for this application, the large power transfers require a large total capacity to maintain a reasonable C-rate. In future, a chemistry optimized for power delivery instead of total energy storage, such as lithium titanate for example, would allow the battery to be smaller, and a battery without the signs of wear noted in Section 4.1.3 would allow more efficient overall operation.

As a second notable obervation, the total energy provided by the generator ($E_{\text{gen}} > 0$, green) exceeds the motor's total propulsive energy ($E_{\text{gen}} > 0$, blue solid). In an ideal system with no losses, $E_{\text{gen}} = E_{\text{mot,net}}$, which would place the green generator energy line on top of the dashed blue motor net energy line, and regeneration energy would make up the remaining propulsive energy requirement. As a result, any losses in the drivetrain appear as an increase in generator energy output beyond the net propulsive energy requirement.

For this test run, the total generator energy output was 530 kWh, which exceeds the net propulsive energy by roughly 15%, due to losses in the power electronics and battery.

4.2.1 Summary of Test Results

The energy contributions of each component per kilometer are summarized in Figure 4.12 for all available test runs, allowing direct comparison among tests of different distances.

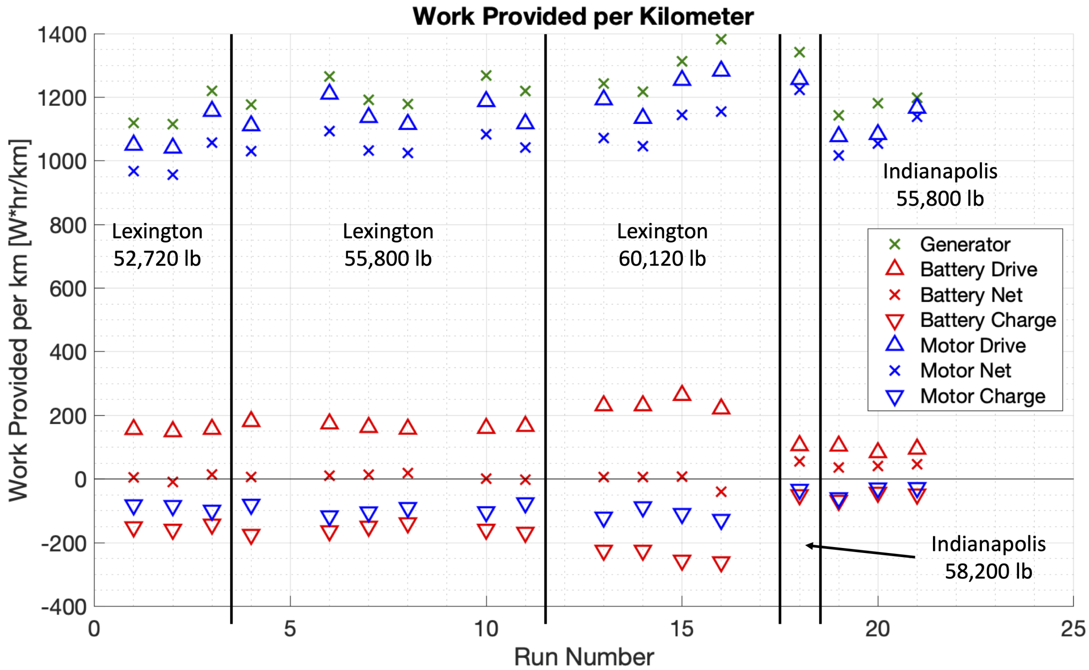

Figure 4.12. Work contributed by each component per km for all data sets

As noted previously, the net energy supplied by the battery is near zero for all runs, and battery charge energy exceeds the regeneration energy supplied by the motor for all runs. Additionally, the motor power and battery charge/discharge energy increases with payload mass, but variation from run to run obscures this trend, indicating that external environmental factors play a significant role in the overall propulsive energy requirement. Finally, the Indianapolis route required significantly less energy flow through all components of the system, particularly the battery, due to its flatness compared to the Lexington route.

5. SYSTEM MODELING

This chapter discusses further analysis of the on-highway testing results by modeling the truck and gaining insights from the ability to capture the regenerative energy. As a first step, the drag and rolling resistance coefficients were determined from experimental coast down tests.

A system model was then developed to estimate the forces on the truck over the course of a drive cycle. This model allowed estimation of the powertrain's theoretical energy requirement and its potential to increase energy savings with decreased drag and rolling resistance.

5.1 Drag and Rolling Resistance Coefficients

In order to estimate the amount of propulsive energy required from the powertrain and regeneration energy available to the powertrain, the truck's drag coefficient, C_d and rolling resistance coefficient, μ must be approximated from coast-down data, where these arresting forces are the only forces acting on the truck. As discussed in Section 3.1.2, two coast-down tests are used to estimate these parameters. Figure 5.1 plots the truck's velocity versus time profiles for each test. At low speeds, the rate of deceleration increased due to unidentified factors, so only the first 50 seconds of data were used for analysis.

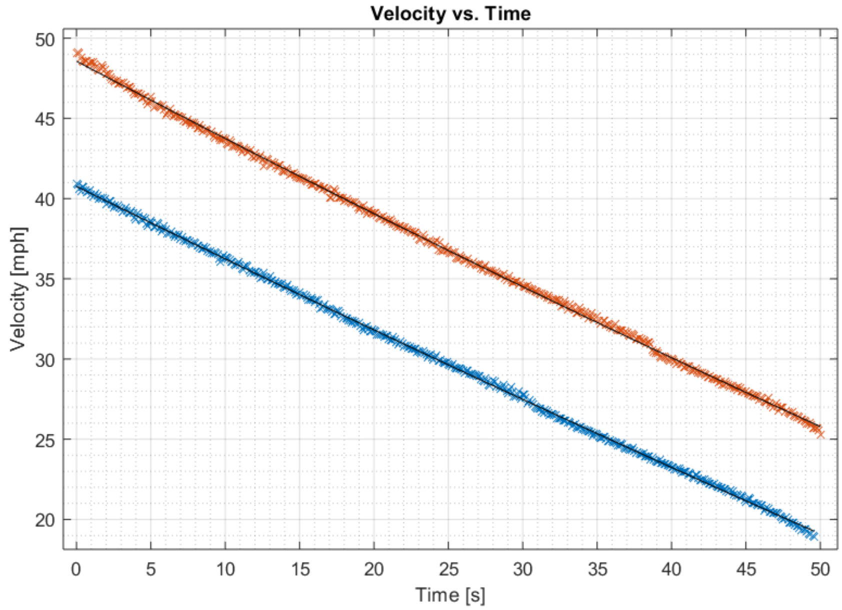

Figure 5.1. Velocity vs. Time Plot from Coast down test on US-42W

C_d and μ can be calculated based on the law of energy conservation represented by Equation 5.1. $W_{\text{resistance}}$ is the work done on the vehicle by drag and rolling resistance forces and will be equal to the vehicle's change in kinetic energy, ΔKE, and potential energy, ΔPE.

$$W_{\text{resistance}} = \Delta \text{KE} + \Delta \text{PE} \tag{5.1}$$

$W_{\text{resistance}}$, ΔKE, and ΔPE can be defined according to Equations 5.2 - 5.4.

$$W_{\text{resistance}} = \int_{t_0}^{t_1} F_{\text{resistance}}(\tau) * v(\tau) d\tau \tag{5.2}$$

$$\Delta \text{KE} = \frac{1}{2} m (v_2^2 - v_1^2) \tag{5.3}$$

$$\Delta \text{PE} = mg(h_2 - h_1) \tag{5.4}$$

Since the road grade angle is negligible and the powertrain is not engaged, the only forces on the vehicle are the aerodynamic and rolling resistance forces, defined in Equation 5.5.

$$F_{\text{resistance}} = F_{\text{aero}} + F_{\text{rr}} = \frac{1}{2}C_d \rho A_f v(t)^2 + \mu m g \tag{5.5}$$

Substituting these expressions into Equation 5.1 yields the equality in Equation 5.6, where C_d and μ are the two unknown parameters.

$$\frac{1}{2}m(v_2^2 - v_1^2) + mg(h_2 - h_1) = \int_{t_1}^{t_2} (\frac{1}{2}C_d \rho A_f v(\tau)^2 + \mu m g) v(\tau) d\tau \tag{5.6}$$

The truck's velocity as a function of time is measured, as are its starting and ending velocity and elevation; the truck's frontal area, A_f, is calculated from the its known dimensions; air density, ρ, is assumed to be a constant 1.225 kg/m^3; and gravitational acceleration, g is a constant 9.8 m/s^2. Using the two data sets over two different speed ranges, two equations can be generated from Equation 5.6 with different numerical values to solve for the two unknown parameters, C_d and μ. Table 5.1 lists the values obtained for these two parameters.

Table 5.1. Drag and Rolling Resistance Coefficients

Parameter	**Value**
C_d	0.68
μ	0.007

These values were validated using a basic model of the nonlinear differential equation (Equation 5.7) representing the truck's dynamics during the coast down test.

$$m\dot{v} = -\mu m g \frac{v}{|v|} - \frac{1}{2}\rho v^2 A_f C_d \tag{5.7}$$

Figure 5.2 plots simulation results and data for the 40 and 50 mph tests, and the the two match fairly closely. These values for C_d and μ are within the expected range for Class 8 trucks, although as discussed in Section 5.2.1, both metrics can be improved.

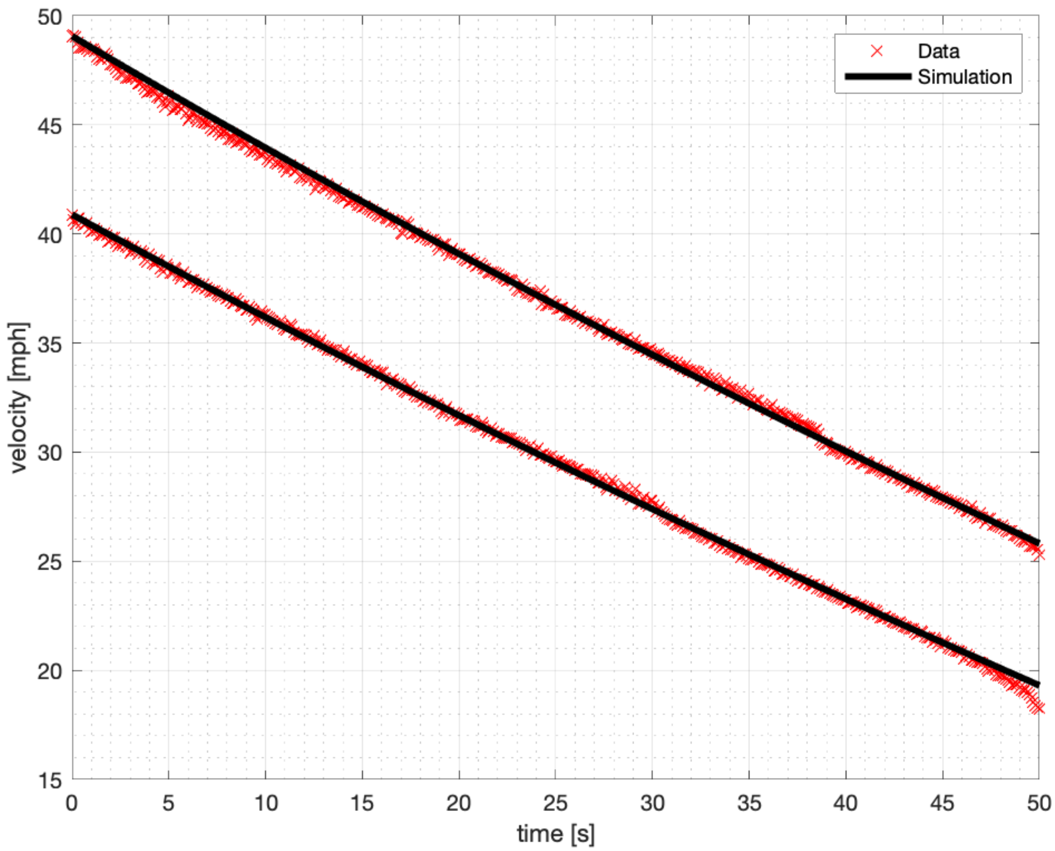

Figure 5.2. Coast-down simulation and measured data

Two factors limit these coefficients' reliability for calculating propulsive and regeneration power. First, in the velocity range tested, the rolling resistance force is much greater than the aerodynamic drag force. As a result, the effects of drag, observable as non-constant deceleration, are almost undetectable. To obtain a better C_d estimate, coast down testing would need to start upwards of 70 mph, a starting speed not possible with the test locations used.

Second, both coefficients vary with tire temperature, road conditions, and relative wind velocity, so these results can only be accurately applied to tests runs that occurred in the same conditions as the coast-down. The values obtained for C_d and μ were close enough for general analysis, but precise calculation of the propulsive energy requirement and regeneration energy available requires more accurate and run-specific coefficients.

5.2 Theoretical Energy Requirement Due to Grade and Speed Changes

The theoretical energy requirement is used to model the truck's energy requirement, and as discussed in Section 5.2.1, this allows the effects of modified system parameters to be estimated.

Calculating Propulsive Power Required

The theoretical energy required to move the vehicle and the theoretical amount of energy available for recapture can be calculated based on the drag coefficient (C_d) and rolling resistance coefficient (μ) estimated in Section 5.1. The forces of interest on the truck are shown in Figure 5.3, yielding the balance of forces in the x-axis, shown in Equation 5.8.

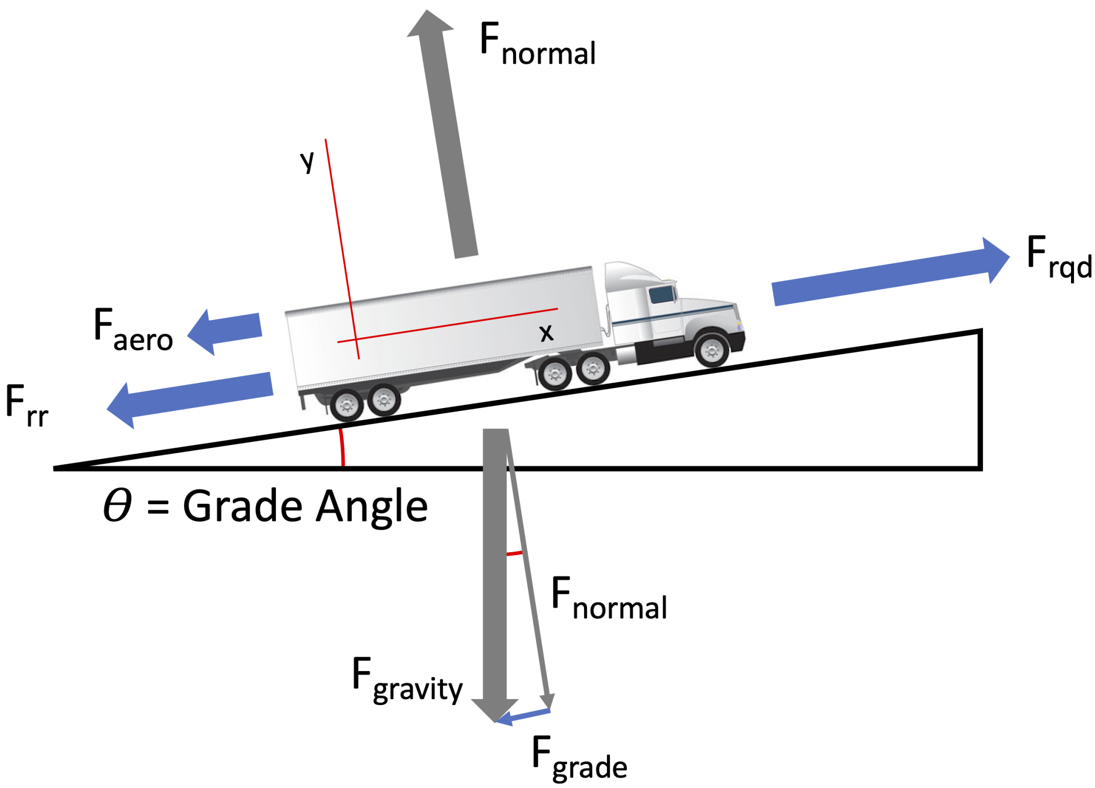

Figure 5.3. Free body diagram for forces on truck during operation

As represented in Equation 5.9, the total force required to accelerate the truck is the sum of grade, aerodynamic and rolling resistance forces, obtained by solving Equation 5.8 for F_{reqd}.

$$\sum F_{\text{x}} = F_{\text{acceleration}} = F_{\text{reqd}} - F_{\text{aero}} - F_{\text{rr}} - F_{\text{grade}} \tag{5.8}$$

$$F_{\text{reqd}} = F_{\text{acceleration}} + F_{\text{grade}} + F_{\text{aero}} + F_{\text{rr}} \tag{5.9}$$

The GPS data allows calculation of each of these forces as shown in Equations 5.10 - 5.13.

$$F_{\text{acceleration}} = ma \tag{5.10}$$

$$F_{\text{grade}} = mg \sin\theta \tag{5.11}$$

$$F_{\text{aero}} = \frac{1}{2}\rho v^2 C_d A_f \tag{5.12}$$

$$F_{\text{rr}} = \mu m g \cos\theta \tag{5.13}$$

The vehicle mass, m, gravitational acceleration, g, atmospheric density, ρ, and the truck's frontal area, A_f are known or measured constants, the truck's velocity, v, acceleration, a, and the route's grade angle, θ are obtained from the GPS data, and the drag coefficient C_d and rolling resistance coefficient, μ are estimated in Section 5.1. Finally, the instantaneous power required is simply the product of the force required to move the truck at that instant and the truck's velocity:

$$P_{\text{reqd}} = F_{\text{reqd}} v \tag{5.14}$$

The four components of the required power calculation are plotted in Figure 5.4 for a 4-km section of the October 10$^{\text{th}}$ test run, and clearly the grade and acceleration components dominate this calculation, with magnitudes near or above the motor's maximum output of roughly 160 kW. In comparison, the rolling resistance and aerodynamic drag require relatively little power to overcome. Unlike acceleration and grade power, they are always positive and relatively constant, so the actual energy required to overcome rolling resistance and drag is of similar magnitude to the acceleration and grade energy requirements.

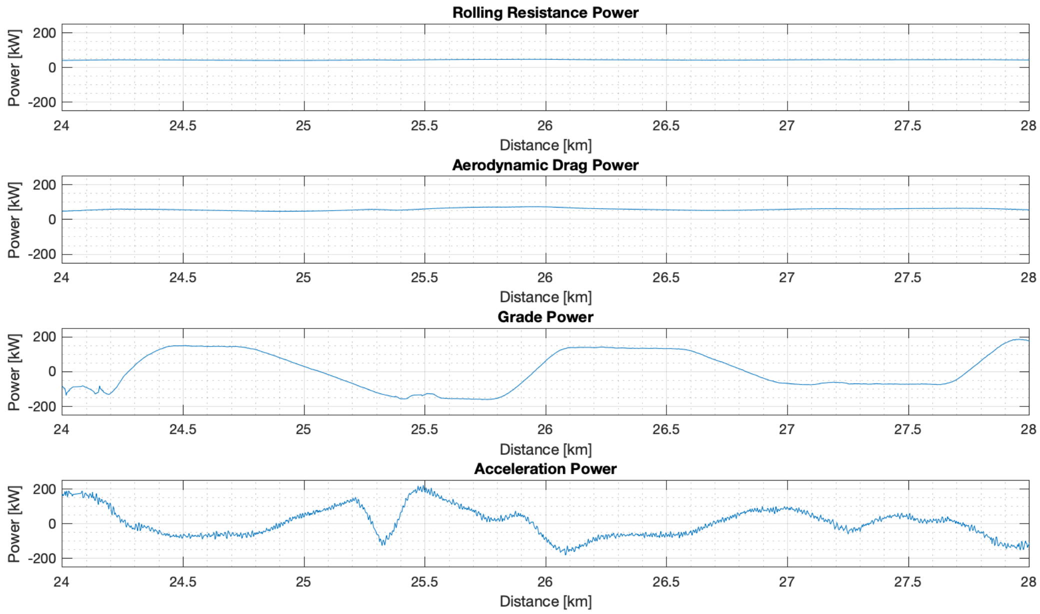

Figure 5.4. Components of calculated power required

Smooth curves were obtained for all of the power components except the acceleration power. The total calculated power required curve and the measured motor power are plotted in Figure 5.5, and although the calculated results track the motor's output reasonably well, the noise from the acceleration data appears in this final calculation.

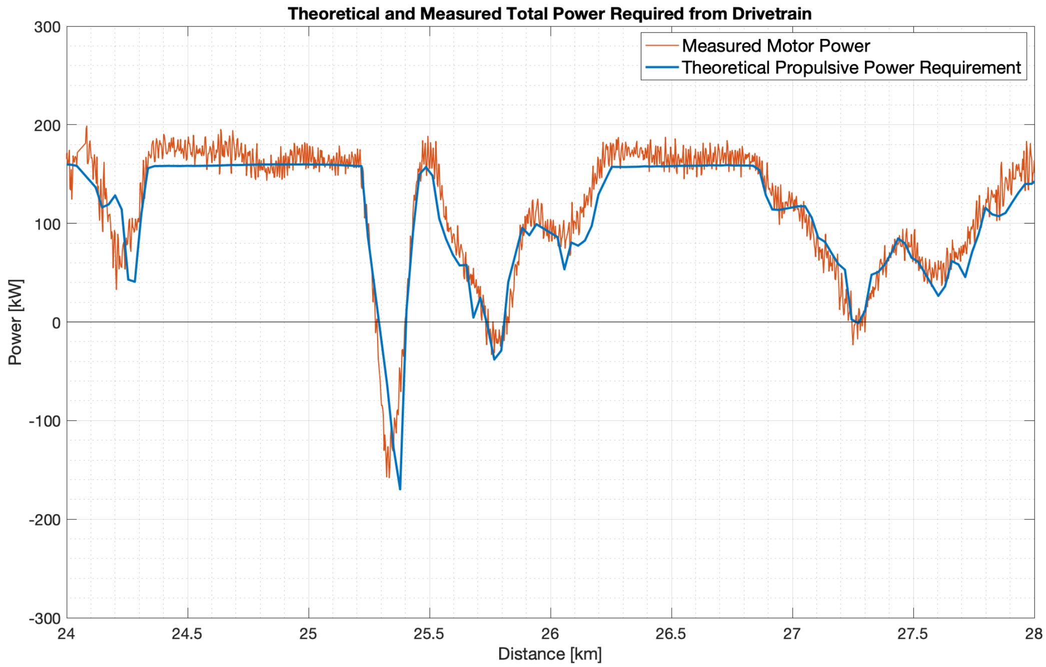

Figure 5.5. Actual and theoretical motor drive power

Theoretical Propulsive Energy Required

The amount of energy theoretically required to move the vehicle can be calculated as the accumulation function (Equation 4.1) of the power required function described by Equations 5.8 - 5.14. As shown in Figure 5.6, the vehicle's the propulsive, regeneration, and net energy as calculated from GPS data matches the values recorded from the motor for the October 22nd test.

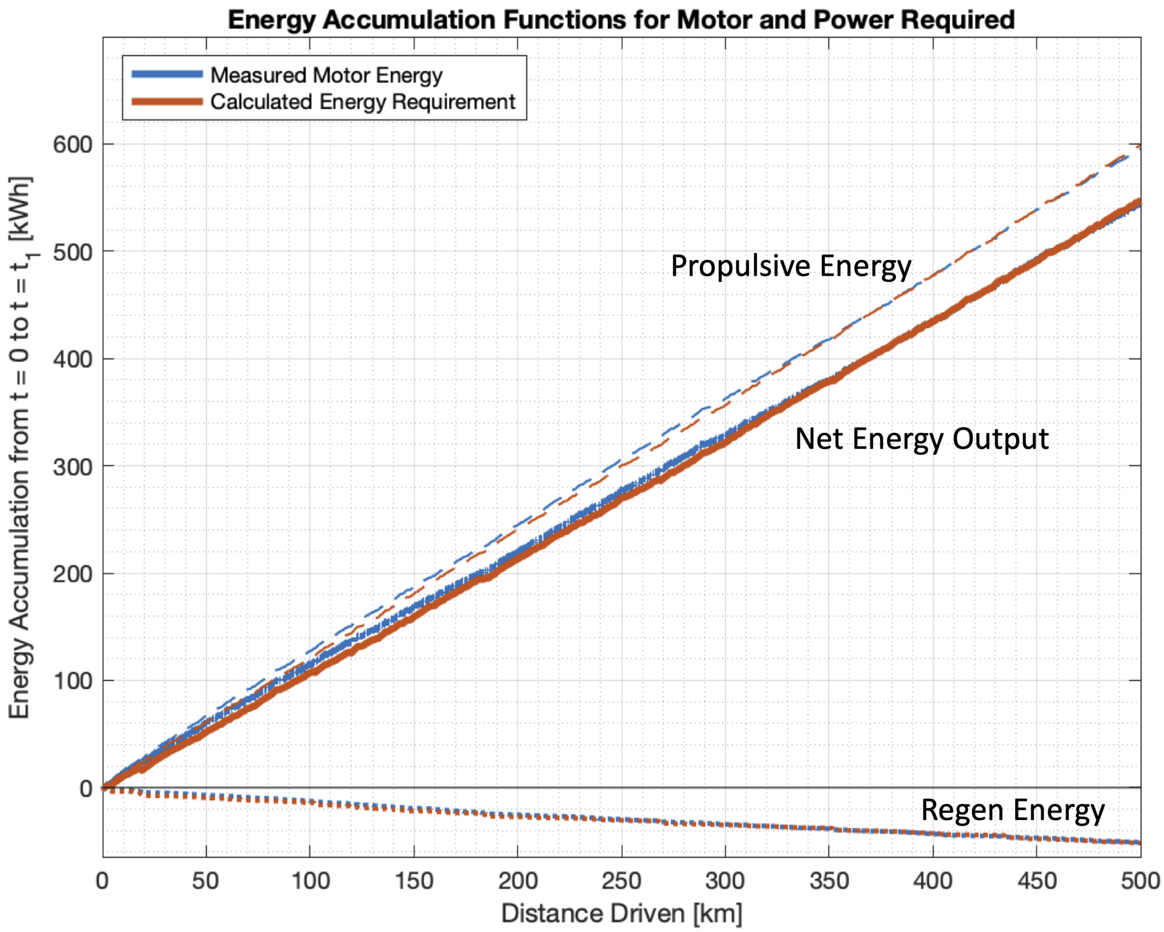

Figure 5.6. Energy accumulation functions for theoretical and motor energy from 22 October test

This power required calculation is sensitive to filtering techniques, small changes in C_d and μ, and relative wind components. The conditions in this particular test closely matched the coast down test conditions, yielding accurate results, but other test runs that occurred in different environmental conditions, such as crosswinds and low and high temperatures yielded significantly different results. For example, 20 mph crosswinds during second half of the January 9$^{\text{th}}$ Indianapolis test caused much higher drag, and as a result, the motor energy output exceeded the theoretical required energy to move the truck, shown in Figure 5.7.

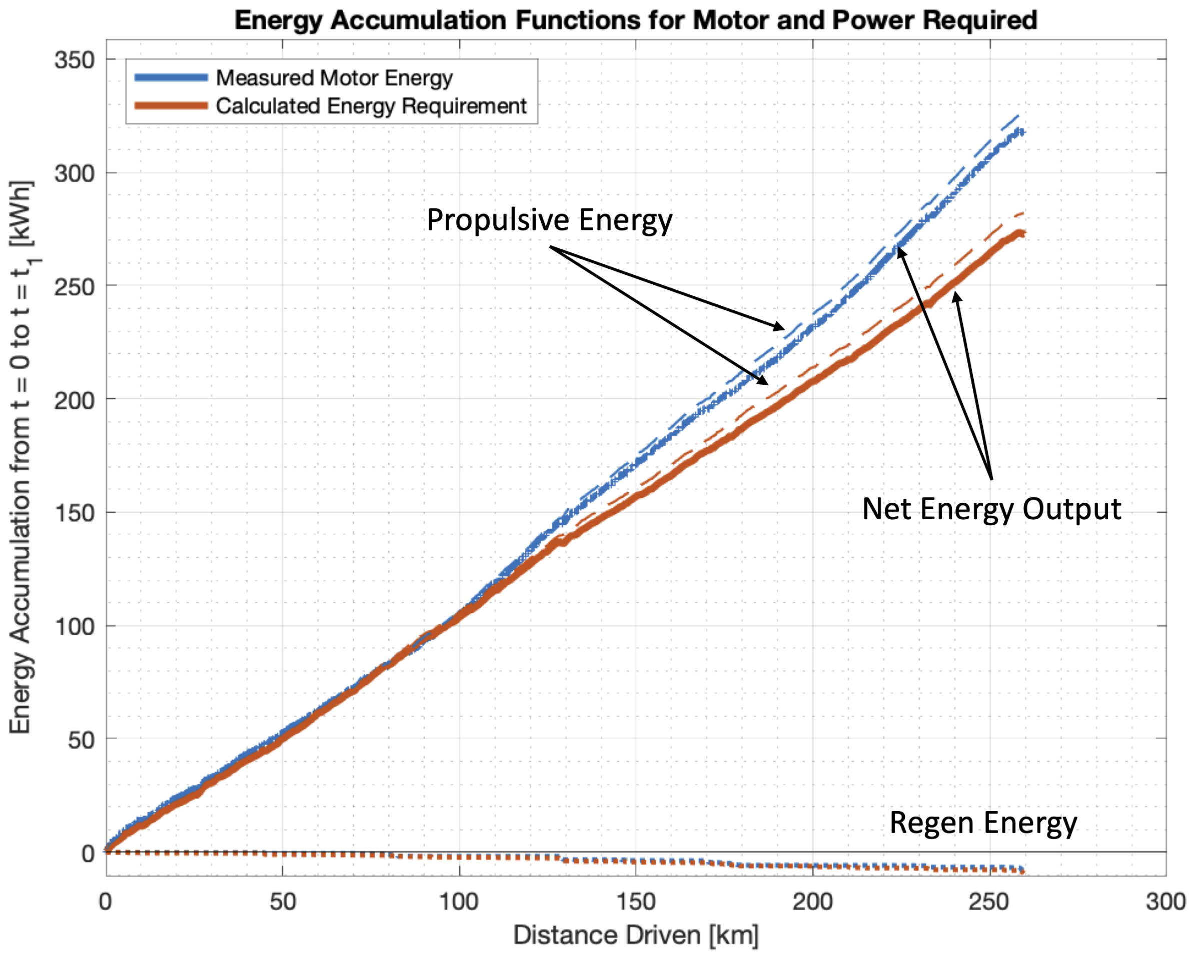

Figure 5.7. Energy accumulation functions for theoretical and motor energy from 9 January test

Theoretical Regeneration Energy Available

The amount of energy theoretically available for regeneration was calculated as an accumulation function (Equation 4.1) of only the negative portions of the power required function described by Equations 5.8 - 5.14. This is plotted as a negative dotted line in Figures 5.6 and 5.7, and the ratio of measured motor regeneration energy to calculated regeneration available is plotted in Figure 5.8 for test runs with usable data.

With the exception of runs 18 and 21, the actual motor regeneration energy was within 20% of the calculated available regeneration energy. Run 18 is the January 9th Indianapolis test run which occurred in high winds, and run 21 occurred in particularly low temperatures, which increase air density and rolling resistance, reducing the actual amount of regeneration energy available. Additionally the actual regeneration energy captured by the motor exceeded the calculated regeneration energy available in half of the test runs, which is due to the use of fixed C_d and μ values for all operating conditions. The problems with this assumption are discussed in Section 5.1.

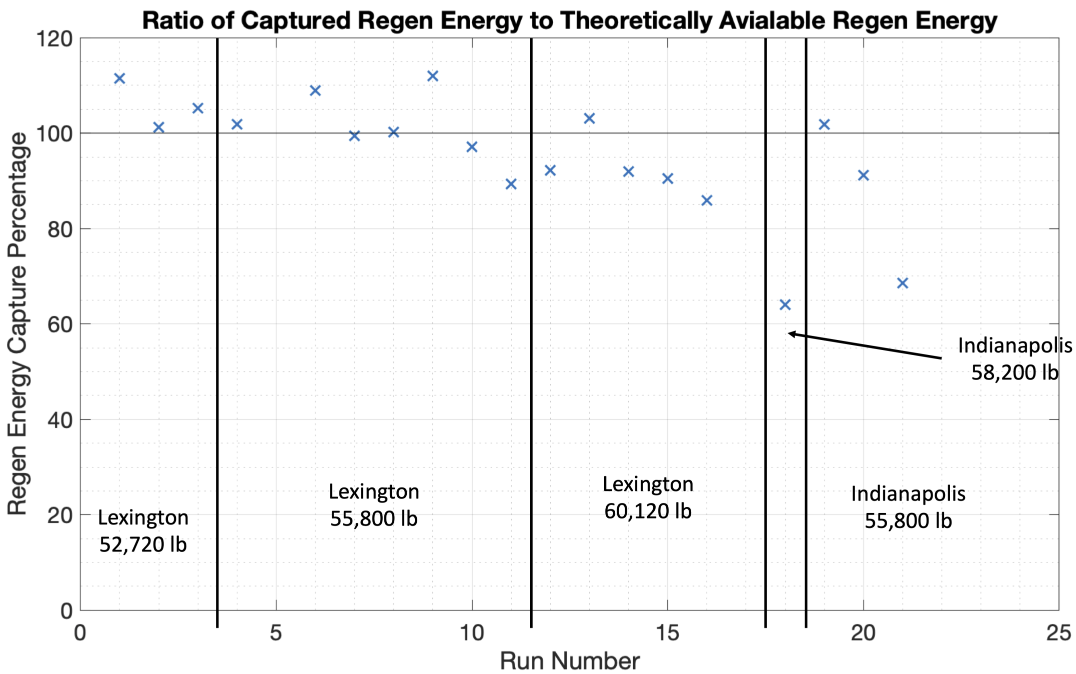

Figure 5.8. Measured motor regeneration energy as fraction of calculated available energy

This ratio of measured regeneration energy to calculated available regeneration energy is evenly distributed around 100%, indicating that the prototype truck system captures close to 100% of the available regeneration energy. However, since the C_d and μ values used were not run-specific, and since relative wind was not taken into account in the theoretical energy model, specific conclusions cannot be drawn on a run-by-run basis for the amount of available regeneration energy the prototype drivetrain was able to capture.

5.2.1 Ratio of Regeneration Energy Capture to Drive Energy Output

The ratio of regeneration energy captured (E_{regen}) to drive energy output (E_{drive}) provides a straightforward comparison between routes and shows the series hybrid's advantages and potential room for improvement. Variations in ambient temperature, road surface, and relative wind were not considered, so per Equations 5.9 - 5.14, these energies depend only on acceleration, speed, and grade angle. For each test route and mass, this ratio of drive to regenerative energy was calculated according to Equation 5.15 as a function of C_d and μ, where each energy term is calculated from its respective force term as shown in Equation 5.16.

$$\frac{E_{\text{regen}}}{E_{\text{drive}}} = \frac{E_{\text{decel}} + E_{\text{grade,down}}}{E_{\text{accel}} + E_{\text{grade,up}} + E_{\text{rr}} + E_{\text{aero}}} \tag{5.15}$$

$$E = \int_{t_1}^{t_2} P(\tau)d\tau = \int_{t_1}^{t_2} F(\tau)v(\tau)d\tau \tag{5.16}$$

This energy ratio is plotted as a color shade ranging from blue to yellow in terms of C_d and μ in Figures 5.9 - 5.13. Each plot is based on a measured speed and acceleration profile at the given mass, and does not account for any changes in this profile that may occur due to changes in C_d or μ. A comparison is made with a new low-mileage Peterbilt 579 truck. The C_d, μ values for the new truck were taken from reference study [13]. The two (C_d, μ) points marked on each plot correspond to the coefficients for the prototype truck, estimated in Section 5.1, and for a new, low-mileage Peterbilt 579. This comparison is done to understand the prototype truck's energy utilization potential.

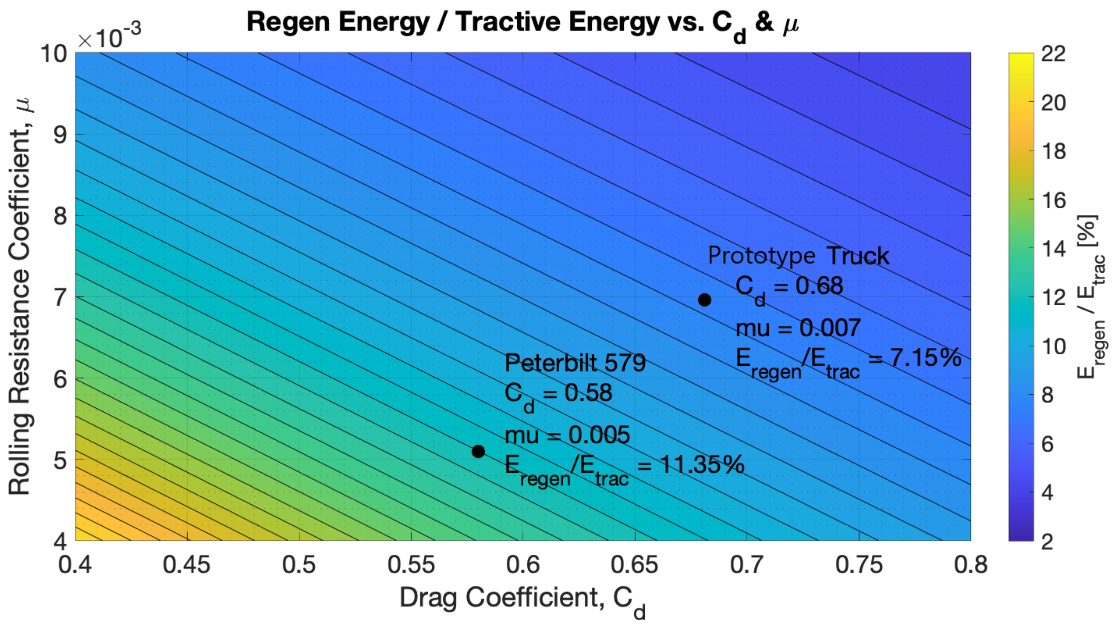

Figure 5.9. Energy ratios for Lexington test, 10 October, 52,720 lbs

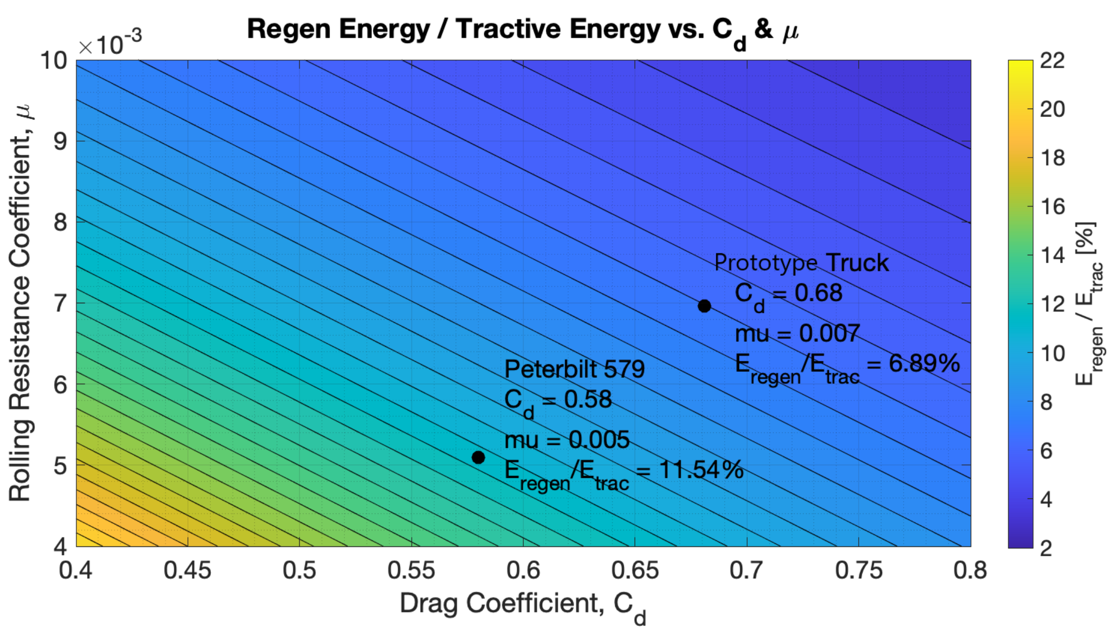

Figure 5.10. Energy ratios for Lexington test, 15 October, 55,800 lbs

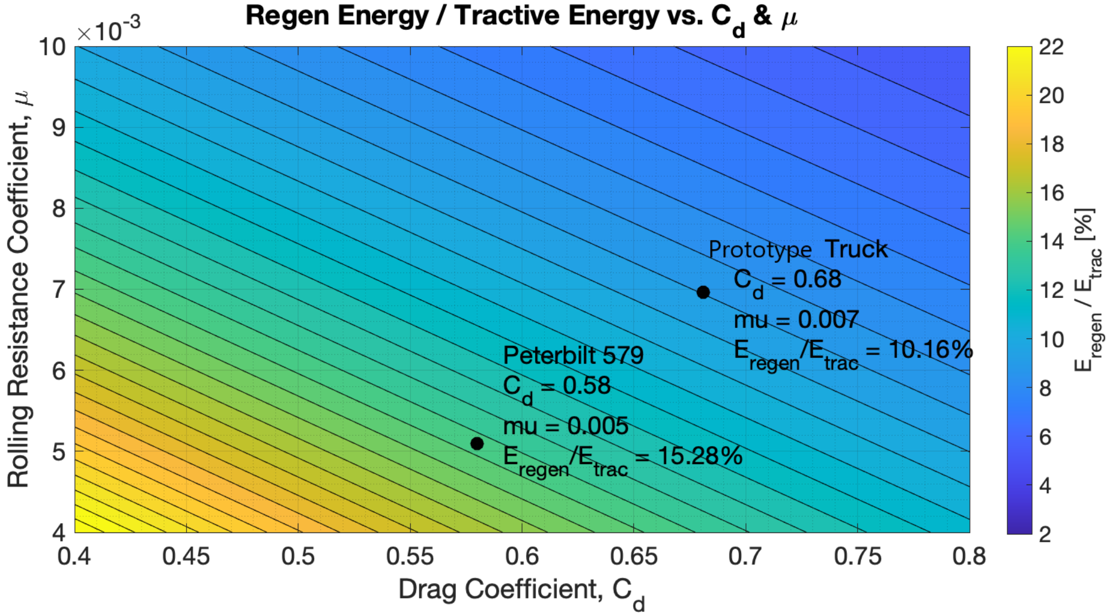

Figure 5.11. Energy ratios for Lexington test, 1 November, 60,120 lbs

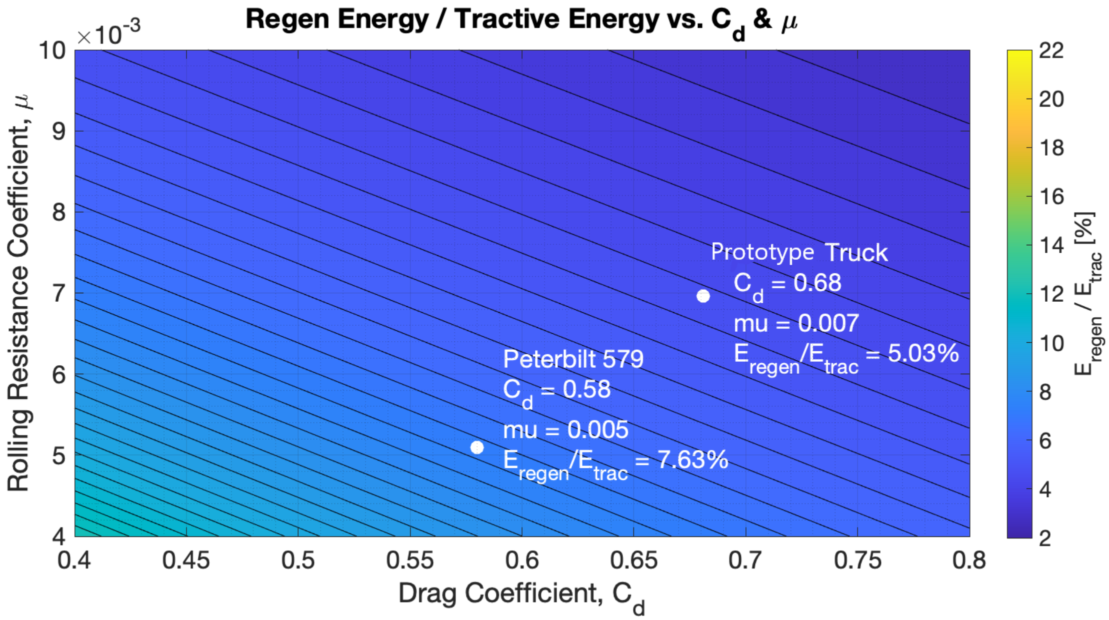

Figure 5.12. Energy ratios for Indianapolis test, 9 January, 58,200 lbs

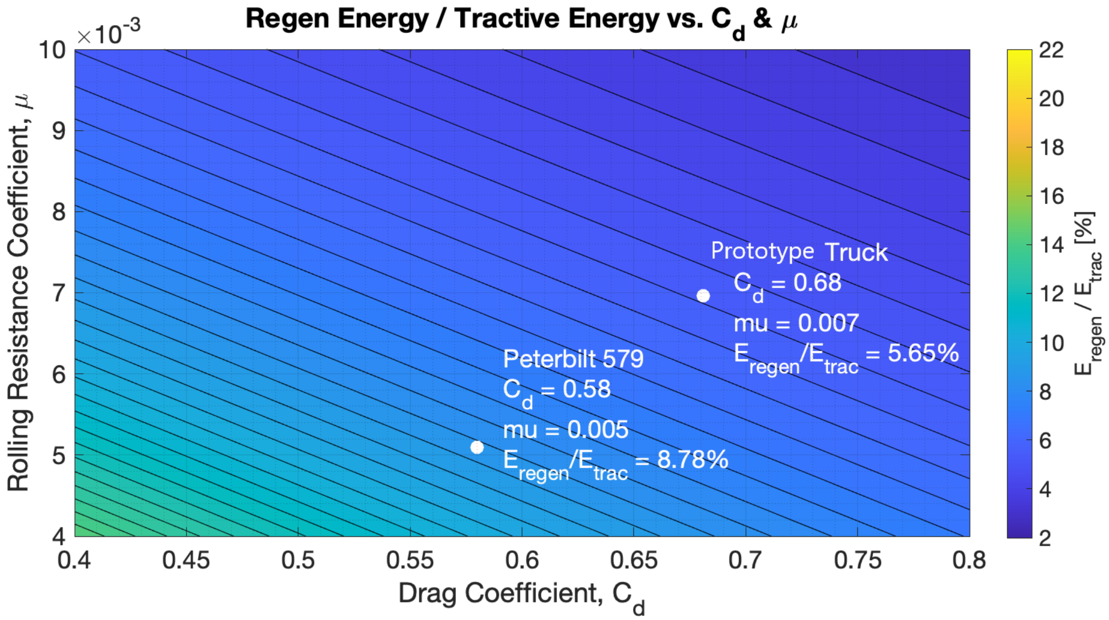

Figure 5.13. Energy ratios for Indianapolis test, 13 January, 55,800 lbs

As expected, based on the higher battery energy transfer (Section 4.1.3), the ratio of regeneration to drive energies for the Lexington route is almost double the ratio for the Indianapolis route, due to the Lexington route's rolling hills. This again affirms that grade profile along the truck's route directly determines the drivetrain's opportunity to capture and reuse regenerative braking energy.

Additionally, decreasing the truck's aerodynamic and rolling drag can potentially improve this energy recapture ratio. In a conventional drivetrain without electrification, reducing a truck's drag reduces the amount of propulsive energy required. However, with the prototype system, the benefits are twofold. Lower resistance both reduces the propulsive energy requirement to move the vehicle, and frees more kinetic energy to be captured through regeneration. The Peterbilt 579 truck and trailer used for comparison incorporate modern aerodynamic improvements and generate less rolling resistance due to lower wear, and these improvements could increase the energy recapture ratio to 8% - 18%, depending on the route, as shown in Figures 5.9 - 5.13.

Finally in Figure 5.14, three energy ratios are plotted for each test run: (1) the prototype truck energy ratio as calculated from motor power data, (2) the prototype energy ratio as calculated from its theoretical power requirement, and (3) the reference 2018 Peterbilt 579 energy ratio as calculated from its power requirement.

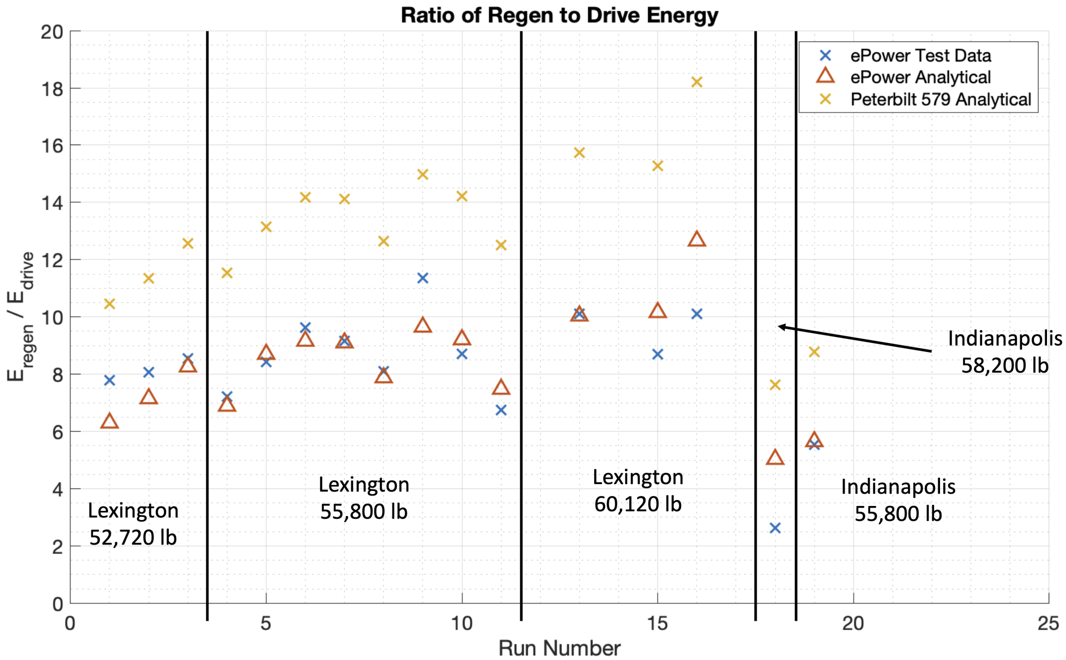

Figure 5.14. Energy ratio results summary

Despite the uncertainty of the C_d and μ coefficients, the analytical results closely track the test results for the ePower truck, so the extrapolation of the energy calculation to different rolling resistance or drag coefficients is reasonable.

Additionally, there is a slight increase in energy ratio with payload mass, which indicates a slight increase in overall performance with mass. This is because the aerodynamic drag term in the denominator of Equation 5.15 is independent of mass, whereas all other terms depend on mass. As a result, when mass increases, the percent increase of regeneration energy is slightly greater than the percent increase of drive energy. However overall, drag and rolling resistance improvements offer the most significant benefits to the series hybrid system's overall performance.

6. CYLINDER DEACTIVATION SIMULATION RESULTS

This chapter discusses the simulated cylinder deactivation efficiency improvement results in comparison to the simulated baseline results for the natural gas engine. A supporting analysis is done to understand the engine operation as well as limitations while implementing CDA.

6.1 CDA Introduction

The performance limitations of an S.I engine are discussed in Chapter 1.3.2.The part load pumping losses caused by the operation of throttling valve are seen in the low load - low speed region of the torque curve. Since the power requirement at this regions are low, the engine is capable to be operated by reducing the number of firing cylinders. The strategy to operate the engine by deactivating cylinders is called cylinder deactivation (CDA). This work focuses on tackling the part load throttling losses by CDA. Experimentally, this is done by deactivating the cylinder valve motions using the VVA system discussed in section 2.3).

6.1.1 Nomenclature

Based on the number of deactivated cylinders the CDA strategies are named as follows :

- 2CDA - Cylinders 1,6 deactivated
- 3CDA - Cylinders 1,2,3 deactivated
- 4CDA - Cylinders 2,3,4,5 deactivated

Figure 6.1 illustrates the CDA operation used in the analysis. A notable observation in the 3CDA illustration, is the deactivation of cylinders 1,2,3. The EGR loop intakes exhuast gases from cylinders 4,5 and 6 due to the split exhaust manifold. Deactivating cylinders 4,5 and 6 would be difficult to operate to meet EGR demands and may cause instability in the EGR controller. Hence, for 3 CDA operation, cylinders 1,2,3 are deactivated.

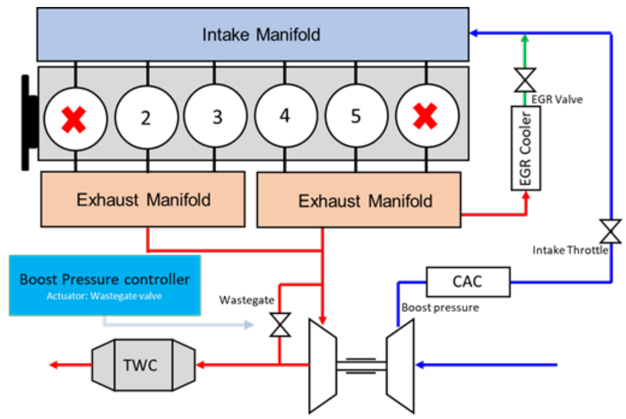

(a) 2 CDA

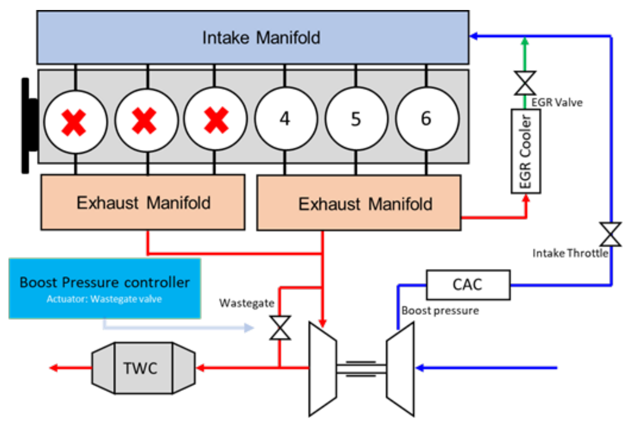

(b) 3 CDA

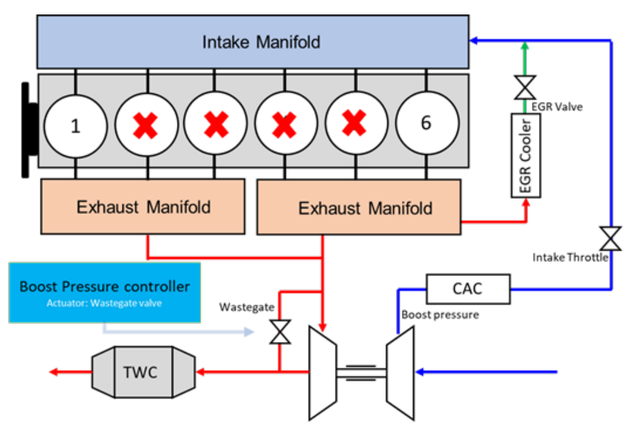

(c) 4 CDA

Figure 6.1. CDA Operation

6.2 CDA Efficiency Results

The assumptions and limitations of the Simulation model, briefly discussed in section 3.2.3, should be referred while inferring from the simulation results.

The engine cycle efficiency analysis discussed in section 3.2.5 was followed to calculate the overall BTE and fuel benefits. A comparison is done with the 6 Cylinder firing engine operation labeled as *Baseline* in the plots. CDA is most effective in low torque regions and has its limitations at higher loads depending on the number of cylinders deactivated. The limitations are discussed in detail in 6.2.2.

6.2.1 Fuel Benefits

Significant improvements were seen in fuel savings and overall brake thermal efficiency of the engine. The simulation results in Figure 6.2 show a maximum reduction in fuel flow of 11% for 2CDA, 18% for 3CDA and 25% percent for 4CDA in comparison to the Baseline simulation results. Corresponding BTE improvements are seen in Figure 6.3 with a maximum increase of 2%, 3% and 4% for 2CDA, 3CDA and 4CDA compared with the baseline respectively.

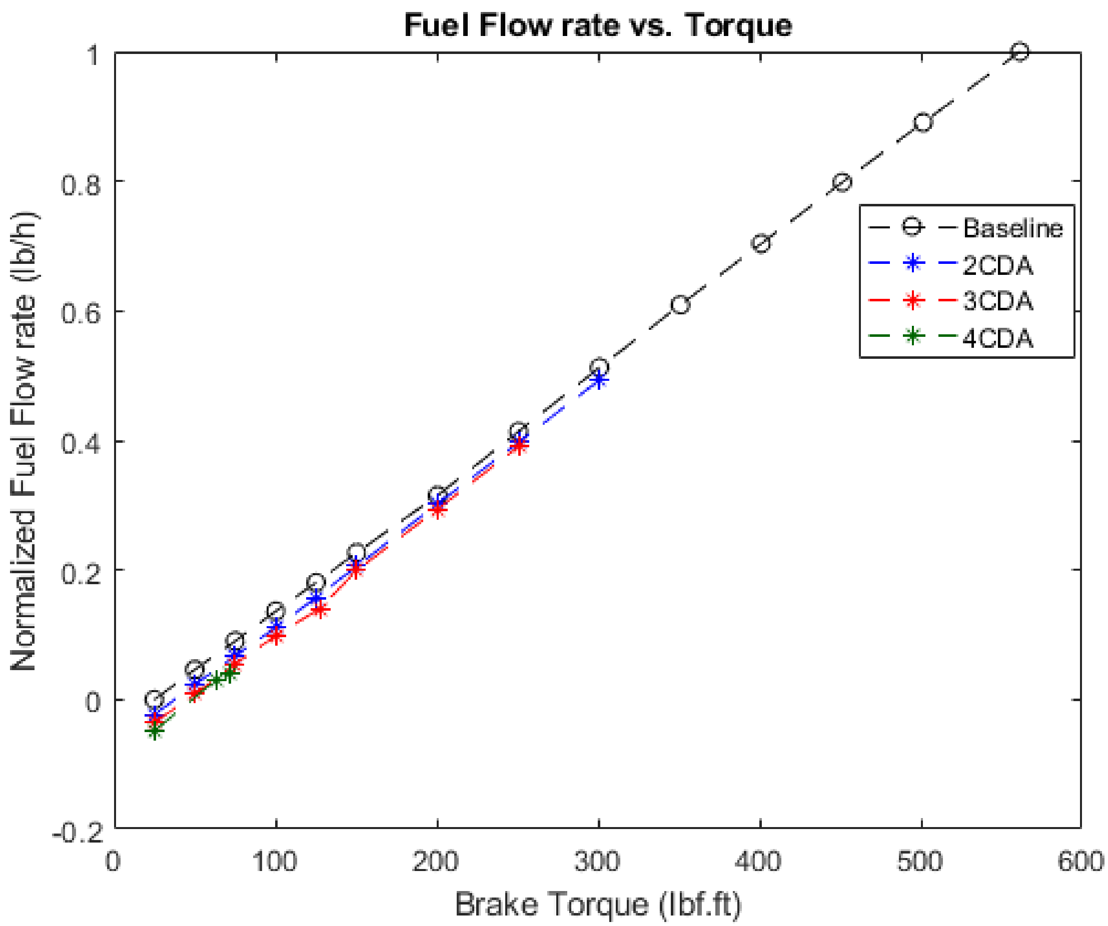

Figure 6.2. Fuel Flow Rate (Simulation)

Reduced fuel flow rate results in improved fuel consumption. BSFC is a measure of efficiency with respect to the engine power output. BSFC can be claculated as

$$BSFC = \frac{P_{brake}}{\dot{m}} \tag{6.1}$$

where P_{rake} is brake power and $\dot{m}$ is fuel mass flow rate.

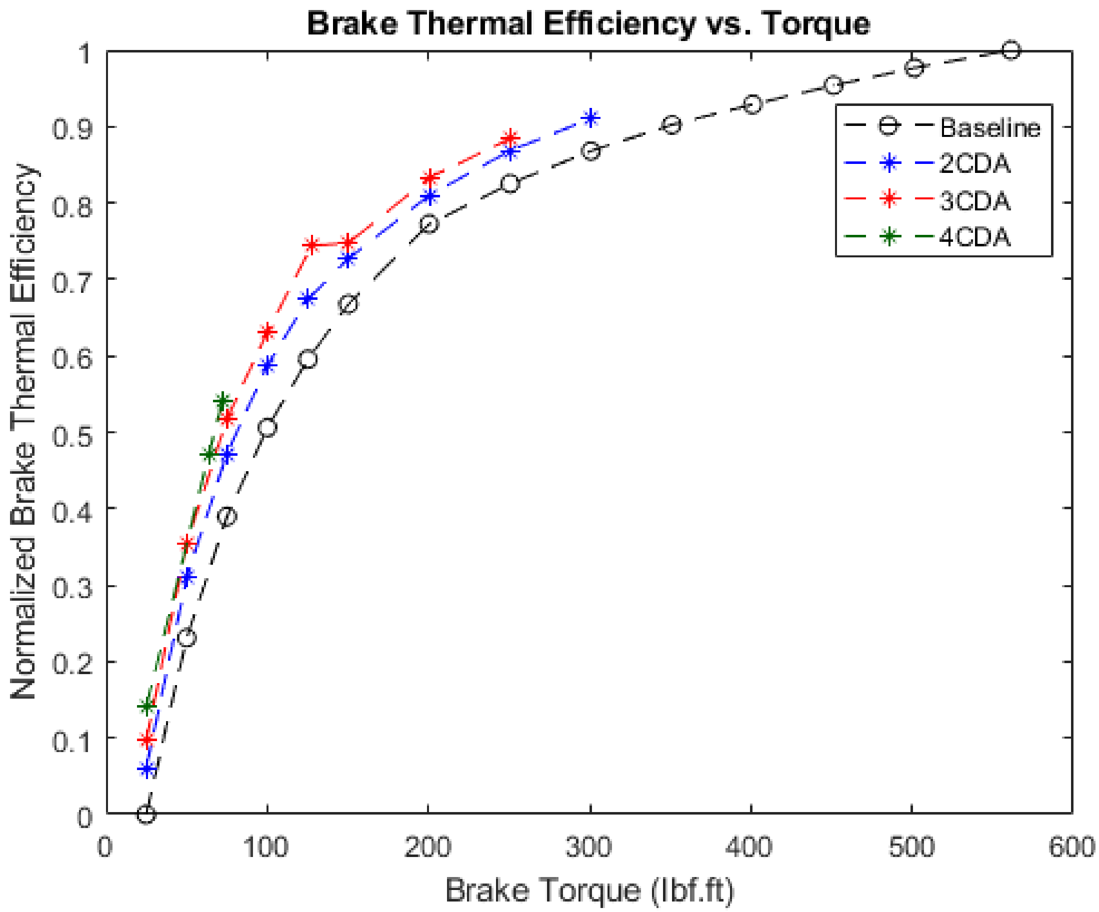

Figure 6.3. Brake Thermal Efficiency (Simulation)

BSFC is inversely proportional to the BTE as can be seen from Figure 6.4. A notable observation from Figures 6.2- 6.4 is maximum benefits are seen at lowest torques. BSFC percent decrease with respect to *Baseline* is shown in Figure 6.5. The percentage reduction with respect to baseline is higher at low torques and reduces with increase in torque. The pumping/throttling losses are maximum at low loads, hence maximum BSFC reduction seen at low torques indicates overcoming of these losses. Engine cycle efficiencies are further assessed to determine contributors to the overall efficiency improvement.

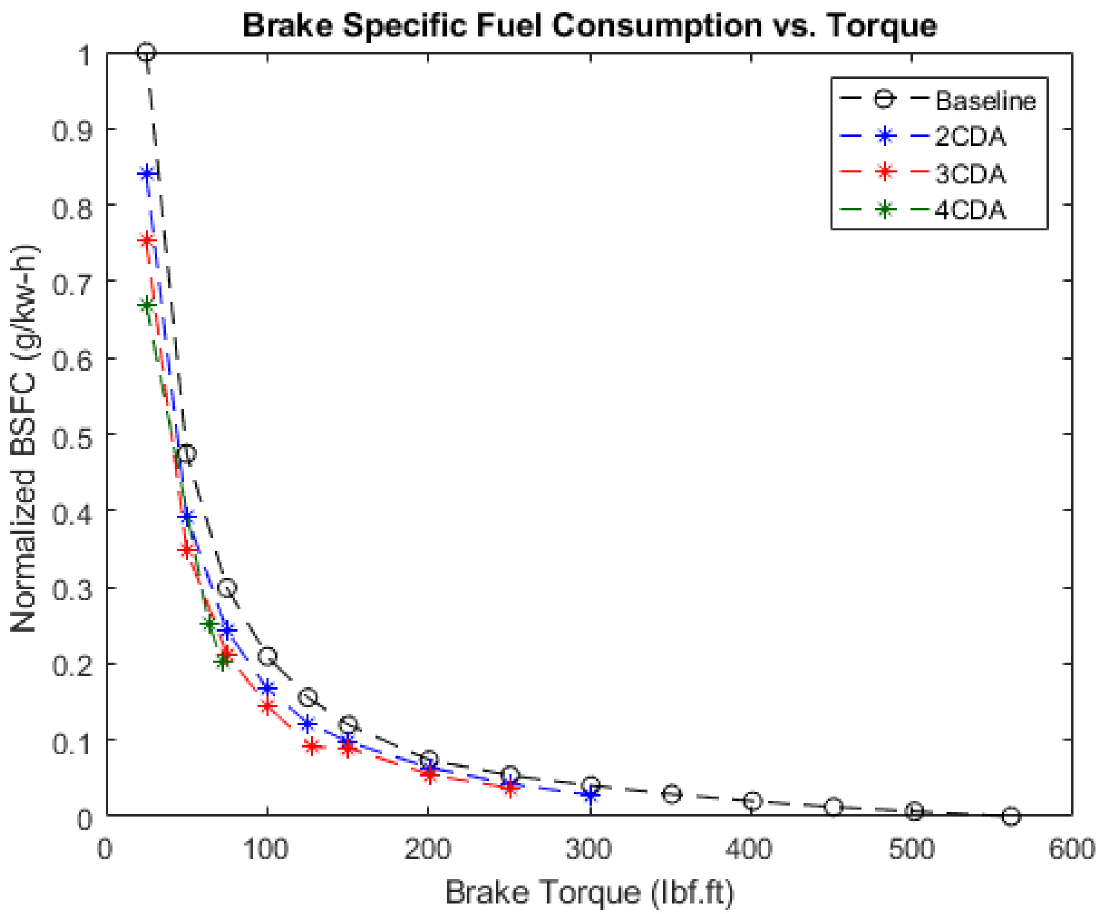

Figure 6.4. Brake Specific Fuel Consumption (Simulation)

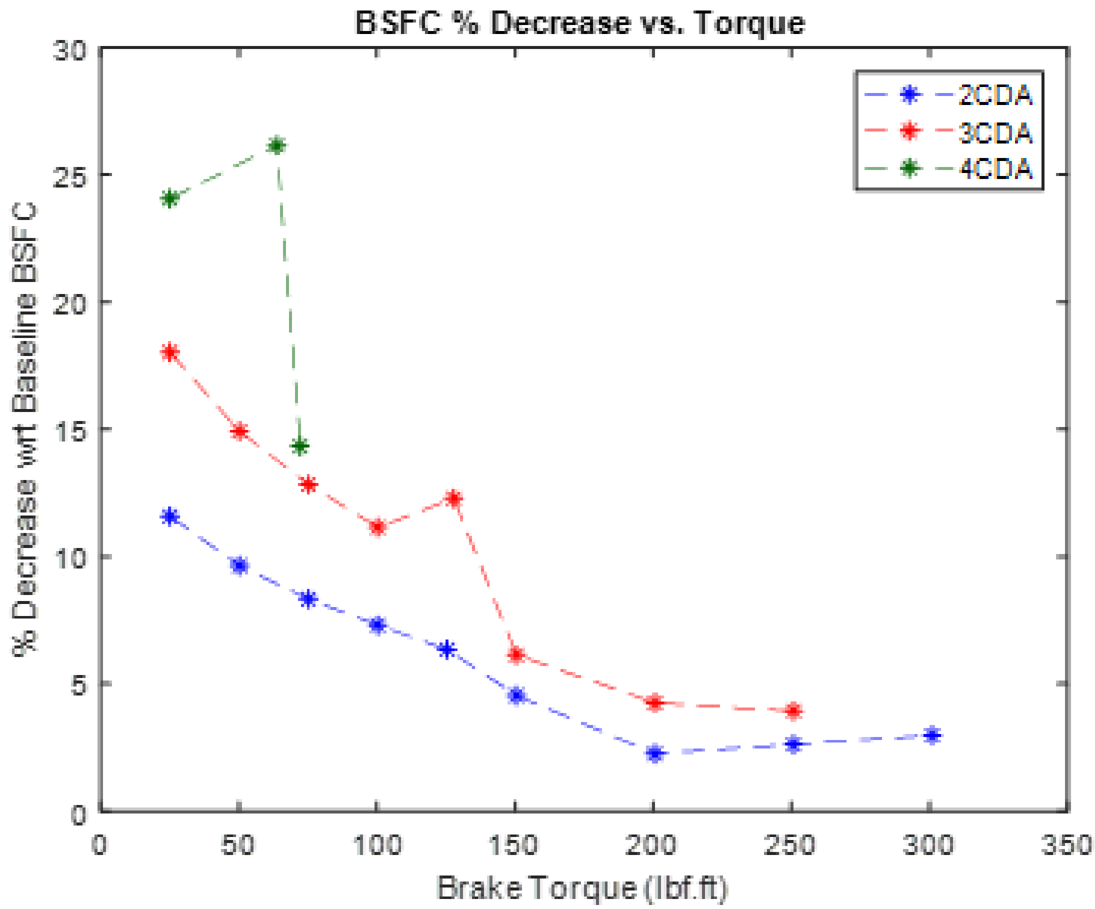

Figure 6.5. BSFC percent decrease

6.2.2 Limitations

All above plots (Figure 6.2-6.5) are plotted for operating points where the torque demands and EGR fraction targets are met simultaneously. The primary limitation of CDA is the ability to flow EGR to meet higher torque demands reduces with deactivated cylinders. In the simulation, EGR targets are set linearly with torque as discussed in subsection 3.2.2. To meet equivalent torque with deactivated cylinders requires elevated intake manifold pressures or pressures downstream of EGR valve. Elevated pressures downstream of EGR valve corresponds to difficulties to drive the EGR gas.

Additionally, as a greater number of cylinders are deactivated, difficulty to drive EGR gases increases further. This can be observed in Figure 6.6, as torque values where EGR fraction targets are met decreases with increase in number of deactivated cylinders. EGR targets are met upto 300ftlbs for 2CDA, 250ftlbs for 3CDA and 75ftlbs for 4CDA. Torque targets are met for all the above data points as seen in Figure 6.7.

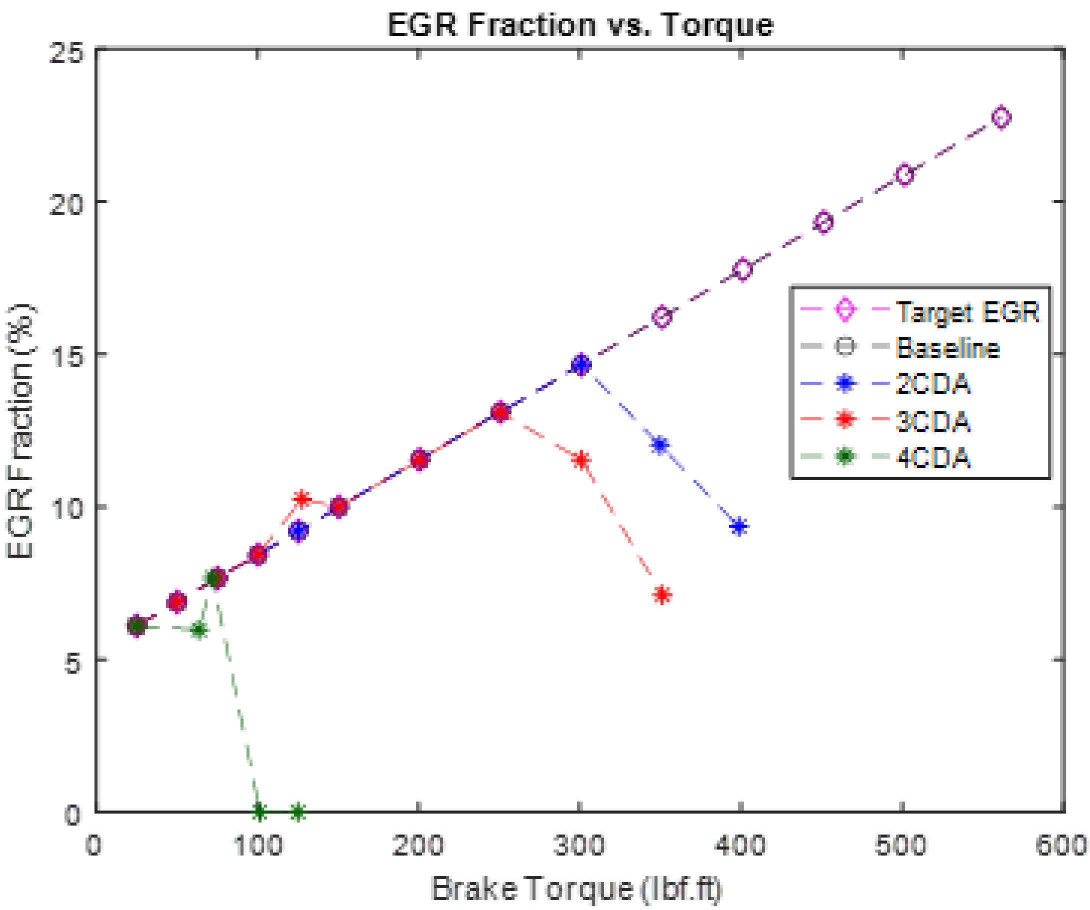

Figure 6.6. EGR Fraction (Simulation)

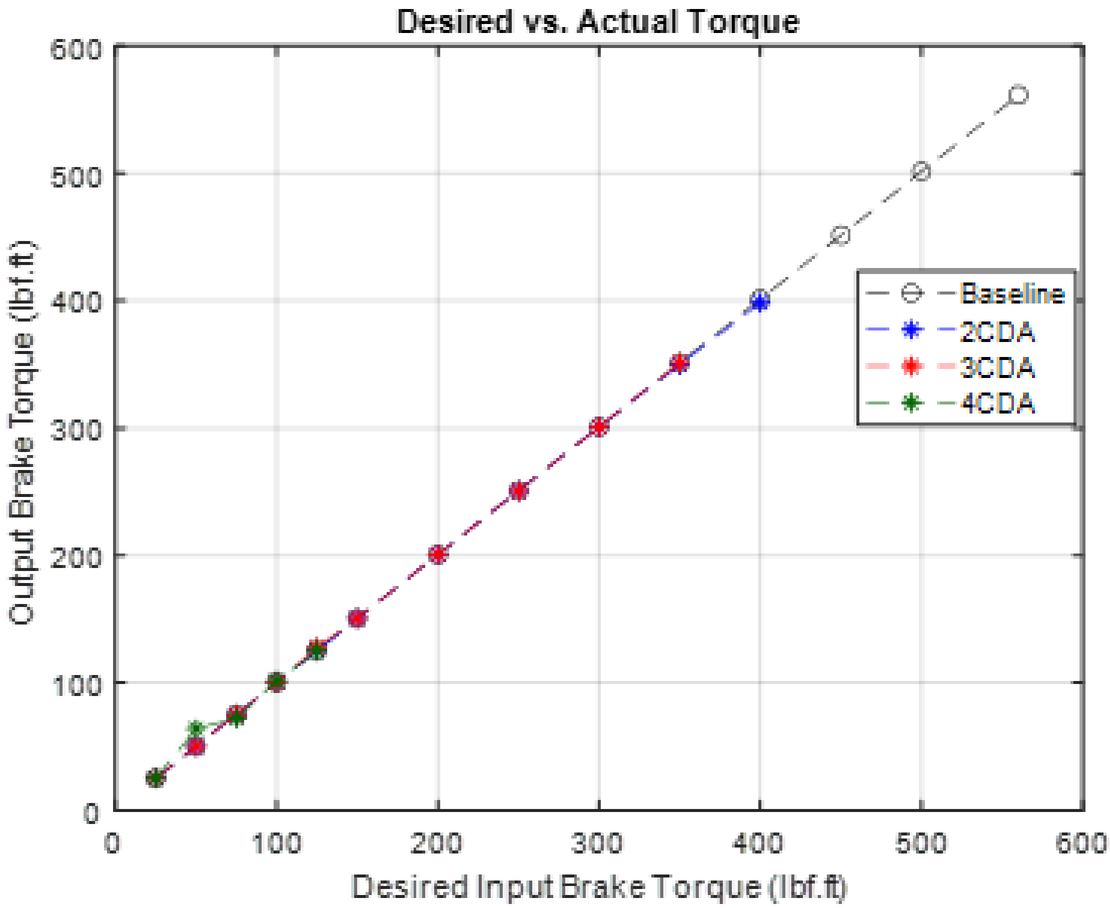

Figure 6.7. Output vs. Input Torque (Simulation)

6.2.3 Engine Cycle Efficiencies

The difficulty to drive EGR is further evident from the LogP-LogV plots. The Figure6.8 illustrates the LogP-LogV representation of the firing cylinders for 4 different cases : 25ftlbs, 50ftlbs, 75fltbs and 100ftlbs. In general, torque demand can be met in CDA by elevated intake manifold pressures. Elevated intake manifold pressure reduces the delta pressure between exhaust and intake manifold. This reduced pressure difference across the EGR valve makes it difficult to drive EGR. The limit can be observed based on the number of cylinders deactivated. For aggressive strategies like 4CDA,the limit is achieved at a low torque of 75 ftlbs.

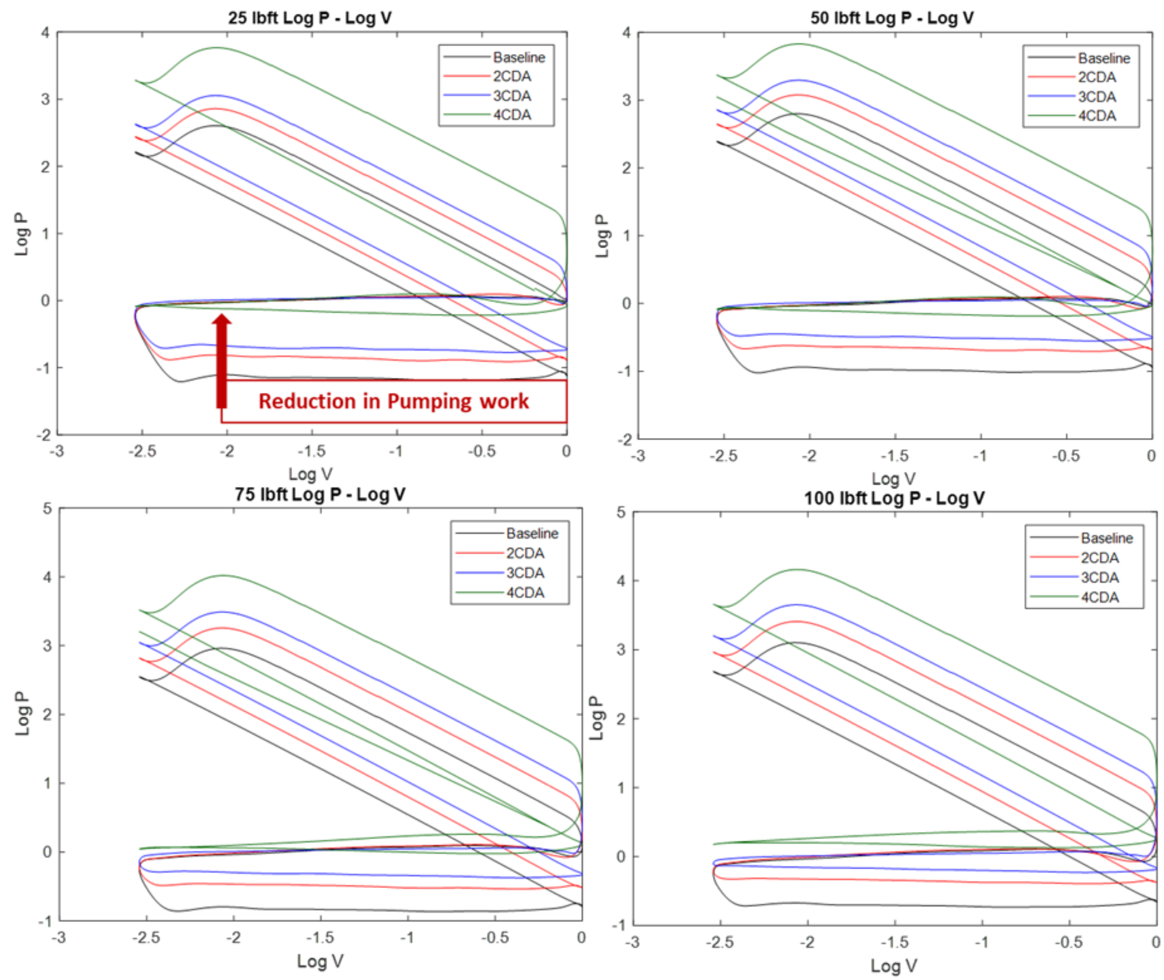

Figure 6.8. PV Diagrams (Simulation)

For example, from the 100ftlbs PV diagram the delta pressure is very small for the 4CDA case and corresponding EGR fraction plot confirms that the EGR fraction targets are not met for 100ftlbs for 4CDA.

However, the advantage of decrease in delta pressure across intake and exhaust manifold is the engine doing less amount of work to pump gases. The pumping loop decreases significantly for CDA strategies as evident from Figure 6.8. As a result, the fuel consumption would be maximum in the baseline case where the engine is working against a larger pressure gradient. Thus , fuel benefits are realized by reducing the pumping work or pumping loop in the PV diagram.

The Open cycle efficiency is related to the pumping of gases. OCE increases as the pumping loop decreases. This is congruent with the results in Figure 6.9. Normalized values are plotted for all efficiency plots. A maximum OCE improvement is seen for the lowest simulated torque value of 25ftlbs for 2CDA, 3CDA and 4CDA respectively. The OCE benefits decrease with increased load conforming with earlier results.

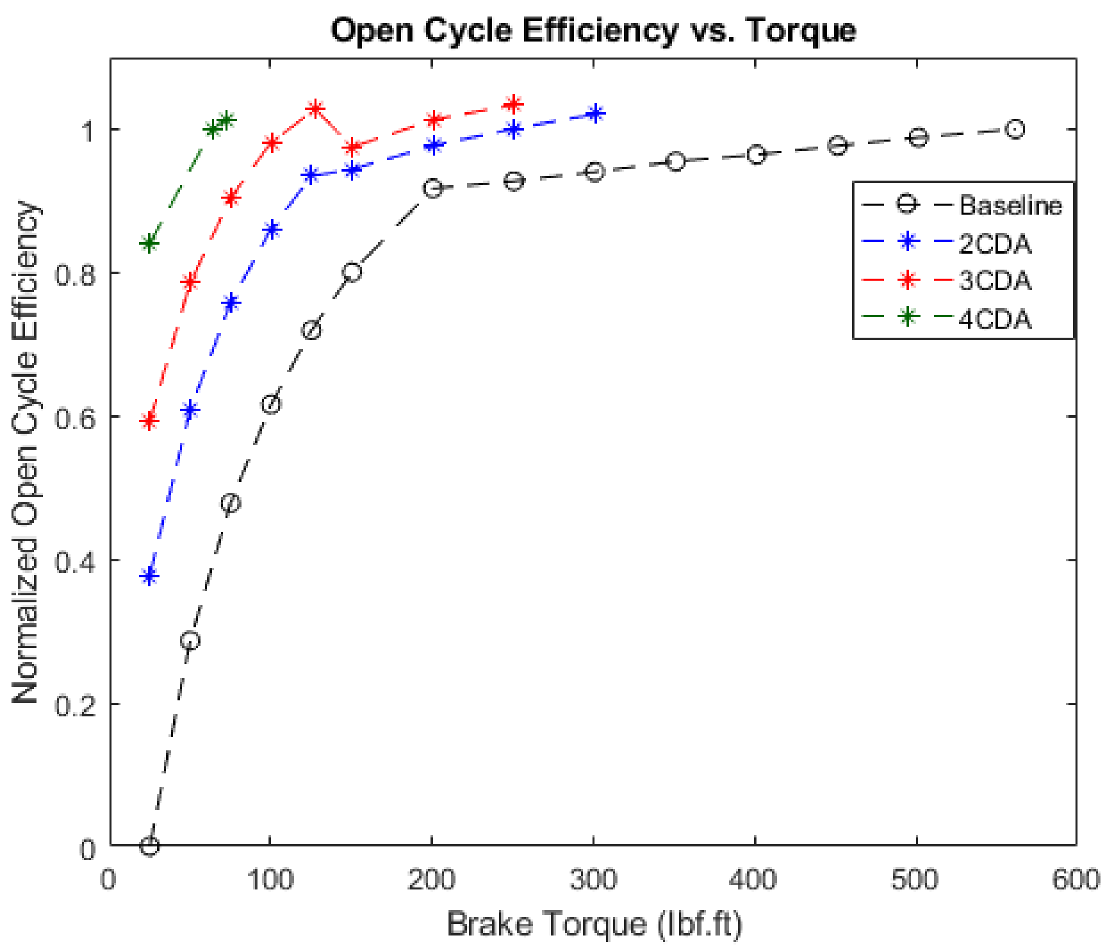

Figure 6.9. Open Cycle Efficiency (Simulation)

For the overall efficiency analysis, it is important to check all cycle efficiencies. The BTE is expressed as shown in equation.

The Closed cycle efficiency is the efficiency of the engine during the portion of time where both intake and exhaust valves are closed. This includes the compression,combustion and expansion process of the four stroke engine. This is affected by the combustion and heat transfer. The heat release rate influences the CCE. Due to the current model limitations of an imposed heat release rate mentioned in section 3.2.3, the CCE results are not truly representative of the how the engine would perform. The CCE results shown in Figure 6.10 have a couple of outliers as well.

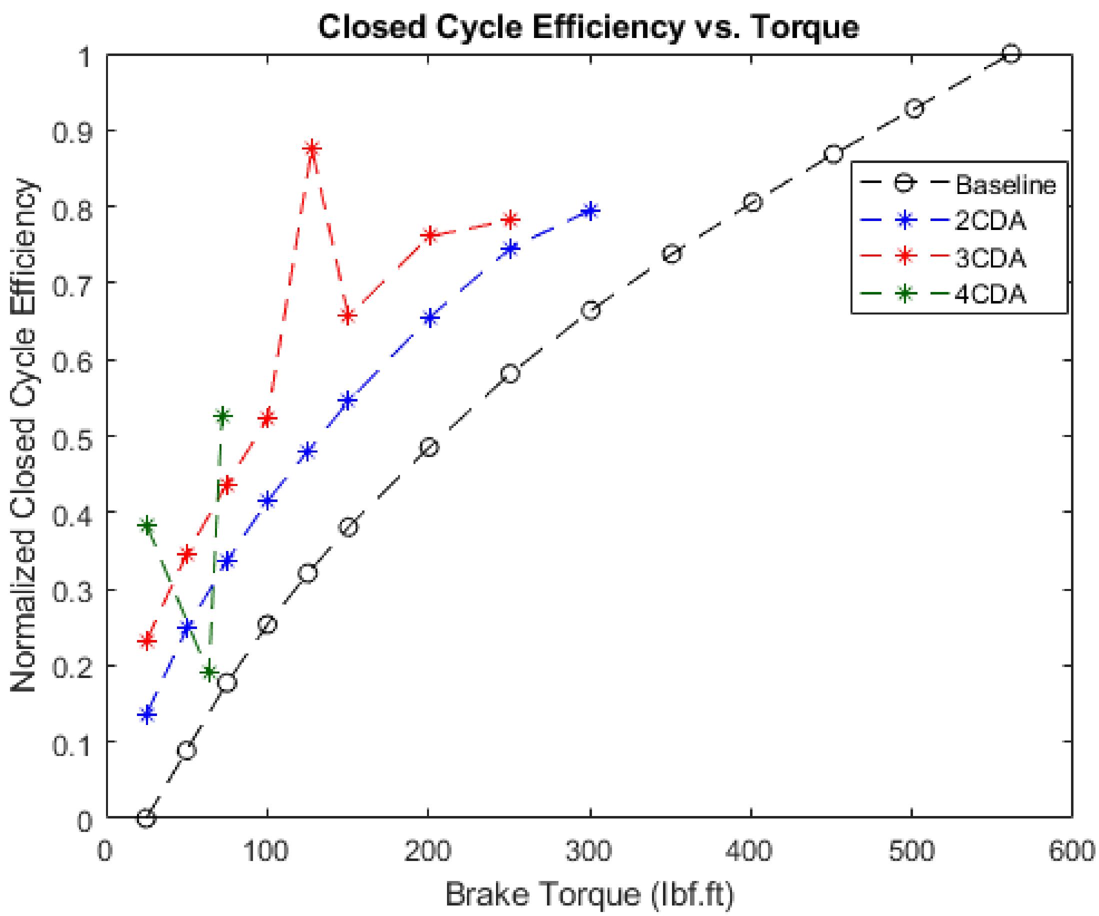

Figure 6.10. Closed Cycle Efficiency (Simulation)

The Mechanical Efficiency (ME) accounts for the mechanical losses in the system like frictional losses. It is dependant on the output power and speed. Since, the simulation conditions of troque and speed are same for CDA and Baseline there is no deviation in the ME for CDA.

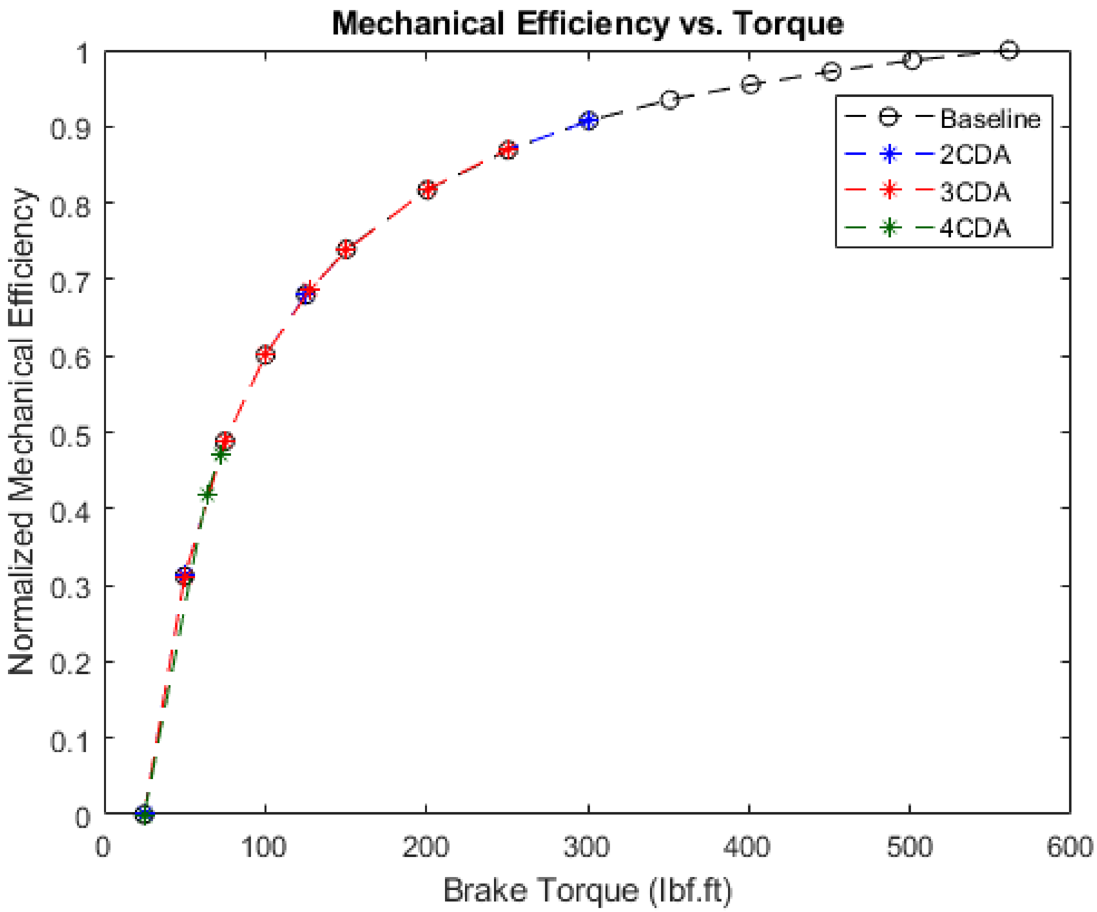

Figure 6.11. Mechanical Efficiency (Simulation)

The BTE comprises of OCE, CCE and ME (refer equation 3.2). Based on the efficiency plots, the improvements in OCE are the most significant and account for the overall BTE improvement and fuel benefits. The efficiency analysis gives a good understanding about the breakdown of the fuel benefits. Further analysis is done to sanity check efficiency results and engine behaviour in the simulation.

6.3 Intake Manifold Gas Properties

The engine operating in stoichiometric condition, is expected to have similar reductions in Air flow rate as the Fuel flow rate seen in Figure 6.2. Figure 6.12 is consistent and shows a reduced air flow rate due to CDA.

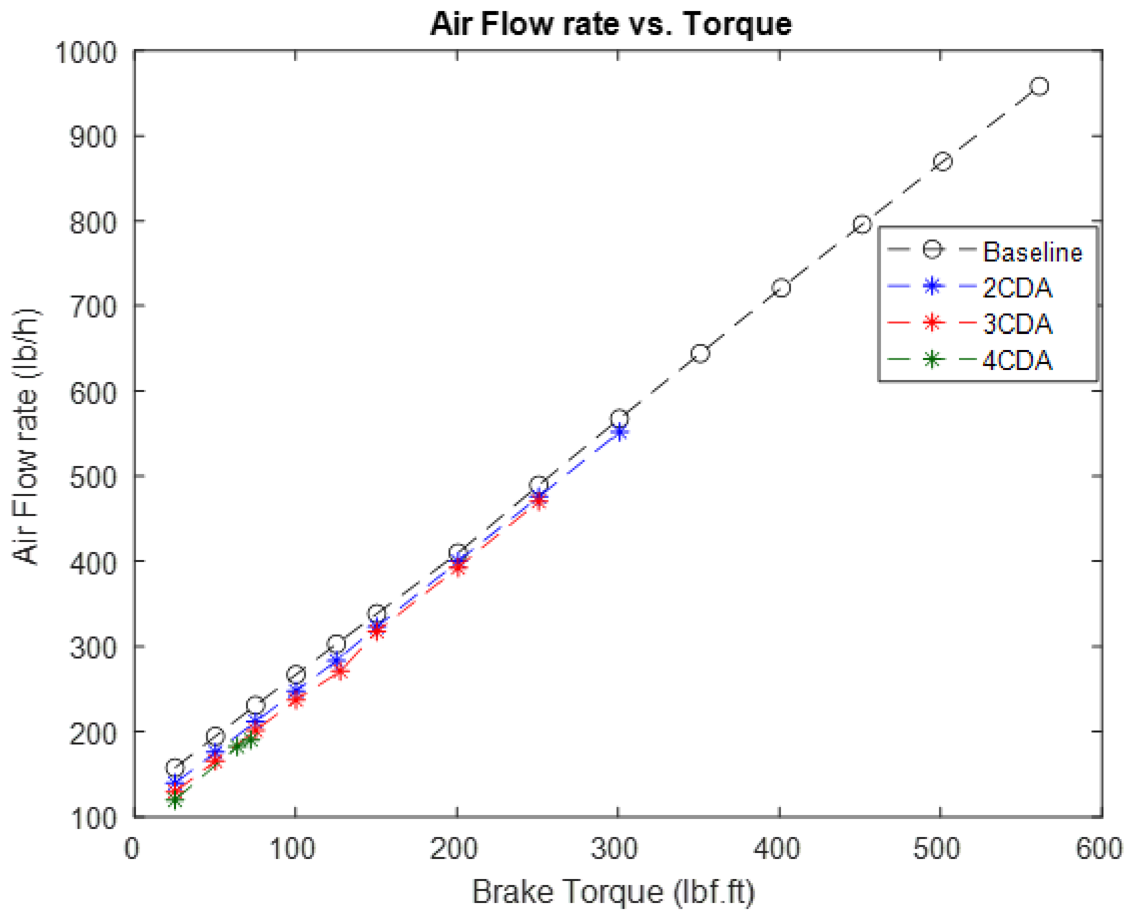

Figure 6.12. Air Flow Rate (Simulation)

For the engine to operate at a reduced air flow rate during CDA, the intake manifold pressures are required to be higher in comparison to the Baseline to generate same amount of torque. Figure 6.13 shows the rise in IMP. For aggressive CDA strategy of 4CDA, the IMP is almost double that of Baseline.

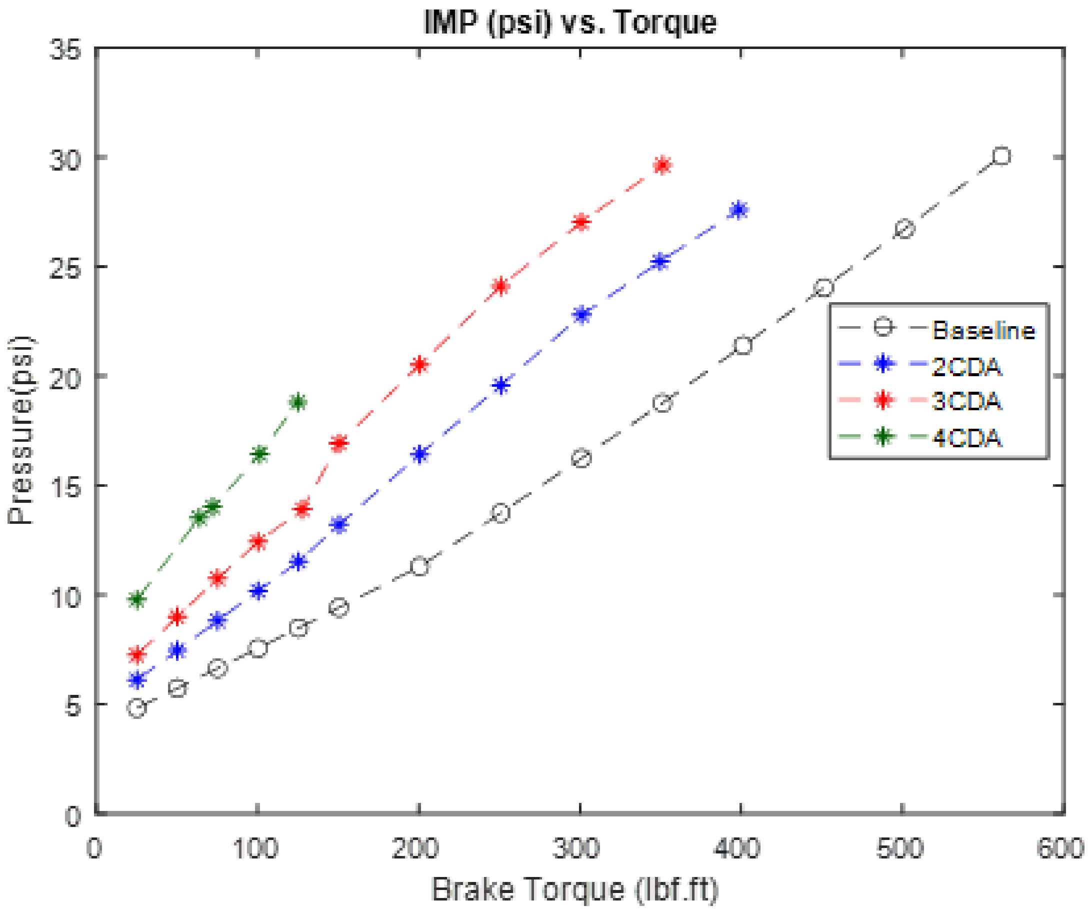

Figure 6.13. Intake Manifold Pressure (Simulation)

6.4 Gas Exchange Actuators

Two main gas exchange actuators in the current system are :

- ***Wastegate*** controlled by the wastegate controller to reach target boost pressure.
- ***Throttle Valve*** controlled by the throttle controller to control intake charge flow to meet demanded torque.

6.4.1 Wastegate

Wastegate valve controls the flow of exhaust gases to the turbine, which determines the turbine speed which in turn determines the compressor speed. In the GT-Power model, the wastegate is an orifice connection with a maximum orifice dia. of 50mm. Maximum orifice dia. indicates wastegate fully open to the exhaust and engine operation at atmospheric pressure or naturally aspirated zone. Closing of the wastegate orifice should indicate increase in the boost pressure. Wastegate orifice dia. is shown in Figure6.14 and corresponding boost pressures can be seen in Figure 6.15. In 6-Cylinder firing, Baseline operation, the wastegate starts closing around 150ftlbs torque value, where the boost pressure starts increasing. The boosting zone shifts to the left for CDA as wastegate is actuated at lower torques based on number of deactivated cylinders. The operation of wastegate is in correspondence with the observed boost pressures.

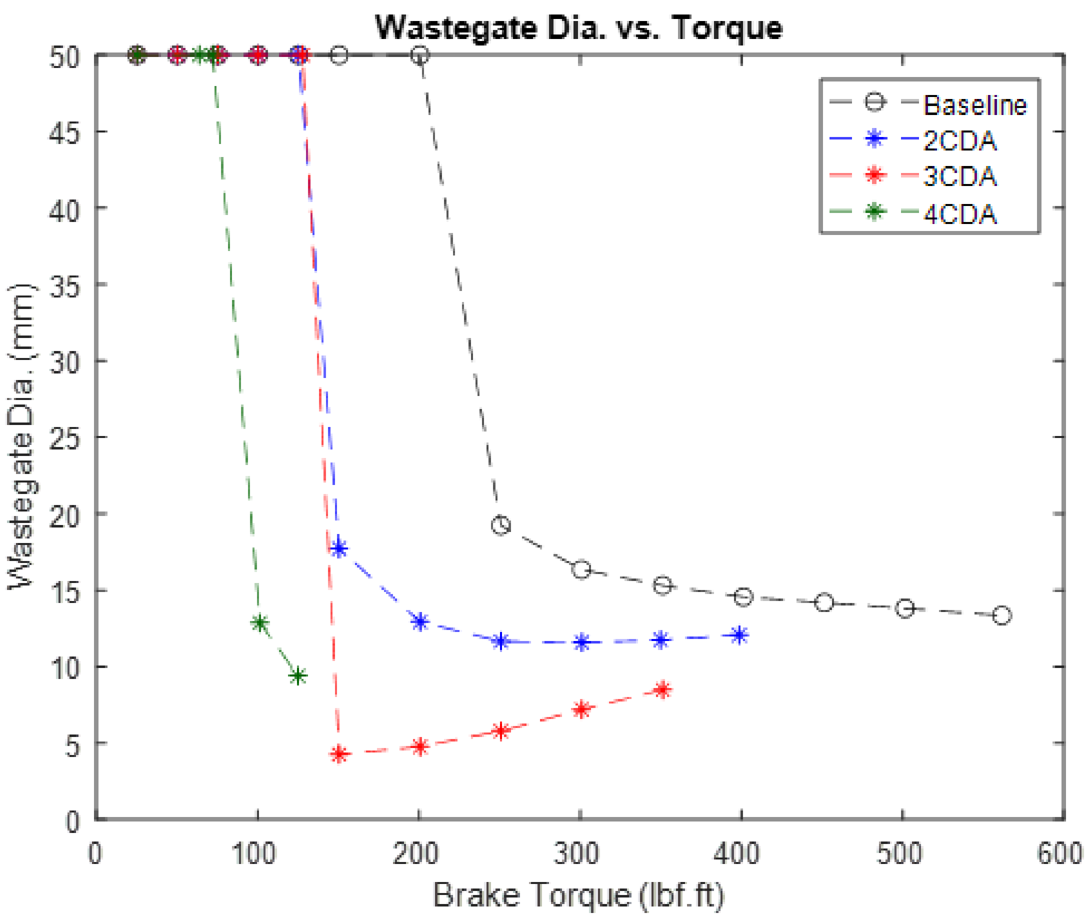

Figure 6.14. Wastegate Diameter (Simulation)

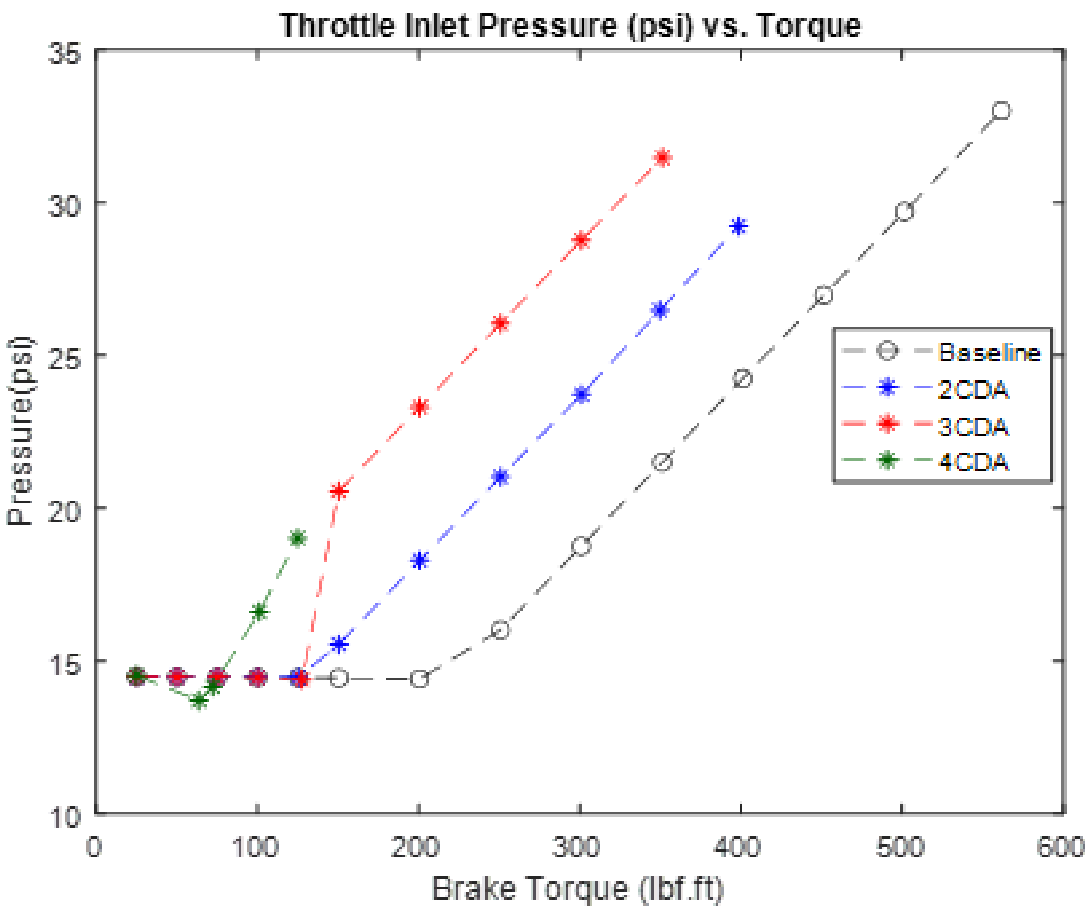

Figure 6.15. Throttle Inlet Pressure (Simulation)

6.4.2 Throttle Valve

The throttle valve operation in a conventional engine operation is to reduce the power output at part loads by restricting the air flow. The restriction of flow cause the pumping losses. To investigate the above discussed benefits further, it is critical to look at the flow across the throttle valve and its behaviour. The downstream pressure across the throttle valve is the Intake manifold Pressure seen in Figure 6.13. The pressure upstream of the throttle valve is seen in Figure 6.15. The 25-200ftlbs torque region for the baseline 6 cylinder firing, corresponds to naturally aspirated operation of the engine. A high difference across the pressures upstream and downstream of the valve is indicative of the high work done to flow gas across the valve or high losses . For 25ftlbs torque, the baseline as well as all the CDA cases are in the naturally aspirated operation. The throttle upstream pressure for all the cases is atmospheric pressure. However, from Figure 6.13, the throttle downstream pressure increases for CDA. The decrease in delta pressure across the valves implies reduced throttling losses.

For the baseline 6 cylinder firing simulation case,the throttle angle opens up linearly with increase in torque in the naturally aspirated zone of 25-200ftlbs. For boosted operation, the throttle is slightly open. Although the throttle is not fully open for maximum torque case, this could be adjusted by the right boost pressure targets in the simulation or comparing it to experimental baseline data.

Intuitively, for CDA cases the throttle angle should increase . However, that is not the case as seen in Figure 6.16. The throttle angle almost tracks the Baseline for 2CDA and 3CDA. For aggressive strategy of 4CDA, the throttle angle opens up wide. This phenomenon was further investigated. Studies with CDA implemented on S.I engines with throttle angle information available were reviewed [14],[15]. Study from ADC university conducted on a 1.6L, 4 cylinder engine compared a single operating point for CDA and Baseline. Although significant fuel benefits were observed, the throttle angle values remained fairly similar (6.8 deg in CDA as compared to 6.3 deg in 6 Cylinder Operation) [14]. Another experimental study conducted in ORNL showed slight increase in the throttle angle (about 2 degrees) on a 3.5L, 6cylinder S.I engine at different operating points [15]. Similar throttle angles does not necessarily imply similar throttling losses. This can be explained from the equation below.

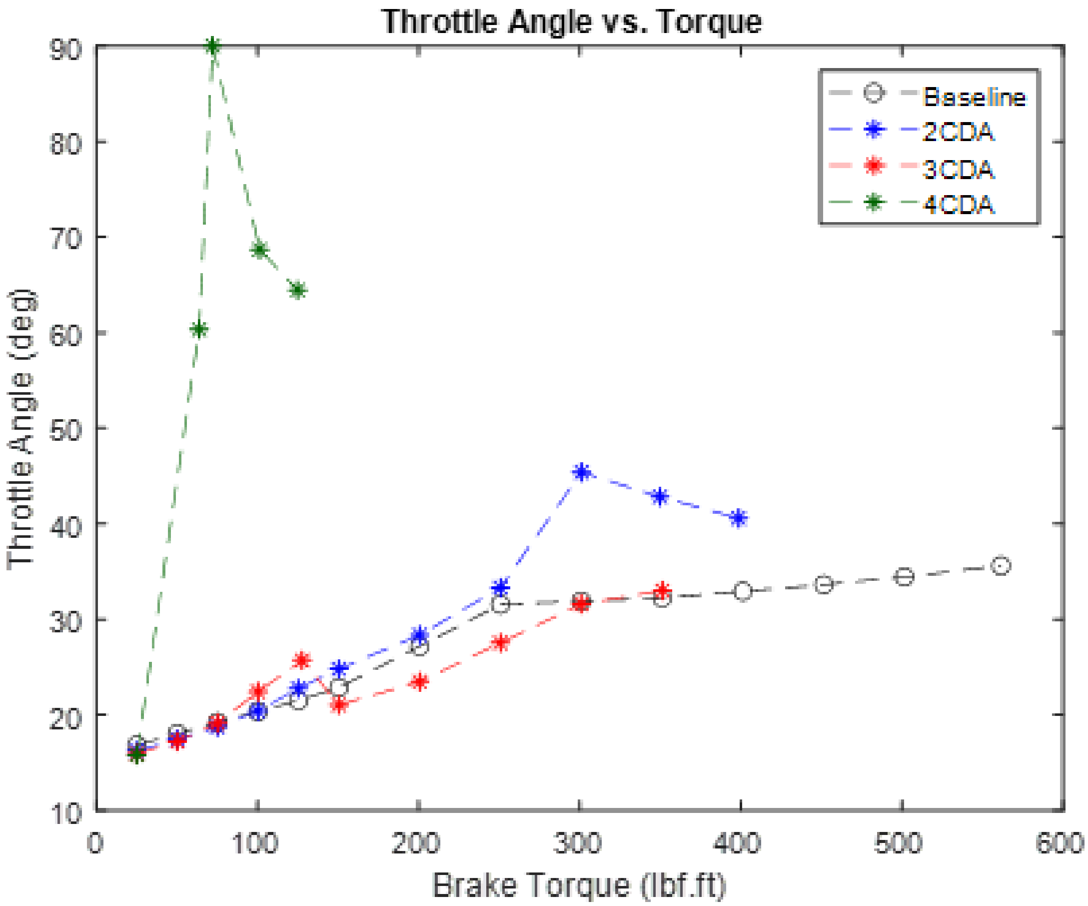

Figure 6.16. Throttle Angle (Simulation)

The flow across a valve is given by :

$$\dot{m} = Cd_1 * \rho * (\frac{\pi D^2}{4})(\sqrt{\frac{2 * \delta P}{\rho}}) \tag{6.2}$$

where $\dot{m}$ = mass flow rate across the valve

C_{d1} = discharge coefficient

D = Throttle diameter

δP = Pressure across the valve

ρ = fluid density

The above equation can be written as

$$\delta P = \frac{8\dot{m}}{\rho}(\frac{1}{Cd_1 \pi D^2})^2 \tag{6.3}$$

In the GT-Power model, discharge coefficient C_{d1} is correlated to the throttle valve angle via a lookup table. Assuming throttle angle remains the same for both Baseline and CDA cases, the discharge coefficient would be same in both cases. For delta pressure across the valve, the only variable between Baseline and CDA cases is the air flow rate. In CDA , the air flow is reduced in comparison to Baseline. Hence, it can be demonstrated that reduced delta pressure across the valve can be achieved with reduced mass flow, even if the throttle angle remains constant.

6.5 Summary

In summary, 1D simulations of CDA on a 6 cylinder natural gas S.I engine showed significant fuel benefits and BTE improvements in the low load torque region. Significant improvements in Open cycle efficiency were responsible for the fuel savings. The OCE gains were caused by overcoming part load pumping losses by implementation of CDA. The ability to drive EGR served as the primary limitation to extend CDA capabilities at higher torques. The intake manifold gas properties along with the behaviour of the gas exchange actuators were in correspondence with the observed efficiency improvement results.

7. FUTURE SCOPE

7.1 Recommendations

7.1.1 Series Hybrid Powertrain

The results presented in the thesis are a preliminary understanding on understanding the efficiency improvements for two systems in consideration.

The on-highway tests demonstrated a good understanding of the powertrain behaviour and its capabilities to save fuel. However, there were some limitations to the analysis that can be included in future work.

The current analysis doesn't relate the powertrain energy savings to the measured engine fuel savings. Engine fuel map data can enable the correlation between the powertrain energy savings to the fuel benefits. Access to the Engine ECM and its fuel map would be helpful in understanding the engine operation on the torque and power curve. A one to one comparison can then be done between a conventional powertrain and hybridization of the powertrain to realize the BSFC benefits.

The power electronics efficiency could be further analyzed based on the power management strategy decided by the control algorithm in each run. The power management strategy is the decision the controller makes of the power division of the generator and battery. This piece of information was critical and proprietary to the startup and couldn't be shared with the Purdue team. Deeper understanding and modification of control algorithms can be an important future work to maximize the work done by the battery. The study can also be extended to determine efficient Power management strategies with respect to trailer weight.

The entire study was focused on efficiencies of the electrical pathways in the powertrain. Determining mechanical power losses could be a scope for future work. Dynamo-meter testing of the transmission and engine-generator coupling could aid in recognizing mechanical losses. This would help in understanding the entire energy pathway from the engine to the wheels.

7.1.2 Natural Gas CDA

The model limitations discussed in 6.2.2 can be overcome by matching experimental data. The imposed Heat release rate could be replaced by experimental heat release rates from engine baseline testing. Replacing the Heat Release Rate would represent appropriate combustion and give a better understanding of Closed cycle efficiencies.

Overall limitations of CDA is the ability to meet EGR targets at higher loads. This could be overcome by combining other VVA strategies along with CDA at higher torques.

(i) CDA with iEGR - Internal EGR (iEGR) is the trapping of exhaust gases from the previous engine cycle by eliminating the intake and exhaust valve overlap. This is also called as negative valve overlap. The exhaust gases remain trapped inside the cylinders after which the intake valve is opened for fresh charge.

(ii) CDA with reinduction - Another strategy for implementing iEGR is via re-induction. In this strategy, either the exhaust valve is opened during the intake stroke for a short duration of time or the intake valve is opened during the exhaust stroke.

Combining the above strategy with CDA may extend the capabilities of CDA at higher torques while meeting higher EGR tragets.

REFERENCES

[1] B. Gates, *How to avoid a climate disaster : the solutions we have and the breakthroughs we need*, eng. 2021, ISBN: 9780385546133.

[2] *International - U.S. Energy Information Administration (EIA)*. [Online]. Available: https://www.eia.gov/international/data/world.

[3] *Trucking Industry Statistics*. [Online]. Available: https://truckerpath.com/blog/trucking-industry-statistics/.

[4] ExxonMobil, "Outlook for energy: A perspective to 2040," Tech. Rep., 2019. [Online]. Available: https://corporate.exxonmobil.com/Energy-and-environment/Looking-forward/Outlook-for-Energy/Outlook-for-Energy-A-perspective-to-2040%5C#ExxonMobilsupportstheParisAgreement, (accessed: 07.01.2020).

[5] *Commercial Vehicle Market Dynamics Evolve Over Time to Include Electrification, Yet Diesel Remains Dominant, IHS Markit Says | Business Wire*. [Online]. Available: https://www.businesswire.com/news/home/20180918005528/en/Commercial-Vehicle-Market-Dynamics-Evolve-Over-Time-to-Include-Electrification-Yet-Diesel-Remains-Dominant-IHS-Markit-Says.

[6] *Environmental Protection Agency and Department of Transportation, National Highway Traffic Safety Administration: Greenhouse Gas Emissions and Fuel Efficiency Standards for Medium- and Heavy-Duty Engines and Vehicles–Phase 2*, eng. 2016.

[7] D. L. Farrell, *Ultra-low nox, durability and warranty part 2 - engine and powertrain integration*, SAE COMVEC Digital Summit, 2020.

[8] K. R. Vos, G. M. Shaver, A. K. Ramesh, and J. McCarthy, "Impact of cylinder deactivation and cylinder cutout via flexible valve actuation on fuel efficient aftertreatment thermal management at curb idle," *Frontiers in Mechanical Engineering*, vol. 5, p. 52, 2019, ISSN: 2297-3079. DOI: 10.3389/fmech.2019.00052. [Online]. Available: https://www.frontiersin.org/article/10.3389/fmech.2019.00052.

[9] C. M. Allen, D. B. Gosala, G. M. Shaver, and J. James McCarthy, "Comparative study of diesel engine cylinder deactivation transition strategies," *International Journal of Engine Research*, vol. 20, no. 5, pp. 570–580, 2019. DOI: 10.1177/1468087418768117. eprint: https://doi.org/10.1177/1468087418768117. [Online]. Available: https://doi.org/10.1177/1468087418768117.

[10] D. B. Gosala, C. M. Allen, A. K. Ramesh, G. M. Shaver, J. James McCarthy, D. Stretch, E. Koeberlein, and L. Farrell, "Cylinder deactivation during dynamic diesel engine operation," *International Journal of Engine Research*, vol. 18, no. 10, pp. 991–1004, 2017. doi: 10.1177/1468087417694000. eprint: https://doi.org/10.1177/1468087417694000. [Online]. Available: https://doi.org/10.1177/1468087417694000.

[11] C. Mi, *Hybrid electric vehicles : principles and applications with practical perspectives*, eng, Second edition., ser. Automotive series (Wiley). 2018, isbn: 1-118-97056-X.

[12] D. W. Stanton, "Systematic development of highly efficient and clean engines to meet future commercial vehicle greenhouse gas regulations," eng, vol. 6, no. 3, pp. 1395–1480, 2013, issn: 1946-3936.

[13] J. Foster, "Advanced control strategies for diesel engine thermal management and class 8 truck platooning," M.S. thesis, Purdue University - West Lafayette, Jul. 2020.

[14] S. N. Mohamed Soid, M. F. Muhamad Said, A. B. Abdul Aziz, Z. Abdul Latiff, and A. Mahmoudzadeh Andwari, "Investigation of cylinder deactivation (cda) strategies on part load conditions," in *SAE 2014 International Powertrain, Fuels Lubricants Meeting*, SAE International, Oct. 2014. doi: https://doi.org/10.4271/2014-01-2549. [Online]. Available: https://doi.org/10.4271/2014-01-2549.

[15] D. B. Strange, *Control system development for gasoline engines with passive scr and cylinder deactivation*, eng, 2019.